Measurement of the Partial Z Decay Width into b Quarks with the L3 Detector at LEP

D I S S E R T A T I O N

zur Erlangung des akademischen Grades

d o c t o r   r e r u m   n a t u r a l i u m
(Dr. rer. nat.)

im Fach Physik

eingereicht an der

Mathematisch-Naturwissenschaftlichen Fakultät I

der Humboldt-Universität zu Berlin

von

Dirk Kamrad

geboren am 7. Januar 1966 in Torgelow

Präsident der Humboldt-Universität zu Berlin
Prof. Dr. Dr. h.c. Hans Meyer

Dekan der Mathematisch-Naturwissenschaftlichen Fakultät I
Prof. Dr. Jürgen Rabe

Gutachter: 1. Prof. Dr. Th. Hebbeker (Humboldt-Universität)
           2. Prof. Dr. P. Söding (Humboldt-Universität)
           3. PD Dr. M. Pohl (ETH Zürich)

Tag der mündlichen Prüfung: 18. Mai 1999

Abstract

In this thesis the relative decay width of the Z to bottom quarks, $R_b^0 = \frac{\Gamma(Z \to b\bar{b})}{\Gamma(Z \to \text{hadrons})}$, has been measured by tagging bottom hadrons exploiting their lifetime information. The analysis has been performed using the data collected at the Z resonance in 1994 and 1995 with the L3 detector corresponding to $\mathcal{L} \approx 71$ pb^{-1} of integrated luminosity. Experimentally, R_b^0 can be obtained at the Z resonance from the ratio of cross sections $R_b = \frac{\sigma(e^+e^- \to b\bar{b})}{\sigma(e^+e^- \to \text{hadrons})}$, by applying a small correction due to photon propagation. The measurement is based on the double-tag method which allows to determine the b tag efficiency from data. Hence, precise knowledge of the details of B hadron decays is not required. The result of the measurement is:

$$R_b^0 = 0.2178 \pm 0.0018(\text{stat}) \pm 0.0031(\text{syst}) - 0.196(R_c^0 - 0.172).$$

The parameter R_c^0, the relative decay width of the Z boson into charm quarks, has not been fixed within the measurement. Taking the Standard Model prediction for $R_c^0 = 0.172$, the result is in agreement with the Standard Model prediction for R_b^0. R_b^0 is a function of the effective vector and axial-vector couplings of the electroweak neutral current. Using a second observable – the forward-backward asymmetry of the b quarks produced in the Z decay – these couplings are derived to be:

$$
\begin{aligned}
g_V^b &= -0.2984^{+0.0381}_{-0.0562} \\
g_A^b &= -0.5275^{+0.0356}_{-0.0200}.
\end{aligned}
$$

The couplings of fermions to the Z boson are of great importance in establishing the validity of the Standard Model and investigating physics effects beyond it.
The experimental results of L3 on the neutral current couplings of the b quark do not provide compelling evidence for physics beyond the Standard Model. Thus, the b quark data are mutually consistent with the theory; the b quark is a representative of the third-generation weak iso-spin doublet. In that sense it can be interpreted as proof of the existence of the top quark, which is the Standard Model weak iso-spin partner of the b quark.
The combination of these results with other very precise measurements expounds small deviations from the Standard Model. Possible contributions of new physics are discussed.

Inhalt

Diese Arbeit beschreibt die Messung der Größe $R_b^0 = \frac{\Gamma(Z \to b\bar{b})}{\Gamma(Z \to \text{hadrons})}$, die relative Zerfallsbreite des Z Bosons in *bottom* Quarks, durch die Identifizierung von *bottom* Hadronen unter Ausnutzung ihrer Lebensdauerinformation. Die Analyse erfolgte mit Daten, die 1994 und 1995 mit dem L3 Detektor auf der Z-Resonanz aufgezeichnet wurden und einer integrierten Luminosität von $\mathcal{L} \approx 71$ pb^{-1} entsprechen. Experimentell kann R_b^0 aus dem Verhältnis der Wirkungsquerschnitte $R_b = \frac{\sigma(e^+e^- \to b\bar{b})}{\sigma(e^+e^- \to \text{hadrons})}$ bestimmt werden. Dazu wird auf den Beitrag des Photonaustausches korrigiert. Die Messung macht von der *double-tag* Methode, die die Bestimmung der Identifikationseffizienz für *bottom* Quarks aus den Daten erlaubt, Gebrauch. Eine genaue Kenntnis der Details des B-Hadron-Zerfalls is somit nicht erforderlich. Das Ergebnis der Messung ist:

$$R_b^0 = 0.2178 \pm 0.0018(\text{stat}) \pm 0.0031(\text{syst}) - 0.196(R_c^0 - 0.172).$$

Die Größe R_c^0, die relative Zerfallsbreite des Z Bosons in charm Quarks, wurde nicht fixiert. Wird für R_c^0 die Vorhersage des Standardmodells $R_c = 0.172$ angenommen, stimmt die Messung mit der Standardmodellvorhersage für R_b^0 überein.

R_b^0 ist eine Funktion der effektiven Vektor- und Axialvektor-Kopplungskonstanten des elektroschwachen neutralen Stromes. Unter Hinzunahme einer zweiten Meßgröße – der Vorwärts-Rückwärts-Asymmetrie der b Quarks aus dem Z Zerfall – wurden diese Kopplungskonstanten berechnet:

$$
\begin{aligned}
g_V^b &= -0.2984^{+0.0381}_{-0.0562} \\
g_A^b &= -0.5275^{+0.0356}_{-0.0200}.
\end{aligned}
$$

Die Kopplungen der Fermionen an das Z-Boson sind von großer Bedeutung für die Bestätigung der Gültigkeit des Standardmodells und das Studium von Effekten, die nicht mit diesem Modell zu erklären sind. Die elektroschwachen Kopplungen des neutralen Stromes, die aus experimentellen Resultaten von L3 bestimmt wurden, geben keine Hinweise auf Physik außerhalb des Standardmodells. Die Daten der *bottom* Quarks sind somit in Übereinstimmung mit der Theorie; das *bottom* Quark ist ein Repräsentant des Isospin-Dubletts der dritten Generation. Gleichermaßen

kann dies als Beweis für die Existenz des top Quarks interpretiert werden, welches im Standardmodell der Isospin-Partner des *bottom* Quarks ist.

Die Kombination dieser Resultate mit anderen sehr präzisen Messungen zeigt eine kleine Abweichung von der Standardmodell-Vorhersage. Mögliche Beiträge neuer Physik werden diskutiert.

Contents

Chapter 1

Introduction and Motivation

The Standard Model of the electroweak interaction - introduced by Glashow, Salam, and Weinberg in the seventies [1–4] - describes interactions between basic constituents of matter. Over the last twenty years, many tests of the Standard Model have been carried out with increasing precision. Its predictions for a large amount of quantities are in remarkable agreement with the precise measurements from the **L**arge **E**lectron **P**ositron collider at CERN[1]. LEP started its operation in 1989 with the goal of studying the properties of the vector boson of the weak neutral current, the Z, and was upgraded 1995 to operate above the pair production threshold of the vector boson of the weak charged current, the W. In order to distinguish these two regimes of LEP they are called LEP-I and LEP-II, respectively. During the LEP-I phase about 15 million electron-positron annihilations have been recorded at centre-of-mass energies in the vicinity of the Z resonance. Precise measurements have been performed of the Z mass, its width and leptonic couplings using leptonic and inclusive hadronic decays of the Z. With the large LEP-I statistics and advanced detector technologies, high precision measurements at LEP have been extended into the investigation of heavy quarks. The measurement of the relative decay width of the Z into b quarks:

$$R_b^0 \equiv \frac{\Gamma_{Z \to b\bar{b}}}{\Gamma_{Z \to hadrons}} \qquad (1.1)$$

is of particular interest in the Standard Model. Electroweak corrections involving

---

[1]An overview of all experiments and laboratories mentioned in this work can be found in the appendix A

the top quark affect the partial Z decay width, $\Gamma_{b\bar{b}}$, differently from the widths for lighter quarks. As a result, R_b^0 depends on the top quark mass but is to a large extent independent of other corrections such as QED or QCD corrections or electroweak corrections to the Z propagator. Therefore, with the known mass of the top quark, measured by CDF and D0 [5–7], R_b^0 provides a sensitive environment to detect a signal for physics beyond the Standard Model. The measurement also allows to obtain the electroweak couplings of the b quark to the Z boson. The Standard Model assumption that the b quark is a representative of an iso-spin doublet is capable of experimental proof by measuring the neutral electroweak couplings. The iso-spin partner of the b quark is the top quark.

Until mid 1996, the average value of R_b^0 measured by the LEP experiments and SLD was about three standard deviations above the Standard Model prediction [8]. Because of the large discrepancy between the observed and predicted values of R_b^0, a lot of interest and effort was invested in updating the measurements, to confirm or disclaim the deviation from the Standard Model.

The work presented in this thesis covers the latest measurement of R_b^0 using data taken with the L3 detector at LEP from 1994 to 1995. The result was published as a contribution to the ICHEP conference [9].

The system of units adopted here is that of particle physics, where the Planck constant $\hbar = h/2\pi$, and the speed of light, c, are set to unity, $\hbar = c = 1$. Energies, momenta, and masses are measured in units of electron volts, $1eV = 1.60217733(49) \cdot 10^{-19} J$. Cross sections are given in units of barns, $1b \equiv 10^{-18} m^2$. Otherwise, SI units are used.

Short History of Quark Physics

- **1963**: Cabibbo postulated the mixing between hadron states to explain the observation of strangeness-changing currents [10]; later interpreted as the mixing between down and strange quarks.

- **1964**: Gell-Mann [11] and Zweig [12] simultaneously introduced quarks as the constituents of the schematic model of mesons and baryons.

- **1970**: Glashow, Iliopoulos and Maiani introduced an extra quark, the charm, as iso-spin partner of the strange quark, in order to explain the suppression of flavour-changing neutral currents in K decays [4].

- **1973**: Kobayashi and Maskawa proposed a third generation of quarks (today known as b and t) in order to accommodate CP-violation in the Standard Model. At least one phase is present in the mixing matrix for three or more quark generations: one phase in the case of three generations, three phases in case of four generations [13]. It was shown that the presence of such a phase is able to explain the CP-violating effects observed in the neutral kaon system.

- **1974**: Gaillard, Lee and Rosner [14] outlined a phenomenology to describe the spectroscopy, production, decays and mixing of particles containing charm quarks, just a month before their discovery. The charm quark was discovered simultaneously at SLAC at the SPEAR e^+e^- collider and at BNL in proton nucleon scattering as 'hidden' charm J/ψ, in 1974 [15, 16].

- **1977**: The b quark was first seen in a fixed target experiment $p + N \rightarrow \Upsilon(1S) + X$ at FNAL [17, 18], by studying the $\mu^+\mu^-$ invariant mass spectrum. This result was confirmed by studying e^+e^- annihilations [19–22] leading to the observations of further Υ states. The structure of the e^+e^- cross section in the 10 GeV region is shown in Figure 1.1. The $\Upsilon(4S)$ $b\bar{b}$ state lies just above the threshold for the $B\bar{B}$ production, and most of the measurements concerning B mesons are done with data taken at the $\Upsilon(4S)$ resonance (*e.g.* ARGUS, CLEO, Crystal Ball and CUSB).

- **1987**: The first measurement of the mixing in the $B\bar{B}$-system was presented by the ARGUS collaboration [23].

- **1994**: The first direct experimental evidence for the top quark was published by CDF and later by the D0 collaboration [5–7].

In the six years of running LEP at energies around the Z resonance heavy quark and particularly b quark physics was a very important part of the experimental program. In addition to spectroscopic measurements the production rates of many
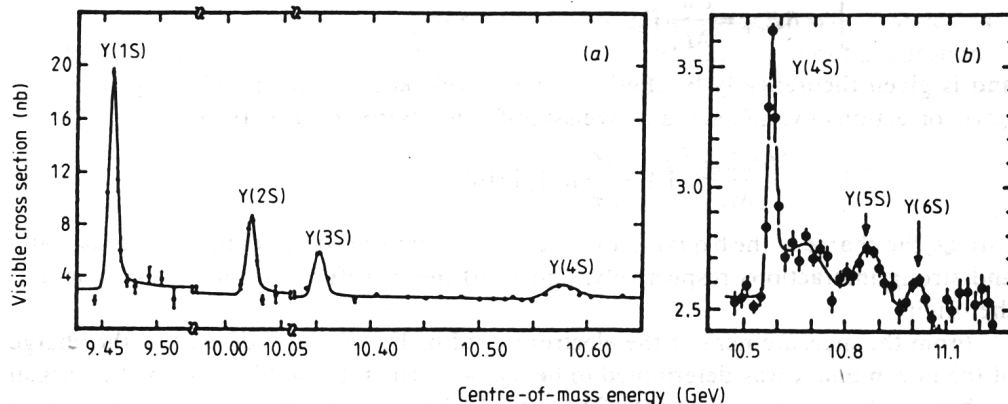
Figure 1.1: The e^+e^- cross section of an energy region around the $\Upsilon(4S)$ resonance [24–26].

hadrons, especially charm and bottom hadrons, have been measured. The lifetime of these hadrons have been measured precisely as average lifetime as well as depending on the hadron composition [27]. Several elements of the Cabbibo-Kobayashi-Maskawa matrix (see section 2.2) have been measured investigating the decay properties of c and b quarks which provide information about the weak charged current.

In today's and future B-physics experiments the study of the CP-violation in the $B\bar{B}$-system is of great interest: CLEOII at LNS is an e^+e^- experiment which is optimised to study the behaviour of B hadrons on the $\Upsilon(4S)$ resonance. In early 1999 the detector BaBar at the asymmetric B-factory PEPII at SLAC is scheduled to start its operation. The BELLE experiment is located at the Japanese asymmetric B factory KEK-B, which is also designed to work at the $\Upsilon(4S)$ resonance. At HERA, B hadrons to be analysed by the HERA-B collaboration starting 1999 are produced by collision of the proton beam halo with an internal wire target.
A new energy era in particle physics will be started by the LHC storage ring at CERN. The LHC is an accelerator which will bring protons into head-on collision at energies of 14 TeV. The LHC-B experiment is designed to perform precision measurements of CP-violation and rare decays using the high B production rate of the LHC. The LHC experiments ATLAS and CMS also have included B-physics into their experimental programs.

Chapter 2

Standard Model of Elementary Particle Physics

The Standard Model of elementary particle physics describes three of the four forces which transmit the interactions of fundamental particles, *i.e.*, the strong force, the electromagnetic force and the weak force. The state of today's knowledge about the smallest constituents of matter and their intermediate forces was developed in the second half of this century. Elementary particles are quarks, leptons and the bosons which are responsible for the transmission of the corresponding forces. The most familiar of these forces, gravity, is not included in this theory. So far a consistent quantum theory of gravity does not exist. It is the weakest of the four forces and has a negligible effect at the subatomic scale. The strong, the weak and the electromagnetic force are described by gauge theories based on the symmetry group $SU(3) \otimes SU(2) \otimes U(1)$. In order to have a complete symmetry nowadays physicists try to include the Standard Model into a Grand Unified Theory (GUT). In the following the basic principles of the Standard Model are described.

2.1   Quantum Chromo Dynamics

The strong force acts between quarks. Hence it is responsible to form particles like protons and nucleons. It is the strongest of the four forces with the shortest interaction distance. The gauge theory of the strong interaction is called Quantum Chromo Dynamics (QCD) [28]. The structure of this theory is non-Abelian and is based on the symmetry group $SU(3)_C$. In analogy to the electromagnetism a

charge - called colour - is introduced. Each quark can exist in three different colour states. The quarks are arranged in a triplet which stands for the three colours. The colour charges are intermediated by massless bosons - the gluons. However, unlike the photon, which is neutral, the gluons themselves carry colour charge and can therefore interact with each other. Gluons occur in eight different states, which correspond to the number of generators of the group $SU(3)_C$.

The self interaction of the gluons leads to a screening of the colour charge at small distances or high energies, respectively. This phenomenon is called *asymptotic freedom*. Therefore, the coupling constant of the strong interaction α_s has an energy dependence.
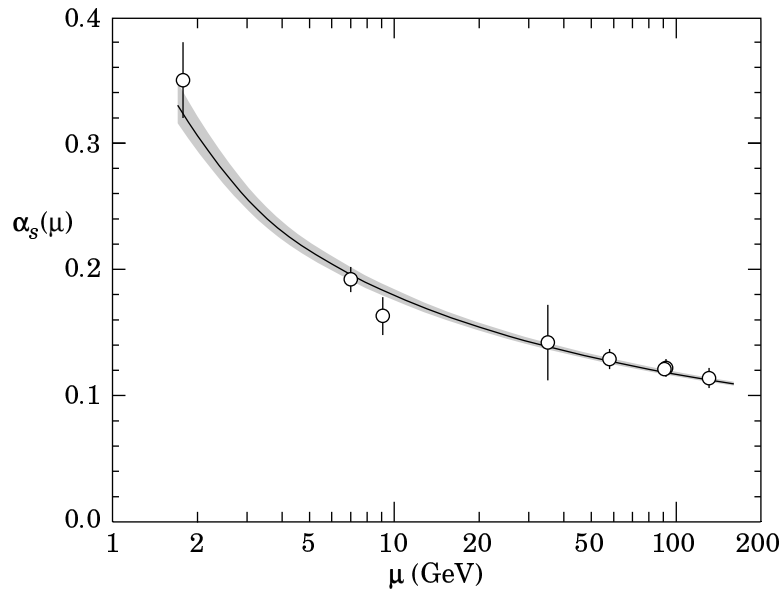

Figure 2.1: World summary of $\alpha_s(\mu)$ at the energies μ where they are measured (status 1998 [27]). The lines show the central values and the $\pm 1\sigma$ limits of the average. The figure clearly shows the experimental evidence of the decrease in $\alpha_s(\mu)$ with increasing μ. The average value for α_s at m_Z is $\alpha_s(m_Z) = 0.119 \pm 0.002$.

At LEP-I α_s was determined with high precision to [29]:

$$\alpha_s(\sqrt{s} = m_Z) = 0.121 \pm 0.003$$

This result is based on a fit to LEP-I data using observables like the ratio of leptonic and hadronic cross section, Γ_{had}/Γ_l, the width of the Z, Γ_Z, and the hadronic

cross section, σ_{had}, which are strongly α_{s} dependent and other weakly correlated fit parameters. The knowledge of the higher-order QCD corrections (see section 3.4) and their computation up to $\mathcal{O}(\alpha_{\mathrm{s}}^3)$ enables to obtain α_{s} from this quantities. Taking the results from experiments at lower energies, the expectation of an energy dependence is confirmed. Figure 2.1 shows the world summary of $\alpha_{\mathrm{s}}(\mu)$ including measurements above 100 GeV from the first data of LEP-II. Following the *confinement* hypothesis (the increase of the strong coupling with decreasing energies), quarks and gluons cannot be observed as free particles but only as colour neutral singlets of the $\mathrm{SU}(3)_{\mathrm{C}}$, the hadrons. The bound states q$\bar{\mathrm{q}}$ and qqq are called mesons and baryons, respectively. Because of increasing α_{s} at lower energies the perturbation theory is not applicable in this case. In order to describe the transition from partons (quarks and gluons) to hadrons phenomenological models are used. This transition process is called *hadronisation* or *fragmentation* and is described in section 5.1.1.

2.2 Standard Model of Electroweak Interaction

The basis for a unified description of the electromagnetic and weak interaction was created in 1961 by S.Glashow [1] as $\mathrm{SU}(2)_{\mathrm{L}} \otimes \mathrm{U}(1)_{\mathrm{Y}}$ gauge theory. This theory was extended 1967 and 1968 by S.Weinberg [3] and A.Salam [2]. They introduced massive vector bosons by the method of spontaneous symmetry breaking. This field theory is known as the *Standard Model of electroweak interaction* or *Glashow-Salam-Weinberg model*. In this scenario the vector bosons get their masses via the Higgs mechanism [30–32], which leads to an additional particle - the scalar Higgs boson.
The weak iso-spin $\vec{\mathrm{T}} = (\mathrm{T}_1, \mathrm{T}_2, \mathrm{T}_3)$ and the weak hyper-charge Y depict the general charges of the theory. They are the generators of the symmetry groups $\mathrm{SU}(2)_{\mathrm{L}}$ and $\mathrm{U}(1)_{\mathrm{Y}}$. The electrical charge is related to the hyper-charge and the third component of the iso-spin by the formula:

$$Q = T_3 + Y. \tag{2.1}$$

The Lagrangian of the electroweak interaction of gauge bosons with a fermion field is of the following form:

$$
\begin{aligned}
\mathcal{L} = \; & \bar{\psi} i \gamma^{\mu} \partial_{\mu} \psi \\
& - \frac{g_1 g_2}{\sqrt{g_1^2 + g_2^2}} A_{\mu} J_{EM}^{\mu} \\
& - \sqrt{g_1^2 + g_2^2} \, Z_{\mu} J_{NC}^{\mu} \\
& - \frac{g_2}{\sqrt{2}} (W_{\mu}^+ J_{CC}^{\mu+} + W_{\mu}^- J_{CC}^{\mu-}).
\end{aligned}
\tag{2.2}
$$

ψ and $\bar{\psi}$ are spinors which represent all fermions, particles with spin $\frac{1}{2}$. A_{μ} is the photon field, Z_{μ} and $W_{\mu}^{\pm}$ are the gauge fields of the neutral and charged weak current, which correspond to the massive gauge bosons Z and $W^{\pm}$, respectively. They arise from the spontaneous symmetry breaking within the Higgs mechanism from the original massless fields $W_{\mu}^{1,2,3}$ and B_{μ} in the Standard Model Lagrangian by:

$$
\begin{aligned}
W_{\mu}^{\pm} &= \frac{1}{\sqrt{2}} [W_{\mu}^1 \pm W_{\mu}^2] \\
A_{\mu} &= \cos\theta_W B_{\mu} + \sin\theta_W W_{\mu}^3 \\
Z_{\mu} &= -\sin\theta_W B_{\mu} + \cos\theta_W W_{\mu}^3.
\end{aligned}
\tag{2.3}
$$

θ_{W} is the electroweak mixing angle and is a fundamental parameter of the Standard Model. The identification of A_{μ} with the photon field leads to a relation of the couplings e, g_1, and g_2 with the weak mixing angle:

$$
e = \frac{g_1 g_2}{\sqrt{g_1^2 + g_2^2}} = g_1 \cdot \cos\theta_W = g_2 \cdot \sin\theta_W.
\tag{2.4}
$$

The electromagnetic (J_{EM}^{μ}), the weak neutral (J_{NC}^{μ}), and the weak charged current (J_{CC}^{μ}) can be written as:

$$
\begin{aligned}
J_{EM}^{\mu} &= \bar{\psi} \gamma^{\mu} (\mathbf{T_3} + \mathbf{Y}) \psi \\
J_{NC}^{\mu} &= \bar{\psi} \gamma^{\mu} \mathbf{T_3} \psi - \sin^2\theta_W J_{EM}^{\mu} \\
J_{CC}^{\mu\pm} &= \bar{\psi} \gamma^{\mu} (\mathbf{T_1} \pm i\mathbf{T_2}) \psi.
\end{aligned}
$$

$$
\tag{2.5}
$$
$$
\tag{2.6}
$$
$$
\tag{2.7}
$$

Here, $\mathbf{T_{1,2,3}}$ and $\mathbf{Y}$ are matrices with the dimension of the corresponding spinors. As in the one-dimensional case, $\mathbf{T_3}$ and $\mathbf{Y}$ are related by formula 2.1. For a specific fermion anti-fermion pair the currents can be written as:

$$
\begin{aligned}
J^\mu_{EM} &= Q\bar{f}\gamma^\mu f & (2.8) \\
J^\mu_{NC} &= \frac{1}{2}\bar{f}\gamma^\mu(g^f_V - g^f_A\gamma_5)f & (2.9) \\
J^\mu_{CC} &= \frac{1}{2}\bar{f}\gamma^\mu(1 - \gamma_5)f. & (2.10)
\end{aligned}
$$

The vector coupling, g^f_V, and the axial-vector coupling, g^f_A, can be expressed by:

$$
\begin{aligned}
g^f_V &= T^f_3 - 2Q^f \sin^2\theta_W & (2.11) \\
g^f_A &= T^f_3, & (2.12)
\end{aligned}
$$

where T^f_3 is the third component of the weak iso-spin and Q^f the fermion charge. The structure of the formulae 2.9 and 2.10 is called (V-A) form. Pure (V-A) coupling, *i.e.* $(1 - \gamma_5)$, means that only left-handed fermions interact. The operator $(1 - \gamma_5)$ projects out the left-handed component of the field. Hence, the weak charged current acts only on the left-handed fermion doublets, whereas the weak neutral current acts on both components of the fermion field. The charged current is 100% parity violating and in addition not flavour conserving. The parity violating of the weak currents is a fundamental characteristic of the Standard Model.

The structure of all fermion generations and their properties are summarised in table 2.1. The quark types with a prime represent a mixture of d, s, and b mass eigenstates. This mixture can be described by:

$$
\begin{pmatrix} d' & s' & b' \end{pmatrix} = \begin{pmatrix} V_{ud} & V_{us} & V_{ub} \\ V_{cd} & V_{cs} & V_{cb} \\ V_{td} & V_{ts} & V_{tb} \end{pmatrix} \begin{pmatrix} d \\ s \\ b \end{pmatrix} \tag{2.13}
$$

where the 3×3 matrix is known as Cabibbo-Kobayashi-Maskawa (CKM) mixing matrix [10, 33].

	fermion generation			I	T_3	Y	Q	C
	I	II	III					
leptons	$\begin{pmatrix} \nu_e \\ e \end{pmatrix}_L$	$\begin{pmatrix} \nu_\mu \\ \mu \end{pmatrix}_L$	$\begin{pmatrix} \nu_\tau \\ \tau \end{pmatrix}_L$	$+\frac{1}{2}$ $+\frac{1}{2}$	$+\frac{1}{2}$ $-\frac{1}{2}$	$-\frac{1}{2}$ $-\frac{1}{2}$	0 -1	0 0
	ν_{eR}	$\nu_{\mu R}$	$\nu_{\tau R}$	0	0	0	0	0
	e_R	μ_R	τ_R	0	0	-1	-1	0
quarks	$\begin{pmatrix} u \\ d' \end{pmatrix}_L$	$\begin{pmatrix} c \\ s' \end{pmatrix}_L$	$\begin{pmatrix} t \\ b' \end{pmatrix}_L$	$+\frac{1}{2}$ $+\frac{1}{2}$	$+\frac{1}{2}$ $-\frac{1}{2}$	$+\frac{1}{6}$ $+\frac{1}{6}$	$+\frac{2}{3}$ $-\frac{1}{3}$	r,g,b r,g,b
	u_R	c_R	t_R	0	0	$+\frac{2}{3}$	$+\frac{2}{3}$	r,g,b
	d_R	s_R	b_R	0	0	$-\frac{1}{3}$	$-\frac{1}{3}$	r,g,b

Table 2.1: The structure and the properties of leptons l (l = e, μ, τ), their neutrinos and u and d type quarks (u = u,c,t, d = d,s,b) in the Standard Model is visualised by their quantum numbers T_3 and Y. The prime at the left-handed down type quarks indicates that they are mixtures of the different mass eigenstates. The colour quantum number, C, is non-zero only for quarks and has three possible states: red, green, blue. Right-handed neutrinos are hypothetical, there is no indication for their existence. Indices L and R denote left-handed and right-handed fermions.

With the assumption that the neutrinos are massless, the Minimal Standard Model[1] (MSM) has 18 free parameters:

- the coupling constants α_s, α_{QED} and $\sin^2 \theta_W$

- the masses of the leptons m_e, m_μ, m_τ

- the masses of the quarks m_u, m_d, m_c, m_s, m_t, m_b

- the masses of the bosons m_Z, m_H

- the parameters of the Cabbibo-Kobayashi-Maskawa mixing matrix of the quark sector ϑ_1, ϑ_2, ϑ_3 and δ

In case of massive neutrinos[2] there are seven additional parameters for lepton masses and a mixing matrix for this sector. In further extensions of the Minimal

---

[1] There are more complicated extensions of the Standard Model. Here, the word 'Minimal' is added to describe the version containing one doublet of Higgs fields.

[2] Recent results from the Super-Kamiokande experiment [34] give evidence for neutrino oscillations and hence for neutrino masses.

Standard Model the number of free parameters increases for additional Higgs or gauge bosons.

However, the MSM has a number of problems, and it is commonly accepted that it is an approximation at the electroweak scale of a more fundamental theory. Outside that scale particle masses receive quadratically divergent contributions which require either an extremely difficult fine tuning of the Higgs potential or, *e.g.*, the introduction of a new symmetry, called *supersymmetry* (SUSY). In this model each fundamental Standard Model particle has a supersymmetric partner, associated with transformations which change the spin by half a unit. The search for SUSY particles is an important part of the current experimental program of LEP-II.

Chapter 3

Physics of Heavy Quarks at LEP-I

As described in the sections before the (V-A) structure of the weak currents and hence the parity violation of the weak interaction is a fundamental property of the Standard Model of the electroweak interaction. Since the Standard Model does not predict the strength of the couplings experimental results are needed to confirm the theory.

At LEP, the effective neutral current couplings of heavy quarks can be measured through the partial Z decay widths of the processes $Z \to b\bar{b}$ and $Z \to c\bar{c}$, denoted as $\Gamma_{b\bar{b}}$ and $\Gamma_{c\bar{c}}$, respectively and the angular distribution of the produced heavy quarks relative to the beam axis.

The measurement of $R_b^0 = \frac{\Gamma_{b\bar{b}}}{\Gamma_{had}}$, the relative decay width of the Z into b quarks, presented here provides a sensitive environment to detect a signal for physics beyond the Standard Model. Vertex corrections render it sensitive to the top mass. By construction, other corrections such as QED or QCD corrections or electroweak corrections to the Z propagator, *e.g.*, corrections which depends on the unknown Higgs mass, are negligible.

Further topics of heavy quark physics at LEP-I are, *e.g.*, measurements of hadron lifetimes, the measurement of exclusive branching fractions, and spectroscopy. Within the scope of this thesis results from these fields are only taken into account in the discussion of the error contributions.

3.1 Production and Decay of Heavy Quarks

Since free quarks (and gluons) have never been observed, the investigation of the electroweak couplings of the quarks at LEP is only possible via e^+e^- annihilations to hadrons, built by this quarks. The evolution of the processes with hadronic final states can be subdivided into four different steps; beginning from the pair production of the quarks to the formation of stable particles, which will be detected by the experimental apparatus. The phases correspond to different time and length scales [35]. Figure 3.1 shows a schematic view of the whole process.

- **electroweak phase** (10^{-19}m): the decay of the Z is an electroweak process and thus subjected to all necessary electroweak corrections. This phase of the process ends when the quark anti-quark pair and a number of initial and final state photons have been produced. Only those photons radiated from the primary final state quark anti-quark pair are counted as final state radiation.

- **perturbative QCD phase** (10^{-17}m): In the perturbative phase of QCD the momentum transfer between the quarks and the gluons - if radiated - is rather large corresponding to small interaction distances and relatively small values of the strong coupling constant, α_s. In this regime perturbative theory is applicable. Two different methods are used for the calculation inside the perturbative theory [36]. The matrix element algorithm (ME) calculates the scattering matrix elements completely up to a certain order of α_s. Calculations are available up to α_s^2 which means that the perturbative phase can end with at maximum 4 partons (gluons and quarks). The parton shower algorithm (PS) accounts for all orders in α_s but only the leading terms. In some cases additional terms, *e.g.*, the next to leading logarithms, are included. This model is especially suited for Monte Carlo applications and is used within this analysis. The perturbative phase of QCD stops when the momentum transfer becomes too small (some GeV) and thus the coupling constant is too large to allow further perturbative steps. The resulting particles from this phase are quarks and gluons and are called final state partons.

- **non-perturbative QCD phase** (10^{-15}m): The process to build colourless hadrons from quarks is called *hadronisation* or *fragmentation*. Since there

is no theory which can describe this phase completely models have to be introduced. The models are characterised by many parameters, which are not based on an underlying consistent theory but which are mostly empirically motivated. This implies that model uncertainties have to be taken into account. Variables which are used to quantify the uncertainties are explained below.

- **particle decay phase** ($> 10^{-15}$m): In order to compare theory with data one has to account for decays of unstable hadrons. Many of these decays are well understood from measurements in low-energy experiments. But in case of heavy-flavoured hadrons still some uncertainties remain because not all decay modes have been measured.
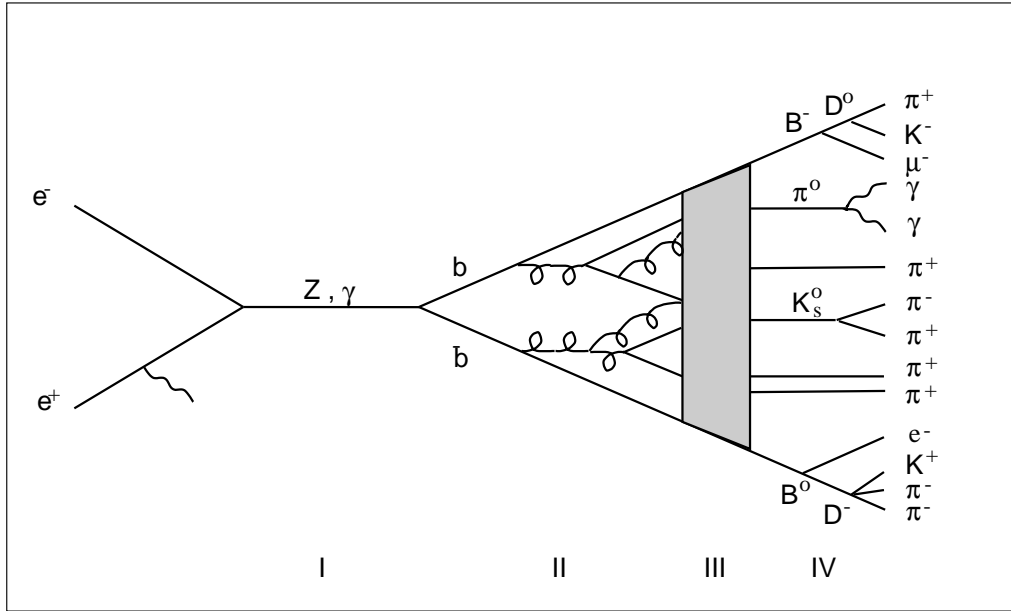
Figure 3.1: The four phases of the quark production in e^+e^- collisions as example of a $b\bar{b}$ event: electroweak part (I), perturbative QCD part (II), non-perturbative QCD part (III) and the decay of unstable hadrons into detectable particles (IV).

In order to deduce the properties of the underlying quarks one has to assume some model for the fragmentation process. Several models have been proposed in the last years: independent *jet* models [37], *string* fragmentation models [38, 39] and *cluster* fragmentation models [40–43].

The string model has been popularised by the Lund Monte Carlo JETSET [44] and has become the model commonly used for the e^+e^- annihilation to hadrons in recent years. String models are based on the idea that, if the primary two quarks move apart, a *colour flux tube* (string) stretches between them. As soon as the potential energy is high enough to build a q$\bar{q}$ pair, the string tears into two parts. The quarks and anti-quarks from adjacent breaking can then form mesons.

Particle	Fraction [%]
B^- ($\bar{u}b$)	$39.7^{+1.8}_{-2.2}$
$\bar{B}^0$ ($\bar{d}b$)	$39.7^{+1.8}_{-2.2}$
$\bar{B}_s$ ($\bar{s}b$)	$10.5^{+1.8}_{-1.7}$
Λ_b (udb)	$10.1^{+3.9}_{-3.1}$

Table 3.1: Fraction of different B hadrons in a sample of weakly decaying B hadrons [27].

Although well founded on the QCD, the model still contains many parameters controlling transverse and longitudinal momentum, baryon production etc. However, because energy and momentum are conserved at each step in the string fragmentation, no artificial procedure has to be applied to join up the last hadrons. Baryon production is included by the production of diquark anti-diquark pairs at some of the string breaks.

In order to parameterise the amount of momentum (or energy) carried by the initial quarks ends up in each of the hadrons produced during the fragmentation process the following variable is commonly used:

$$z = \frac{(E + p_{\parallel})_{hadron}}{(E + p_{\parallel})_{quark}}.$$ (3.1)

E is the energy and $p_{\parallel}$ the momentum component along the initial quark direction. In the Lund string model the Peterson fragmentation function [45] is used to describe the fragmentation of heavy quarks:

$$f(z) = \frac{1}{z(1 - (1/z) - \epsilon_q/(1 - z))^2}.$$ (3.2)

Here ϵ_q is a free parameter and its value decrease with increasing mass of the initial quark, $\epsilon_q \sim 1/m_q^2$. Experimentally one observes the quantity:

$$x_E = \frac{E_{hadron}}{E_{beam}}.$$
(3.3)

Using the relation of z and x_E from the Monte Carlo one can study the fragmentation function and the agreement of the model with data. The LEP experiments have measured the mean retained hadron energy of b and c quarks [46] to be $\langle x_E \rangle_b = 0.702 \pm 0.008$ and $\langle x_E \rangle_c = 0.484 \pm 0.008$.

There is a functional dependence between the charge multiplicity of hadronic events, $\langle n \rangle$, and the initial quark energy [47]. Results from measurements of $\langle n \rangle$ are used to estimate the heavy quark fragmentation function. The most accurate measurement of the charged decay multiplicities of D^+, D^0, and D_s mesons are from the MARKIII collaboration [48]. Applying an averaging procedure which takes into account the separate uncertainties weighted by their relative contributions, an average D decay multiplicity of $\langle n \rangle_c = 2.53 \pm 0.06$ can be obtained. The LEP collaborations have measured the average decay multiplicity of the b decay [49–51]. The combined result is $\langle n \rangle_b = 4.955 \pm 0.062$ [52] and hence found to be about two times larger than for charm mesons.
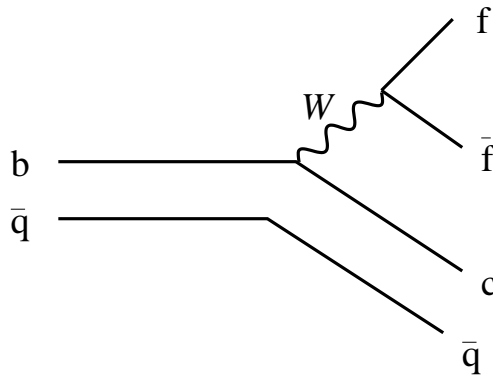
Figure 3.2: Standard Model charged current decay of the b quark. The quark line below is called the 'spectator' quark. The spectator model one possible description for the decay of the B hadron. f$\bar{\text{f}}$ can be a lepton anti-neutrino pair as well as a quark anti-quark pair.

At high-energy collider experiments b quarks hadronise as $\bar{B}^0, B^-, \bar{B}_s$, and B_c^- mesons or as baryons containing b quarks. B mesons decay mainly weakly via

the charged current process depicted in figure 3.2. The B hadron sample composition of weakly decaying B hadrons at the Z resonance is shown in table 3.1. A summary of properties of bottom and charm hadrons are shown in table 3.2.

Particle	Mass [MeV/c^2]	τ [10^{-12} s]	$c\tau$ [μm]	Br(X $\rightarrow l^-$ anything) [%]
B$^-$	5278.9 $\pm$ 1.8	1.65 $\pm$ 0.04	495	10.3 $\pm$ 0.9
B^0	5279.2 $\pm$ 1.8	1.56 $\pm$ 0.04	468	10.5 $\pm$ 0.8
B$_s$	5369.3 $\pm$ 2.0	1.54 $\pm$ 0.07	462	8.1 $\pm$ 2.5
D$^-$	1869.3 $\pm$ 0.5	1.057 $\pm$ 0.015	317	17.2 $\pm$ 1.9
$\bar{\text{D}}^0$	1864.5 $\pm$ 0.5	0.415 $\pm$ 0.004	124	6.75 $\pm$ 0.29
D$_s$	1968.5 $\pm$ 0.6	0.447 $\pm$ 0.017	134	8^{+6}_{-5}

Table 3.2: Summary of properties of weakly decaying bottom and charm mesons [27]. The branching ratio of B$_s$ is not a pure measurement and related to the channel $\bar{\text{B}}_s \rightarrow \text{D}_s^+ l^-$ anything.

3.2 Partial Decay Width

As mentioned before, high energy e$^+$e$^-$ annihilations into fermion anti-fermion pairs could establish the weak iso-spin doublet character of the b quarks by measuring their vector and axial-vector couplings to the Z boson. Annihilations at centre-of-mass energies around the Z resonance (LEP-I, SLC) proceed predominantly via e$^+$e$^-$ $\rightarrow$ Z $\rightarrow$ f$\bar{\text{f}}$. f is any fermion except the top quark which is too heavy to be produced at LEP-I energies. In contrast, at previous colliders (PEP, PETRA, KEK) the process e$^+$e$^-$ $\rightarrow \gamma \rightarrow$ f$\bar{\text{f}}$ was dominant with some sensitivity to the γ-Z interference term.

In the lowest-order (Born) approximation and taking the Z exchange only, the cross section shows the typical Breit-Wigner resonance behaviour:

$$\sigma^0(e^+e^- \rightarrow Z \rightarrow f\bar{f}) = \frac{12\pi s}{m_Z^2} \frac{\Gamma_{Z \rightarrow e^+e^-} \Gamma_{Z \rightarrow f\bar{f}}}{(s - m_Z^2)^2 + m_Z^2 \Gamma_Z^2} \cdot \tag{3.4}$$

If the centre-of-mass energy, $\sqrt{s}$, is exactly equal to the Z mass, m$_Z$, the cross section can be written as:
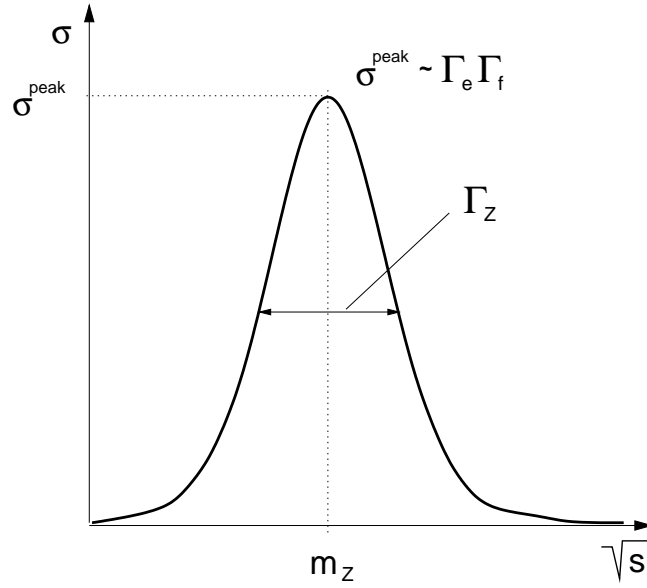
Figure 3.3: Depiction of the Born cross section of the process $e^+e^- \to Z \to f\bar{f}$ at energies around the Z mass. The resonance behaviour can be clearly seen. Fundamental observables like the Z mass, the width of the Z and the peak cross section can be extracted.

$$\sigma^0\left(e^+e^- \to Z \to f\bar{f}\right)\big|_{\sqrt{s}=m_Z} = 12\pi\frac{\Gamma_{Z\to e^+e^-}\Gamma_{Z\to f\bar{f}}}{m_Z^2\Gamma_Z^2} \, . \tag{3.5}$$
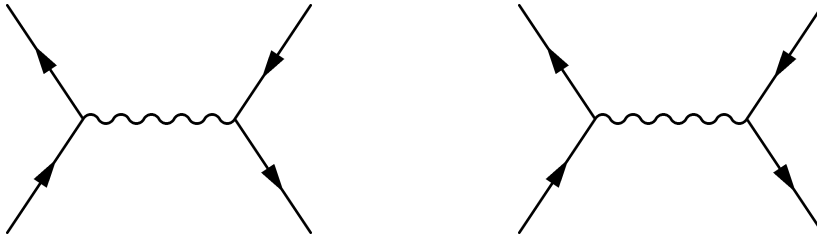
Figure 3.4: Lowest order Feynman diagrams for $e^+e^- \to f\bar{f}$ where f is any fermion.

The partial decay width of the Z to a particular $f\bar{f}$ pair can be expressed as a function of the coupling constants [53] by:

$$\Gamma_{Z \to f\bar{f}} = \frac{G_F m_Z^3 \beta_f}{6\pi\sqrt{2}}[(1 + 2\eta_f)((g_V^f)^2 + (g_A^f)^2) - 6\eta_f(g_A^f)^2]N_C \,, \qquad (3.6)$$

where $\eta_f = m_f^2/m_Z^2$, $\beta = \sqrt{1 - 4\eta_f}$ and N_C the colour factor which is equal 3 for quarks and 1 for leptons. The Fermi decay constant, G_F, replaces the coupling g which appears in equation 2.2 and was measured very precisely from the muon decay [54].

As can be seen from formula 3.5, the partial decay width of the Z into a certain fermion is directly proportional to the corresponding pole cross section. By forming the ratio of the widths all constant terms cancel. The relative production of b quarks at the Z pole given by the ratio of the width of the decay $Z \to b\bar{b}$ to the total hadronic width can be measured by the ratio of the corresponding cross sections:

$$R_b^0 \equiv \frac{\Gamma_{Z \to b\bar{b}}}{\Gamma_{Z \to hadrons}} = \frac{\sigma^0(e^+e^- \to Z \to b\bar{b})}{\sigma^0(e^+e^- \to Z \to q\bar{q})}\Bigg|_{\sqrt{s}=m_Z} \qquad (3.7)$$

The observable which can be measured at the Z pole:

$$R_b = \frac{\sigma^0(e^+e^- \to b\bar{b})}{\sigma^0(e^+e^- \to q\bar{q})}\Bigg|_{\sqrt{s}=m_Z} \qquad (3.8)$$

includes a contribution coming from the photon exchange. The contribution to R_b has been evaluated using the ZFITTER program [55, 56] to be $R_b^0 = R_b + 0.0003$ and is taken into account.

Using equation 3.6, G_F and m_Z cancel, leaving a result in terms of vector and axial-vector couplings of the Z to each type of quark, q, accessible at LEP-I. At energies around the Z mass - assuming $\eta_b \simeq (0.05)^2$ and hence $\beta \simeq 1$ - equation 3.7 can be written as:

$$R_b^0 \simeq \frac{(g_V^b)^2 + (g_A^b)^2}{\sum_{q=1,5}((g_V^q)^2 + (g_A^q)^2)} \qquad (3.9)$$

Assuming $\sin^2\theta_W \simeq 0.23$ [57], $R_b \simeq 0.2$ is obtained; in about 20% of the cases where the Z decays hadronically it decays into b quarks. The influence of higher order (radiative) corrections is discussed in section 3.4.

3.3   Forward-Backward Asymmetry

Another access to direct information about the coupling constants in the electroweak sector is the measurement of the angular distribution of the final state fermions.
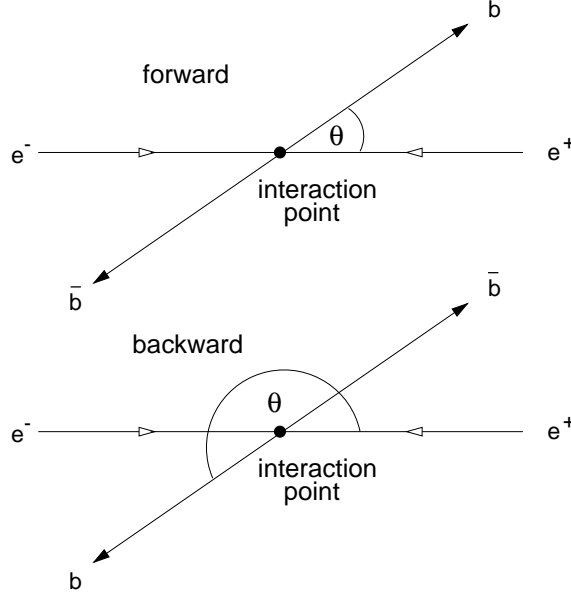

Figure 3.5: Definition of forward and backward $e^+e^- \to b\bar{b}$ events. θ is the angle between the directions of the incoming electron and the outgoing b quark.

For pure photon exchange, the process is forward-backward symmetric. The differential cross section can be described as follows:

$$\frac{d\sigma(e^+e^- \to \gamma \to f\bar{f})}{d\cos\theta} \propto 1 + \cos^2\theta. \tag{3.10}$$

Because of the parity violating nature of the weak interaction as discussed in section 2.2, the Z exchange leads to a forward-backward asymmetry and a modified differential cross section:

$$\frac{d\sigma(e^+e^- \to Z,\gamma \to f\bar{f})}{d\cos\theta} \propto 1 + \cos^2\theta + \frac{8}{3}A_{FB}^f\cos\theta. \tag{3.11}$$

As can be seen from figure 3.5, $e^+e^- \rightarrow b\bar{b}$ events may be classified as *forward* or *backward* according to whether the projection of the outgoing b momentum along the beam line is parallel or anti-parallel to the direction of the incident electron. The asymmetry, A_{FB}^b, is defined in terms of the cross sections σ_F for 'forward' and σ_B for 'backward' events:

$$A_{FB}^b \equiv \frac{\sigma_F - \sigma_B}{\sigma_F + \sigma_B} \tag{3.12}$$

Neglecting the contributions from virtual photon exchange, the asymmetry at the Z peak can be expressed as the product of two terms, one results from the annihilation of the e^+e^- pair, the other from the decay $Z \rightarrow b\bar{b}$:

$$A_{FB}^{0,b} = \frac{3}{4}\mathcal{A}_e\mathcal{A}_b \tag{3.13}$$

where $\mathcal{A}_{e,b}$ are given by

$$\mathcal{A}_f = \frac{2\,g_V^f g_A^f}{(g_V^f)^2 + (g_A^f)^2} = \frac{2\,\frac{g_V^f}{g_A^f}}{1 + (\frac{g_V^f}{g_A^f})^2} \qquad (f = e, b) \tag{3.14}$$

For $\sin^2\theta_W \simeq 0.23$ one obtains $A_{FB}^b \simeq 0.10$, a forward-backward asymmetry of b quark production of about 10%.
With the two observables R_b^0 and $A_{FB}^{0,b}$ (3.7 and 3.14) it is possible to calculate the vector and axial-vector couplings from b quarks to the Z boson. It is important to stress that measurements of $A_{FB}^{0,b}$ at LEP can only measure the product $\mathcal{A}_e\mathcal{A}_b$.

However, $\mathcal{A}_b$ can be measured directly if a significant longitudinal polarisation P_e is present in the electron or positron beam using the left-right forward-backward asymmetry:

$$A_{FB}^{LR,b} \equiv \frac{\sigma_{LF}^b - \sigma_{LB}^b - \sigma_{RF}^b + \sigma_{RB}^b}{\sigma_{LF}^b + \sigma_{LB}^b + \sigma_{RF}^b + \sigma_{RB}^b} = \mathcal{A}_b P_e|_{\sqrt{s}=m_Z} \tag{3.15}$$

With a known polarisation P_e, $\mathcal{A}_e$ can be derived directly from the left-right asymmetry between the cross section of left-handed and right-handed electrons:

$$A^e_{LR} \equiv \frac{\sigma_L - \sigma_R}{\sigma_L + \sigma_R} = \mathcal{A}_e P_e|_{\sqrt{s}=m_Z} \qquad (3.16)$$

This is currently possible only at SLC using a longitudinally polarised electron beam. $\mathcal{A}_e$ can also be measured at LEP exploiting the τ polarisation as the function of the polar τ production angle [58].

3.4 Radiative Corrections

For a given process of interest, the Feynman rules derived from the Standard Model Lagrangian allow to calculate the corresponding matrix elements and hence the differential cross sections. For a given final state, however, the most simple diagram, the Born diagram, does not always describe the measurements sufficiently. In order to get more precise theoretical predictions it is necessary to incorporate more complicated diagrams leading to the same final state. Because of arising mathematical problems in calculating higher-order corrections, a consistent procedure is used to redefine the ingredients of the Lagrangian - such as the coupling constants, wave functions and propagators - in order to recover finite expressions. The application of such a procedure to a quantum field theory is called renormalisation. There are two schemes of renormalisation widely used: the modified minimal-subtraction ($\overline{\text{MS}}$) scheme and the on-shell renormalisation. In the following the on-shell scheme is used. A detailed discussion and a list of references can be found in [59].

The radiative corrections need to be considered in the process $e^+e^- \rightarrow f\bar{f}$ are summarised in the following groups of Feynman graphs:

- **QED corrections** - contain all diagrams with an extra photon added to the Born diagrams either as a real bremsstrahlung photon or virtual photon loop in the initial or final state. These are illustrated in figure 3.6.

- **Weak corrections** - include all other loop diagrams involving electroweak bosons. These can be divided into those which involve corrections to the γ or Z propagator, also called self-energy correction (figure 3.7a), a set of vertex corrections (figure 3.7b) and contributions from box diagrams (figure 3.8a).

- **QCD corrections** - arise from gluon radiation from real and virtual quarks characterised by diagrams as shown in figure 3.8b. They affect the final state and appear in $q\bar{q}$ only.
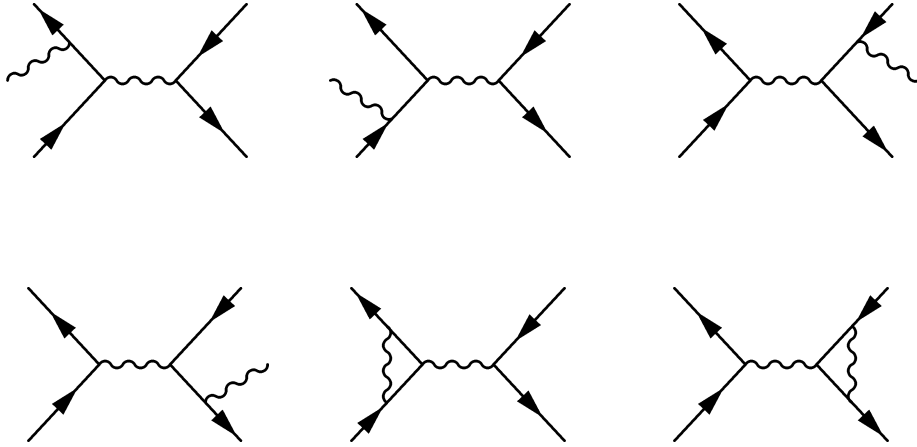

Figure 3.6: Most important QED corrections to $e^+e^- \rightarrow f\bar{f}$ around the Z resonance. The wiggly lines without specifications are photons.

Considering the corrections appearing to R_b , only the parts of the Feynman graphs concerning the Z boson and γ, the final state fermions and the corresponding vertices are relevant.

A good approach in describing electroweak corrections at energies around the Z resonance is the concept of running coupling constants. They are defined in such a way that the results at LEP are a measure of these couplings at the scale $q^2 \simeq m_Z^2$. In the on-shell renormalisation scheme the weak mixing angle is defined uniquely through the gauge boson masses:

$$\sin^2\theta_W \equiv 1 - \frac{m_W^2}{m_Z^2} \quad \text{and} \tag{3.17}$$

$$m_W^2 \sin^2\theta_W = \frac{A_0^2}{1 - \Delta r} \tag{3.18}$$
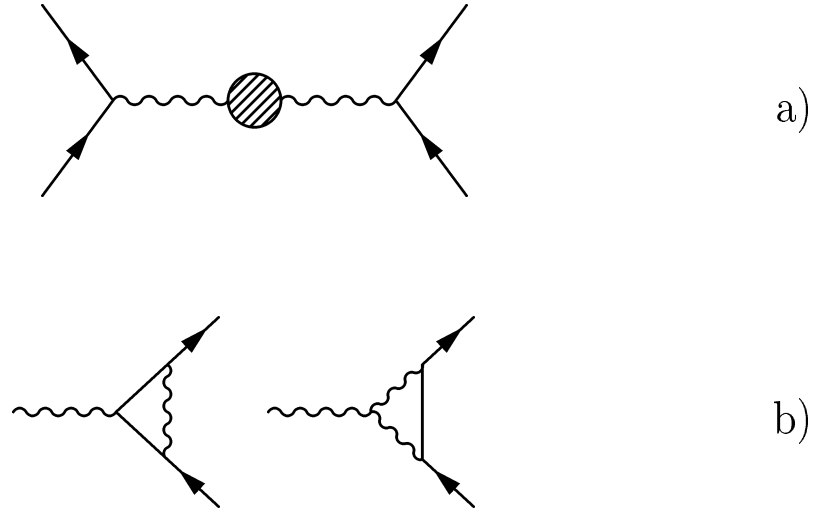
Figure 3.7: a) Propagator corrections to $e^+e^- \rightarrow f\bar{f}$: the shaded area represents a virtual loop of any of the fundamental fermions or bosons. b) Vertex corrections: the straight lines represent fermions, the wiggly lines vector bosons (W or Z).

where $A_0 = \sqrt{G_F \pi \alpha / \sqrt{2}} = 37.2802$ GeV [27] is known very precisely by measuring G_F from the muon decay $\mu \rightarrow \bar{\nu}_\mu + e + \nu_e$. Δr includes the radiative corrections relating to the dominant contribution from the photon self-energy and a much smaller term which is dominated by a quadratic top mass dependence. The effective electroweak mixing angle can be expressed by:

$$\sin^2 \theta_W^f \rightarrow \sin^2 \theta_{eff}^f = \sin^2 \theta_W \kappa^f. \qquad (3.19)$$

κ^f is a form factor that describes vertex corrections for a given fermion f. An additional form factor, ρ^f, appears in the replacement:

$$m_Z \sqrt{G_F} \rightarrow m_Z \sqrt{G_F \rho^f}. \qquad (3.20)$$

Effective vector and axial-vector couplings can be expressed in terms of this form factor by:
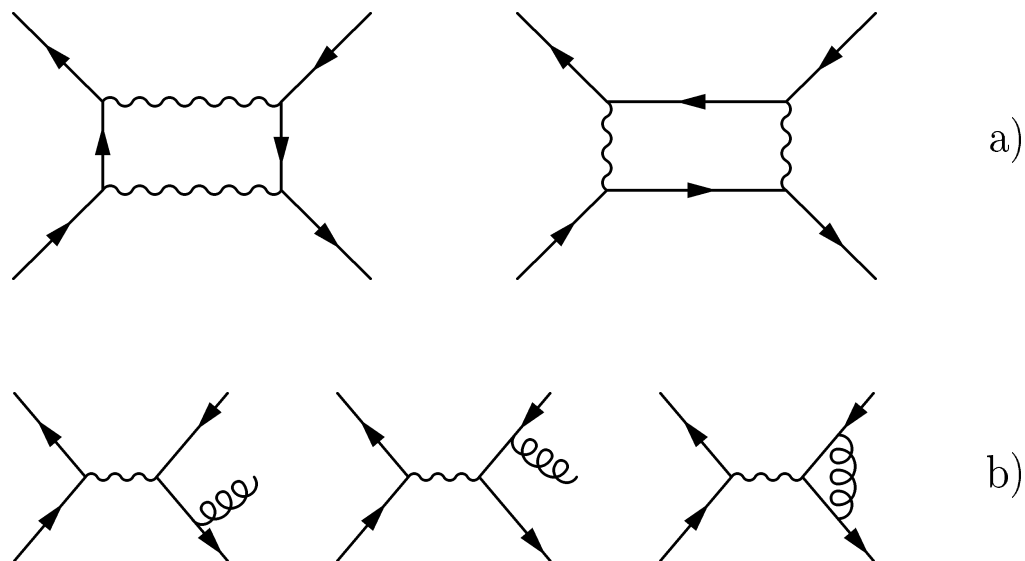
Figure 3.8: a) Typical box diagrams for the process $e^+e^- \to Z \to f\bar{f}$ and b) Feynman graphs represent QCD corrections in the process $e^+e^- \to Z \to q\bar{q}$ caused by radiated gluons.

$$g_A^f \to \bar{g}_A^f = T_3^f \sqrt{\rho^f} \tag{3.21}$$

$$g_V^f \to \bar{g}_V^f = \sqrt{\rho^f}(T_3^f - 2Q_f \sin^2\theta_{eff}^f). \tag{3.22}$$

With these transformations, the effect of electroweak radiative corrections can be absorbed in a running coupling constant $\sin^2\theta_{eff}^f$. The running of α from $q^2 = 0$ to $q^2 = m_Z^2$ is given by:

$$\alpha(m_Z^2) = \frac{\alpha(0)}{1 - \Delta\alpha(m_Z^2)}, \tag{3.23}$$

where $\Delta\alpha$ consider the self-energy to the photon propagator. At the Z pole α is determined to be [27]:

$$\alpha(m_Z^2) \simeq \frac{1}{128.8} \tag{3.24}$$

QCD corrections to the Z partial width can be expressed as an expansion of the strong coupling constant α_s and have approximately the form of a multiplicative factor:

$$f_{QCD}^f = 1 + \delta_{QCD}^f. \tag{3.25}$$

The quantity δ_{QCD}^f is equal zero for leptons and has been computed for quarks up to the order of α_s^3. The magnitude of these corrections is $\mathcal{O}(10^{-2})$. The same procedure can be applied in case of QED corrections

$$f_{QED}^f = 1 + \delta_{QED}^f \tag{3.26}$$

with $\delta_{QED}^f = 3\alpha Q_f^2/4\pi$.

Improved Born Approximation

The Born-level formulae (e.g. equation 3.6) can be used in the analysis of the LEP data, provided the coupling constants are replaced by effective constants (equations 3.21 and 3.22) at a scale $q^2 \simeq m_Z^2$. The fermionic partial width can be parameterised by the Improved Born Approximation in terms of effective vector and axial-vector couplings of the Z to fermions:

$$\Gamma_{Z \to f\bar{f}} = \frac{G_F m_Z^3 \beta_f}{6\pi\sqrt{2}}[(1 + 2\eta_f)((\bar{g}_V^f)^2 + (\bar{g}_A^f)^2) - 6\eta_f(\bar{g}_A^f)^2]N_C f_{QED}^f f_{QCD}^f \tag{3.27}$$

with the correction factors f_{QCD}^f and f_{QED}^f defined above.

For the $Z \to b\bar{b}$ final state there are additional sizable vertex corrections, arising from vertex diagrams [60–62] involving b and t quarks and W bosons, as shown in figure 3.9. The CKM matrix element V_{tb} is about 1, which results in a dominant contribution from the Wtb vertex. Due to the large top mass these contributions are significant with respect to the high precision of the LEP/SLD measurements. In the framework of running couplings the additional contributions are included by corrections with respect of the form factors of the light down type quark d:
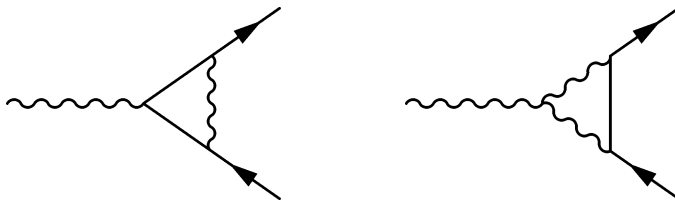
Figure 3.9: Vertex corrections to $e^+e^- \to Z \to b\bar{b}$

$$\rho_Z^b = \rho_Z^d - 2\frac{\Delta_b(m_{top}^2)}{a_b}, \qquad (3.28)$$

$$\kappa_Z^b = \kappa_Z^d + \frac{\Delta_b(m_{top}^2)}{a_b}. \qquad (3.29)$$

In the limit of large top quark masses, the correction is given by [62]:

$$\frac{\Delta_b(m_{top}^2)}{a_b} \simeq |V_{tb}|^2 \left[\frac{m_{top}^2}{m_W^2} + \left(\frac{8}{3} + \frac{1}{6\cos^2\theta_W} \right) \log \frac{m_{top}^2}{m_W^2} \right] \qquad (3.30)$$

For the decay width, $\Gamma_{Z \to b\bar{b}}$, these vertex corrections cancel most of the loop corrections due to loops of a virtual top quark; $\Gamma_{Z \to b\bar{b}}$ is weakly top mass dependent. Taking $R_b^0 = \frac{\Gamma_{b\bar{b}}}{\Gamma_{had}}$, the top quark corrections appearing in the total hadronic width cancel the loop corrections in $\Gamma_{Z \to b\bar{b}}$ and hence render it sensitive to the square of the top mass coming from the vertex correction. In contrast to R_b the relative decay width of lighter down type quarks, e.g. $R_d = \frac{\Gamma_d}{\Gamma_{had}}$, is much less sensitive to the mass of the top. Figure 3.10 shows the behaviour of R_b and R_d with respect to the top mass predicted by Standard Model calculations using the ZFITTER[1] program. It is also shown that R_b is, by construction, nearly insensitive to the mass of the Higgs boson.

---

[1]ZFITTER is the most comprehensive implementation of the radiative corrections for e^+e^- interactions at energies around the Z resonance. It is commonly used for experimental data analysis. and is based on a semi-analytical approach to fermion pair production in e^+e^- annihilation and Bhabha scattering and is using the on-shell renormalisation.
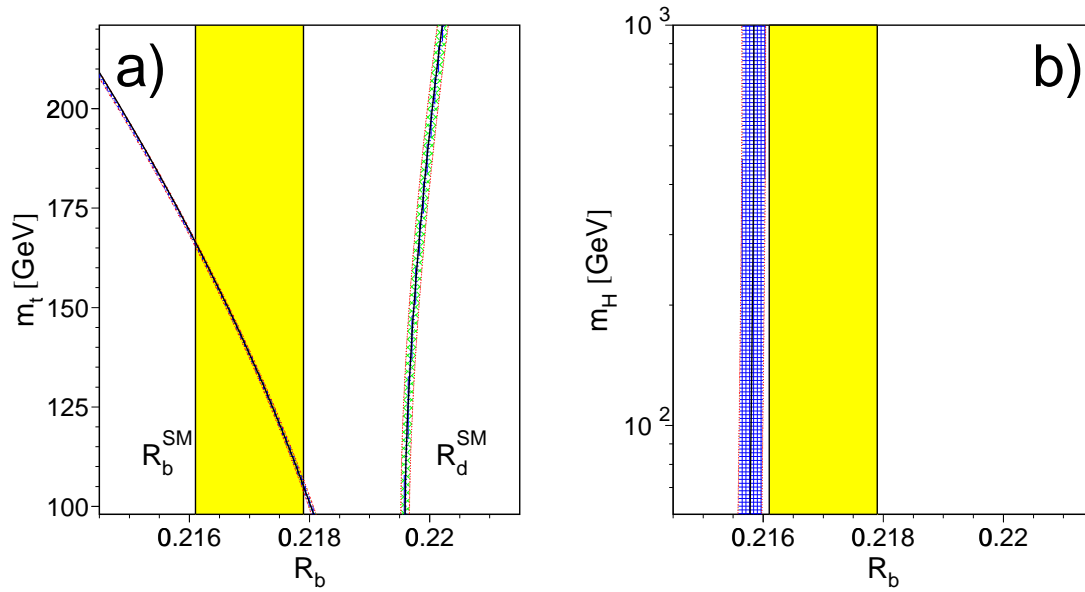
Figure 3.10: a) Standard Model predictions of R_b and R_d as a function of the mass of the top quark. The effect on the curves of varying the Higgs mass between 90 and 1000 GeV is smaller than the resolution of the lines. R_d is much less dependent on m_{top} than R_b. The band in the middle depicts the 1σ region of the latest world average of $R_b = 0.2173 \pm 0.0009$ [27]. b) Standard Model predictions of R_b as a function of the Higgs boson mass assuming a top mass of $m_{top} = 173.8 \pm 5.2$ GeV [27]. R_b is nearly independent from the Higgs mass.

3.5 Measurement of R_b at LEP-I - Experimental Review

The following Z decays have been studied at LEP-I in great detail [63, 64]:

- $e^+e^- \to q\bar{q}$ (γ) (hadronic)

- $e^+e^- \to \mu^+\mu^-(\gamma)$ (dimuon)

- $e^+e^- \to \tau^+\tau^-(\gamma)$ (tau)

- $e^+e^- \to e^+e^-(\gamma)$ (Bhabha)

The decay of the Z into a neutrino anti-neutrino pair is not visible, because neutrinos passing the detector without interaction. Only if at least one initial state photon (from a bremsstrahlung process) appears, the process $e^+e^- \to \nu\bar{\nu}\,\gamma$ can be investigated by looking for events with a single photon in the detector.

Year	1990/91	1992	1993	1994	1995	total
$\mathcal{L}$ (pb^{-1})	19.1	22.7	33.0	49.7	30.0	154.5
N_E	7	1	3	1	3	
number of events ($\times 10^3$)						
hadronic	416	678	645	1359	526	3624
dimuon	13	21	21	42	17	114
tau	10	15	20	41	17	103
bhabha	16	23	23	43	21	126

Table 3.3: Integrated luminosity $\mathcal{L}$ and number of events recorded by L3 at the Z resonance. N_E gives the number of energy points per year.

The integrated luminosity per year recorded by the L3 experiment and the corresponding number of events per channel mentioned above are given in table 3.3. The numbers for ALEPH, DELPHI and OPAL are similar. In some years the centre of mass energy was scanned over a few energy points within 2-3 GeV off the Z peak (see N_E in table 3.3).

The key for precise heavy quark physics is an efficient and so-called self-calibrating method of distinguishing (*tagging*) Z → b$\bar{\text{b}}$ decays from Z decays into lighter quarks. A self-calibrating tag allows that the efficiency can be determined directly from the data. This reduces systematic errors by minimising the dependence on Monte Carlo simulations. There are three sources of information available to identify Z → b$\bar{\text{b}}$ decays: leptons from semileptonic b decays, the shape of b jets (event shape) and the finite lifetime of the B hadrons:

- **Lepton tag**: Approximately 20% of b quarks decay semi-leptonically into electrons and muons. Due to the relatively high mass and hence the fact that a large fraction of the initial energy of the b quark is retained by the B hadron into which it fragments, about half of these decays result in a high-momentum lepton (p $\geq$ 3 GeV) with high momentum transverse to the b quark direction (p$_\perp \geq$ 1 GeV). Due to the lower c quark mass, leptons from c decays have high momenta but lower transverse momenta.

- **Event shape tag**: The method relies on the fact that the larger mass leads to slightly more isotropically distributed tracks from heavy quark events than in light quark events. However at energies around the Z mass the difference of few GeV between the quark masses is of limited consequence to achieve any discrimination. Event shapes are only used occasionally at these energies and mostly in conjunction with other methods, for instance as one of many inputs to an neural network.

- **Lifetime tag**: This method exploits the relatively long lifetime of hadrons containing b quarks and their hard fragmentation. At LEP-I energies, a weakly decaying B hadron from Z decay travels typically 2-3 mm before decaying into five charged tracks on average. There are two main variables that are used for lifetime tagging. The most straightforward one is the *decay length*, which is the distance from the interaction point to the decay point. The second variable is the *impact parameter*, which is the distance of closest approach of the track to the assumed interaction point. In contrast to the decay length, which is a joint property of a number of tracks, the impact parameter is a property of each track and can be used even when the decay vertex has not been reconstructed. With the installation of silicon vertex

detectors in the LEP experiments very accurate determinations of secondary vertex positions and impact parameters became possible.

The lifetime tag is by far the most efficient method to distinguish b events from events containing lighter quarks. Typically 20-25% of $Z \to b\bar{b}$ events are tagged with a sample purity of $\sim$90%. The full characteristics of this kind of tag and the method of 'self-calibration' will be described in detail in section 6.2. Different tags are sometimes combined into a multivariate tag which can increase the tagging efficiency.
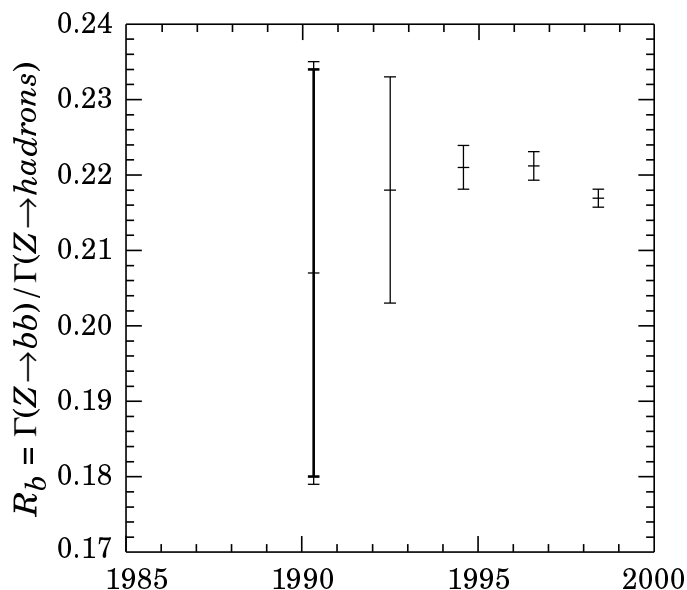
Figure 3.11: Historical perspective of R_b^0 as a function of date of publication of the *Review of Particle Physics* [27].

The first precise measurements of R_b have been presented in early 1993, when analysis of data taken with vertex detectors at LEP became possible. Since summer 1993, the situation has evolved slowly (depicted in figure 3.11), with a discrepancy of the combined average of the LEP experiments growing from about two standard deviations to more than three. The status of LEP measurements on R_b, as presented in summer 1995, is given in figure 3.12. The slow evolution can be explained by the fact, that results were systematically limited from the very beginning. Progress could only come from improved techniques and better understanding of the underlying systematic.
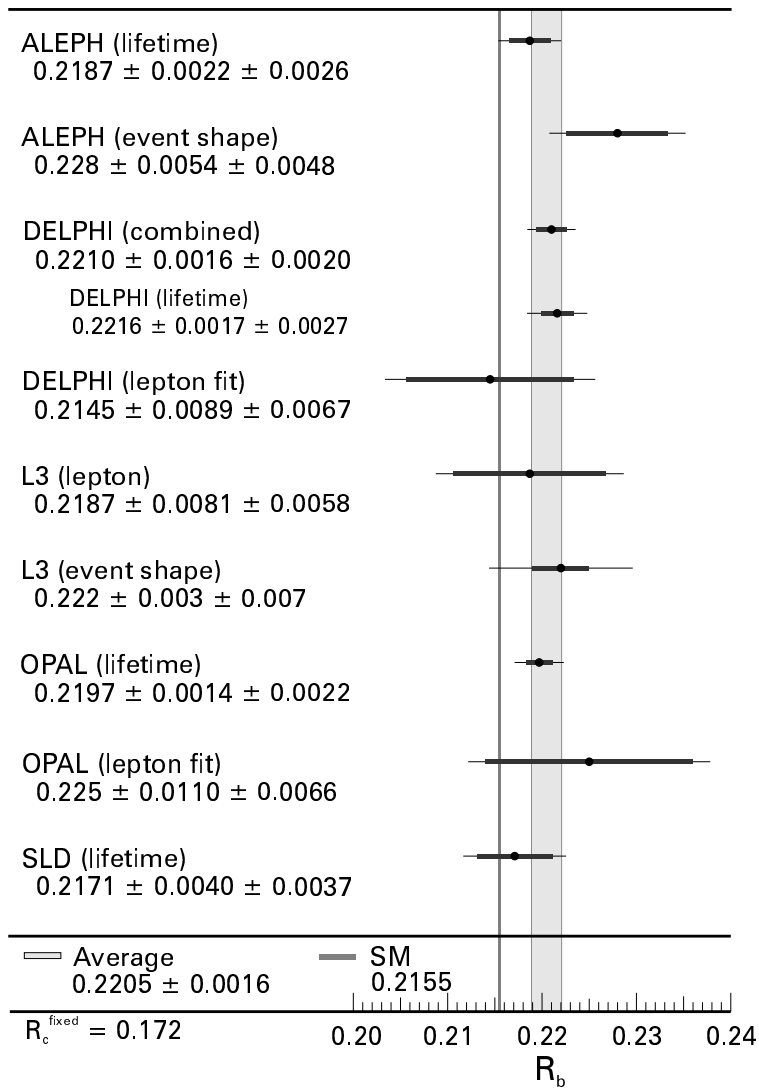
Figure 3.12: Measurements of R_b, as presented in summer 1995 [8]. Beside the total error, the contribution from statistics is given for each measurement (thick line). The left vertical band depicts the Standard Model prediction, the right one is the world average. DELPHI has presented a combined measurement. In addition the result of the lifetime tag is given.

In addition measurements of R_c have developed a discrepancy at the level of two standard deviations. The combined results in 1995 were [8]:

$$R_b = 0.2205 \pm 0.0016 \quad \text{SM Value:} \quad 0.2155 \quad \text{discrepancy:} \quad 3.1\sigma$$
$$R_c = 0.1598 \pm 0.0069 \quad \text{SM Value:} \quad 0.172 \quad \text{discrepancy:} \quad 1.8\sigma$$

with a negative correlation of - 30%. The correlation results from the fact that charm events are the main background to the $Z \rightarrow b\bar{b}$ signal.

Taking into account the difficulty of the measurement, one should check measurements and methods and trying to find out how new physics or other model dependent things could explain it, as well. Precise updated measurements of R_b are necessary and of great interest.

Chapter 4

The L3 Detector at LEP

4.1   The LEP Machine

The Large Electron Positron collider was built to study the electroweak interaction at energies of up to 200 GeV. The physics goals are twofold. The first stage (LEP-I) was started in 1989 and provided colliding beams of approximately 45 GeV, *i.e.*, a centre of mass energy close to the Z resonance, in order to study production and decay of the Z boson. LEP-II began in 1996 with beam energies of around 80 GeV allowing the production of W boson pairs.

A map of the LEP area is shown in figure 4.1. The ring consists of eight bending and eight straight sections. The four experiments, ALEPH, DELPHI, L3 and OPAL are located at the centre of alternate straight sections. The electron and positron beams are split into four or eight bunches which are timed to cross at the interaction points inside the detectors. In 1995 a new technique was introduced: each bunch was replaced by up to four closely-spaced bunchlets. This increases the luminosity considerably. With four bunches in each beam, the bunch crossing rate seen by each experiment is approximately 44 kHz.

Superconducting quadrupoles on either side of each experiment squeeze the beams to give a luminosity of about 10^{31} cm^{-2}s^{-1}. Conventional radio frequency cavities in LEP-I accelerate the beams and compensate for synchrotron radiation losses. For LEP-II they are complemented by additional superconducting cavities. The beams are injected into LEP with an energy of 22 GeV via a complex system of smaller accelerators, as shown in figure 4.2. Once accelerated they can circulate up to about 20 hours giving several thousand Z decays per fill.
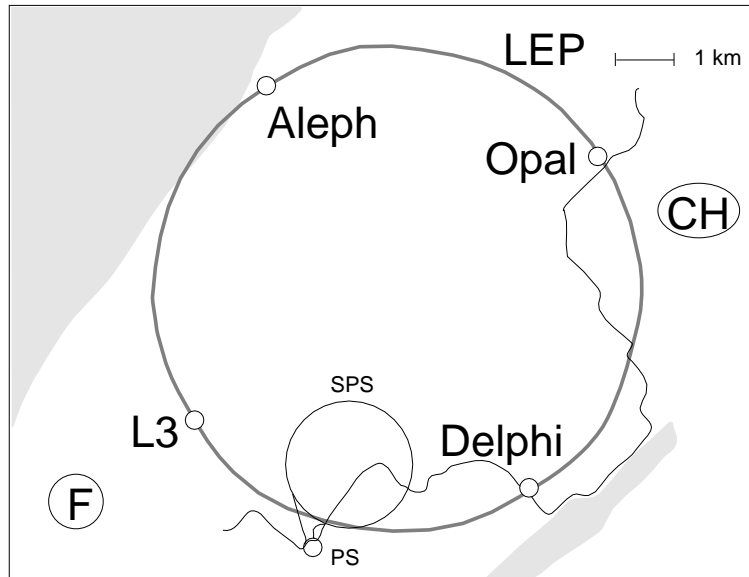
Figure 4.1: A map of the CERN site showing the Large Electron Positron collider (LEP), the Super Proton Synchrotron (SPS), Proton Synchrotron (PS), and the four LEP experiments ALEPH, DELPHI, L3 and OPAL.

To identify bottom hadrons using the length of flight, the dimension of e^+e^- bunches and the environment near the interaction point are of great importance. The average decay length of B hadrons at LEP-I is of the order of 3 mm. The extension of the beam in the plane perpendicular to the beam axis at the interaction point is of about 20 μm in vertical direction and of about 100 μm in horizontal direction. The difference between horizontal and vertical extension is caused by the synchrotron radiation emitted in the accelerator plane causing momentum and thus orbit changes. The total luminosity delivered to the L3 experiment at the Z resonance was 155 pb^{-1}; 80 pb^{-1} were taken in the years 1994 and 1995. Detailed information on the LEP machine and its performance can be found in [65].

4.2   The L3 Detector

L3 is a large detector [66] designed to study e^+e^- collisions at centre-of-mass energies of up to 200 GeV with an emphasis on the precise energy measurement of electrons, photons, muons and jets. Figure 4.3 shows a perspective view of the detector. It is located in a cavern at interaction point 2 of the LEP ring, 50 m
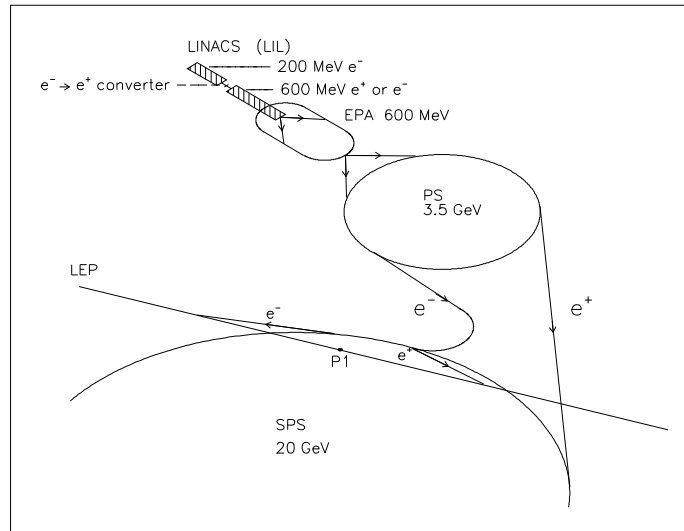
Figure 4.2: A schematic view of the e^+e^- injection system through linac, accumulator (EPA), Proton Synchrotron, Super Proton Synchrotron and into LEP.

under the village of Sergy in the foothills of the Jura mountains in France.

The experiment consists of a number of sub-detectors housed in a 7800 ton solenoid. The magnetic field of the solenoid is 0.5 T along the beam line with a high degree of uniformity. A 32 m long, 4.45 m diameter steel tube running concentric to the LEP beam line houses the *inner detector* elements arranged as *barrel* and *endcap* components around the beam pipe. This support tube can be adjusted to allow the alignment of all sub-detectors relative to the e^+e^- beams.

Starting from the interaction point there is a high resolution Silicon Vertex Detector (SMD), a tracking chamber (TEC) to measure the $r\phi$ coordinates, and a Z chamber to measure the z coordinates of charged particle trajectories, an electromagnetic calorimeter made from Bismuth Germanate (BGO) crystals, a luminosity monitor, an array of scintillators, an uranium hadron calorimeter and a muon filter. Outside the support tube, but within the magnet volume, are three layers of muon chambers arranged concentrically around the beam axis. From 1995 an additional forward-backward muon system consisting of chambers arranged on either side of the solenoid endcaps belongs to the detector.

Additional toroids on both sides allow precise momentum determination with this

new forward-backward muon chamber system.
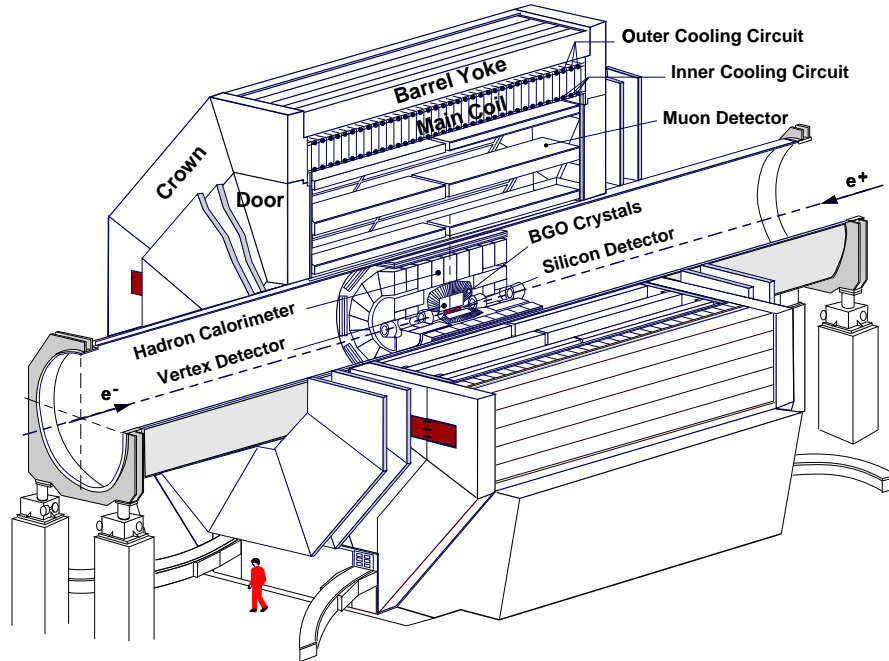
Figure 4.3: Perspective view of the L3 detector.

The design and operation of each sub-detector is outlined below, with focusing on the inner tracker (SMD+TEC) which is the most important part of L3 for the analysis presented in this thesis. A more detailed description of the detector can be found in reference [66, 67].

Coordinate System

In order to combine the information of the detector components, a standard coordinate system has been agreed upon:

- The origin of coordinates is at the nominal e^+e^- interaction point.

- The z axis runs from the origin in the direction of the incoming electron beam.

- The x axis runs from the origin to the centre of the LEP machine.

- The y axis points vertically through the origin.

- The polar angle, θ, is defined as the angle with respect to the z axis.

- The azimuthal angle, ϕ, is defined as the angle in the xy plane with respect to the x axis.

- The xy plane is also denoted as rϕ plane where r is the radial distance from the origin (cylinder coordinates).

Silicon Microvertex Detector

In the last 10 years a lot of effort has been made to establish the silicon technology for the construction of detectors with very high spatial resolution. Today two kinds of segmentation techniques are used: strips to measure one coordinate per segmentation layer and silicon pads to measure two coordinates per segmentation layer simultaneously. Their spatial resolution of the order of 10 μm and the possibility to install the detectors close to the beam pipe make the silicon detectors essential for the recognition of secondary decays on an event-by-event basis. Most of the actual collider experiments make use of this technique: *e.g.*, all LEP experiments, SLD, H1, ZEUS, HERA-B, the BaBar Experiment, CDF, D0, and BELLE.
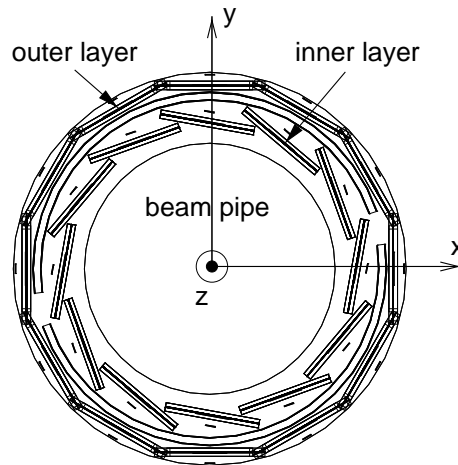
Figure 4.4: The Silicon Microvertex Detector - end view.

The Silicon Microvertex Detector (SMD) of L3 is a cylindrical detector directly surrounding the beam pipe (figure 4.4). It is built of 2 layers of double-sided silicon

strip detectors, at 6 and 8 cm radially from the interaction region, respectively. It is capable of providing rϕ and z coordinate measurements for $|\cos\theta| \leq 0.93$.

The basic detector element is a *ladder* (figure 4.5). There are in total 24 ladders, each built from two separate half-ladders. Each half ladder in turn consists of 2 electrically and mechanically connected silicon sensors. Each sensor is 70 mm long, 40 mm wide and made of 300 μm thick n-type silicon. On one side (the junction side) there are implantation strips every 25 μm with a readout pitch of 50 μm. These run parallel to the long side of the sensor and give the rϕ coordinate. On the other (ohmic) side are n$^+$ implantation strips with a pitch of 50 μm perpendicular to the junction side strips. Between the strips on the ohmic side p$^+$ blocking strips are interspersed designed to separate accumulated surface charge. The readout pitch is 150 μm for $|\cos\theta| \leq 0.53$ and 200 μm for the rest of the angular range. This side measures the z coordinate.
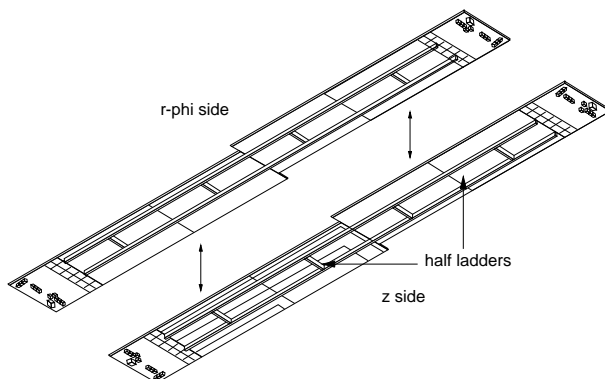
Figure 4.5: Exploded view of a SMD ladder. Each half ladder consists of two double-sided silicon sensors.

The inner ladders are mounted parallel to the beam line with a 5 % overlap as an alignment aid. The outer ladders are mounted at a stereo angle of 2° with respect to the beam line to facilitate pattern recognition, particularly the reconstruction of the z coordinate. More information on the construction and operation of the SMD can be found in [68] and [69, 70].

As mentioned above there is a difference between the strip distance and the readout pitch. It is still rather expensive to read out all strips of these detectors with typical strip pitches of $\approx$ 30 μm. One possibility to reduce the huge number of readout channels by a small worsening of the resolution is the method of capacitive

charge division: strips are coupled by a capacitor and hence charge collected by a non-readout strip induces a certain charge on the neighbour readout strips. The position of the trajectory can consequently be extrapolated by the signal heights including information from non-readout strips.

A detailed report on silicon detectors and their application in heavy flavour physics can be found in [71].

SMD Alignment

In order to achieve the desired high precision in vertex reconstruction an accurate alignment of the SMD has to be performed. Before installation of the SMD detector into the L3 experiment a complete survey of the ladder positions on the carbon cylinder has been performed. Under running conditions the ladder positions are monitored as a function of time. This is done by laser light spots, focused on the silicon detector surface. The system is capable of a precision of several microns.

The final alignment concerns both the global SMD detector position with respect to the rest of the detector and the relative positions of SMD sensors to each other. The global alignment is performed by the use of a sample of dimuon events with muons measured in the time expansion chamber and the muon chambers. The discrepancy between the SMD hits and the track extrapolation points is minimised using free parameters describing translations and rotation angles of the whole detector. In the local alignment each ladder position is described by translations and rotations relative to a SMD coordinate frame. The parameters are determined as before by minimising the residuals of the hit positions with respect to the fitted track. In order to be independent of the systematic error from the rest of the tracking system the local alignment is done with the SMD alone. Tracks that are passing through the rϕ overlap region of the inner ladders constrain neighbour ladders to each other. Tracks that have hits in the inner and outer layer relate both detector layers to each other. In addition dimuon and Bhabha events allow to constrain opposite sides of the detector due to their back-to-back structure. As a result the relative ladder positions can be determined with a resolution of 5 μm in the rϕ projection and of 10 μm in the rz projection.

SMD Efficiency

In order to study the SMD efficiency the number of tracks with an associated SMD hit has been compared to the number of tracks measured by the TEC:

$$\epsilon^{SMD} = \frac{\text{Number of tracks with SMD hit}}{\text{Number of TEC tracks}} \tag{4.1}$$

A dilepton sample was used to determine the efficiency. The low track multiplicity of such events avoids problems with ambiguous hit assignments. Hit finding and matching algorithm effects are included in the tracks numbers and lead to correlations between the physical independent SMD layers. The efficiencies of all four SMD layers as a function of the angles θ and ϕ are shown in figures 4.6 and 4.7. As can be seen the efficiency is angular dependent. The Monte Carlo describes these dependencies, because broken or inefficient readout channels are taken into account in the simulation. The observed deviations are of the order of 2%. The requirement that each track has at least one assigned SMD z-hit reduces the number of events to 74% of the total data sample.

The overall efficiency is 84% and the hardware was found to be operational to 79% [68, 72]. The spatial resolution in rϕ is 15μm and 25μm in z.

Time Expansion Chamber

The time expansion chamber (TEC) [73] is a precise wire chamber for position measurements of charged particles traversing its volume. The chamber extends over a radial distance of 37 cm and operates in the so-called *time expansion mode*. Following this principle, the chamber combines a large volume with a low, homogeneous drift field with a very small volume of high field to achieve the necessary gas amplification. The chamber is filled with a mixture of 80% CO_2 and 20% isobutane (iso-C_4H_{10}), at a pressure of 1.2 bar. This gas mixture has a low diffusion coefficient and enables the use of low electric fields (0.9 kV/cm). Thus the electrons produced by ionisation have a low drift velocity of 6 μm/ns which allows high position resolution. Within the region of a linear drift-distance-to-time relation - which not includes the amplification region and the zone around the cathode wires - an average single-wire resolution of about 50 μm is obtained. The averaged double-track resolution is 650 μm.
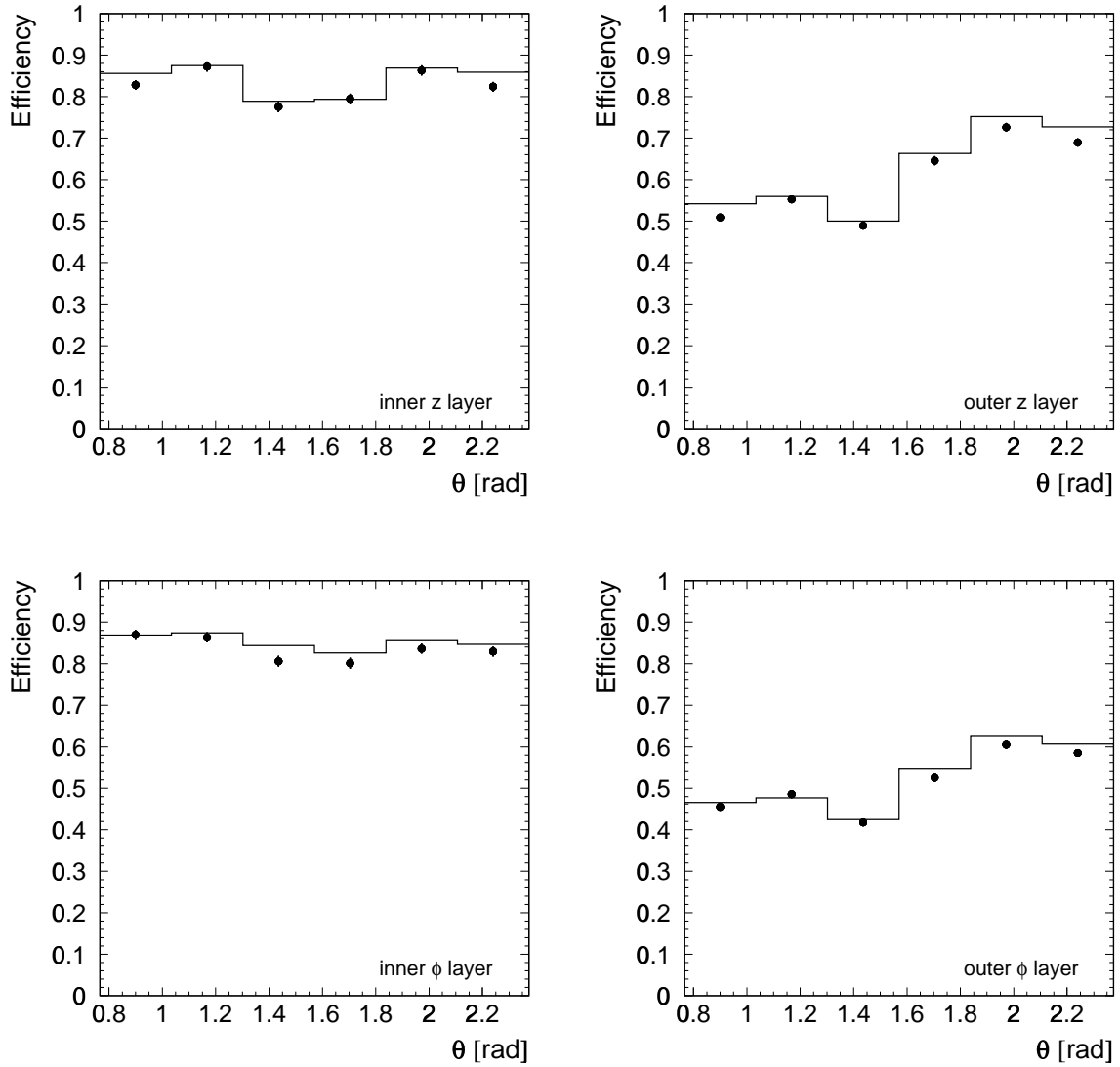
Figure 4.6: The SMD efficiency as a function of θ. The dots correspond to data and the histograms to the Monte Carlo.
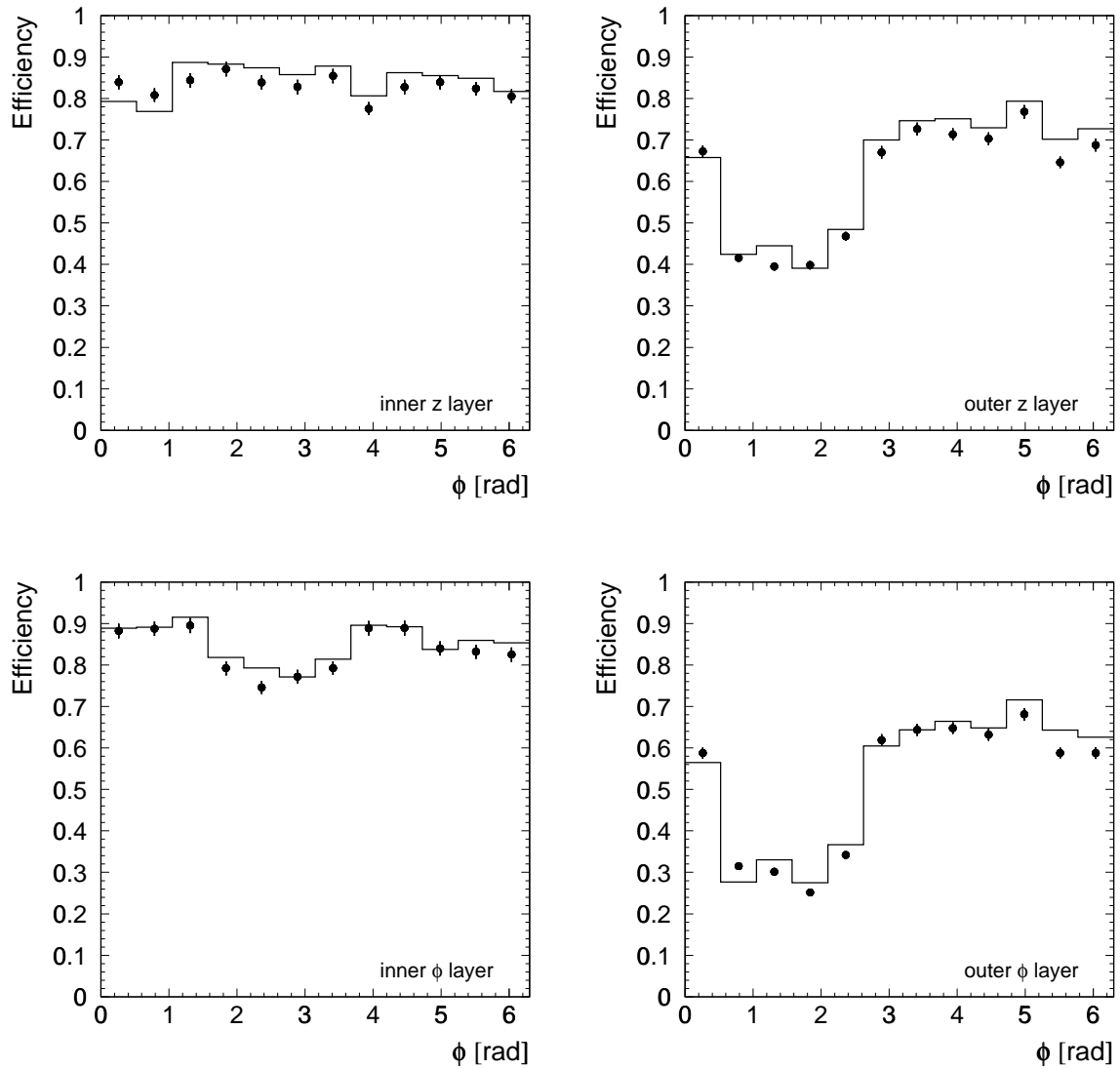
Figure 4.7: The SMD efficiency as a function of ϕ. The dots correspond to data and the histograms to the Monte Carlo. The reduced efficiency of the outer ϕ layer in some particular bins is due to two disconnected silicon wafers. Due to the matching algorithm a similar efficiency gap can be found for the outer z layer, although this layer is fully operational.

The chamber is made up of two concentric cylinders operating in a common gas volume which is limited by an inner cylinder at a radius of 9 cm and by an outer cylinder at a radius of 46 cm. Its sensitive length in z direction is 98 cm. The inner drift chamber is divided into 12, the outer into 24 sectors along the ϕ angle. The different number of sectors is given by the limitation of the geometry of each sector to keep the maximum drift distance in the inner and outer sectors almost equal. The drift time in one sector is required to be smaller than the time between two bunch crossings. In the 8x8 bunch-train regime in 1995 the time between two bunches was about 11 μs. The maximum drift time of the TEC is about 9 μs.
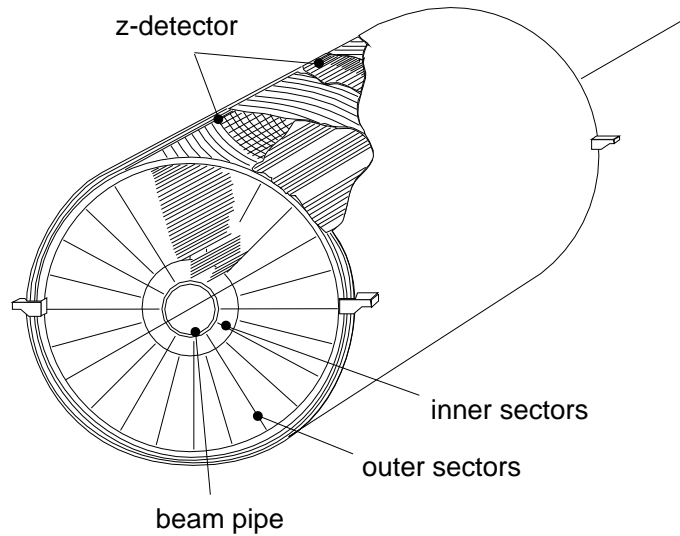
Figure 4.8: The Time Expansion Chamber. Note the two concentric cylinders around the beam pipe and the division into 24 outer and 12 inner sectors.

The arrangement of the sectors of the inner chamber with respect to the sectors of the outer chamber enables to resolve left-right ambiguities. These ambiguities occur because only the absolute value of the drift distance - not its direction - is determined. Each sector contains anode, cathode and grid wires stretched parallel to the beam direction, as it can be seen in figure 4.9. The grid wires situated close to the anodes separate the drift region from the amplification region. The inner chamber measures up to 8, the outer up to 54 coordinate points of a track.

All wires measure the ϕ coordinate. In addition some of the anode wires are prepared for z coordinate measurement. Information on the z coordinate can be obtained by a division of the signal charge which is transported to both ends of
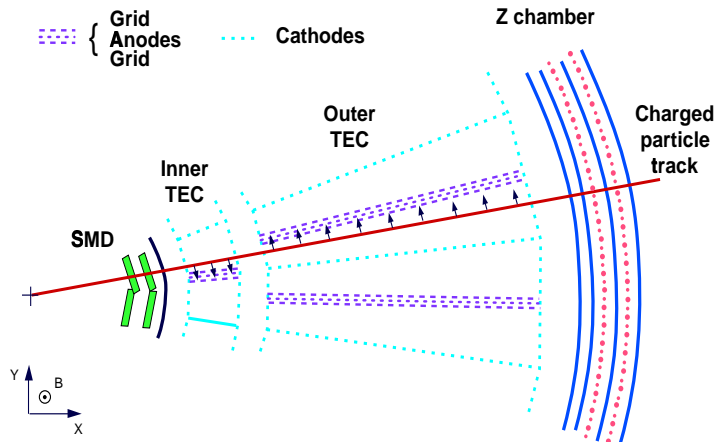
Figure 4.9: A view of the tracking system in rϕ. Beginning from the interaction point, two layers of the silicon detector, the inner and outer sectors of the TEC and the two layers of the Z chamber are seen.

the wire and a comparison of its pulse heights. The drift direction can be determined by the readout of groups of grid wires on both sides of the anode. The difference of the induced charges read out on both sides of an anode helps to solve the left-right ambiguity. In order to get spatial information from a drift chamber, the drift-distance-to-time relation has to be known. The determination of the drift-distance-to-time relation for all anodes of the TEC is an essential part of the calibration. The first step is to convert the raw time information coming from the flash analog digital converter (FADC) into the drift time. This is done by subtracting from the raw time an anode depending time marker, which results from the delay of the beam crossing signal to the induction onto an anode. The next step is the determination of the calibration constants, *e.g.*, the drift-distance-to-time relation. This is done by using pairs of muon tracks produced in e$^+$e$^-$ collisions. The curvature of the tracks predicted by the muon chamber is used as an external constraint. The determination of the global parameters is done by minimising the average residuals of the hits in the inner chamber with respect to the track predicted by the outer one. Using these global parameters, the anode dependent correction parameters for each anode are determined by an iterative

fitting procedure.

A new possibility to calibrate the TEC is offered by the SMD detector [74]. This calibration has the advantage that it is independent of some TEC systematic uncertainties. In dimuon events a precise track fit can be performed with the muon chambers and the SMD. The TEC is now calibrated by comparing this track trajectory with the time measured in the TEC. The particular advantage is that the residual minimisation is non-iterative and yields directly the calibration parameters. As a result the parameterisation can be chosen closer to the realistic situation by enlarging the number of free parameters. For instance, small corrections to the linear drift-distance-to-time relation in the drift region can be described by the inclusion of a quadratic term. Most important, the drift-distance-to-time relation are determined separately for each wire, so that the calibration becomes wire and drift region dependent. Having 2784 wires, about 18000 parameters were fitted with the SMD calibration method. The single-wire resolution could be improved by 20% in the drift region and by a factor two in the low-resolution regions close to the cathode and amplification regions. The only drawback is that the TEC and SMD calibrations become dependent from each other because the resolution is only as precise as the position of the SMD is known with respect to the TEC. A data sample, not used in the SMD calibration, has been used to cross check the impact of SMD systematic uncertainties on the TEC calibration. This uncertainty was found to be small.

The use of an external detector, namely the SMD, allows to remove systematic uncertainties in the TEC calibration so that an intrinsic resolution of the TEC of better than 50 μm could be reached [75]. The transverse momentum resolution obtained with the combination of SMD and TEC measurements is $\delta(1/p_{\perp}) = 0.017$ GeV^{-1} [75]. The inclusion of the SMD improves the resolution by a factor of two mainly due to the very precise measured track points and its impact on the lever arm of the tracking system. In addition the precise measured SMD track point close to the interaction point has a considerable effect on the impact parameter resolution. A track fit with the TEC alone yields a resolution of 120 μm for high-momentum tracks which is improved to 32 μm by including the track points measured by the SMD.

Z Chamber

The Z chamber [76,77] supplements the measurements from TEC and SMD with a z coordinate measurement in the angular range of $42° \leq \theta \leq 138°$ at r=50 cm. It consists of two cylindrical proportional wire chambers with cathode strip readout. Each wire chamber contains two cathode layers. The 240 readout strips of one cathode layer in each chamber are oriented perpendicular to the chamber axis whereas the strips of the remaining layers form a helix with an angle of $\pm$ 69° to the axis (stereo layer). The 576 anode wires per chamber are strung in the axial direction. A particle traversing the Z chamber generates an avalanche of electrons close to the wire. The avalanche induces image charges on both cathode layers. The measurement of the charge distribution allows to localise the avalanche position along the wire. The ϕ-component of the stereo layer measurement is used to match the z information with the tracks measured in TEC. The single hit efficiency of each chamber is approximately 96%. The resolution varies between 200 μm and 1 mm from the centre to the edges of the chamber. For an analysis which is based on high multiplicity events, the capability to separate two tracks up to a certain distance is very important. This distance is called double-track resolution. The double-track resolution of the Z chamber is measured to be about seven millimeter and is the limitation factor for a high 3-dimensional impact parameter resolution.

Electromagnetic Calorimeter

The electromagnetic calorimeter, shown in figure 4.10, was designed to measure the energies and positions of photons and electrons with high precision. The calorimeter surrounds the central tracking system and consists of 10734 Bismuth Germanate (BGO) crystals. The central part of the detector is made of two half barrels covering a polar angle range of $42° \leq \theta \leq 138°$ and contains 7680 crystals in total. This angle region is called *barrel region*. The polar angle coverage of the two endcaps each consisting of 1527 crystals is $11.6° \leq \theta \leq 38°$ in the forward and $142° \leq \theta \leq 168.4°$ in the backward direction. The inner radius at the origin of the coordinate system is 52 cm.

Each BGO crystal has the shape of a pyramid segment with a front face of 2×2 cm^2 and a rear face of 3×3 cm^2. Their length of about 24 cm corresponds to approximately 22 radiation lengths and one nuclear interaction length. The BGO
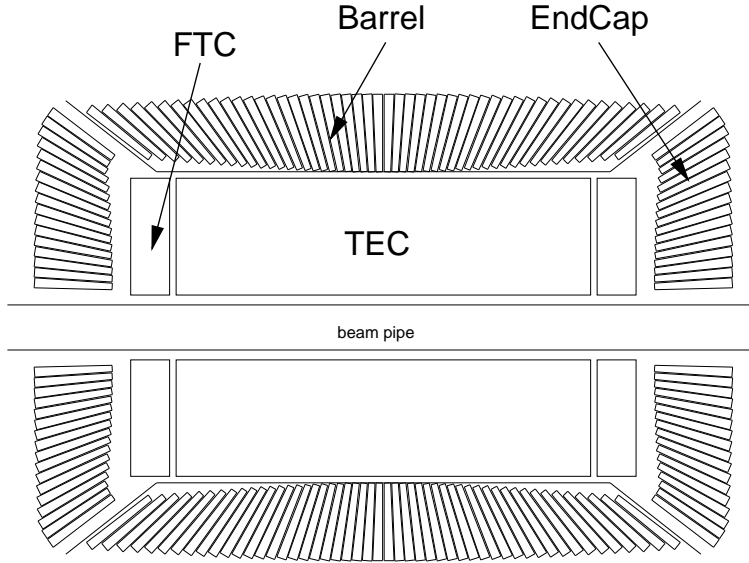
Figure 4.10: The BGO electromagnetic calorimeter.

scintillation light is collected using 2 photodiodes glued on the rear face of each crystal. An angular offset of the order of 10 mrad of the crystals in ϕ with respect to the nominal interaction point reduces the amount of particles traversing the space between crystals. The crystals act both as showering and detection medium. The principle of forming clusters in the BGO is depicted in figure 4.12. The BGO crystals have a high stopping power for electrons, positrons and photons. Due to the small Moliere radius of BGO (2.2cm) the energy of electromagnetic showers is concentrated in almost one crystal. The scintillation light is read out by photodiodes mounted on the crystal backface. Hadronic particle can be separated by the lateral expanded showershape.

Three independent calibration methods ensure a continuous calibration and monitoring of the calorimeter. A Xenon flasher monitoring system measures the transparency of the crystals by comparing the detector response with a generated reference light pulse. In addition Bhabha scattering is used to calibrate the BGO to the precisely known beam energy. For the calibration at low energies data of minimum ionising cosmic muons are used.

The energy resolution is measured to be 5% at 100 MeV and less than 2% for energies larger than 1 GeV [67].

Scintillation Counters

An array of 30 scintillation counters is situated in the region between the BGO and the hadron calorimeter. A polar angle coverage corresponding to $|\cos\theta| < 0.83$ and an azimuthal coverage of 93% is achieved. The aim of these scintillators is to trigger hadronic events using the hit multiplicity and to discriminate cosmic muons by precise time-of-flight measurements.
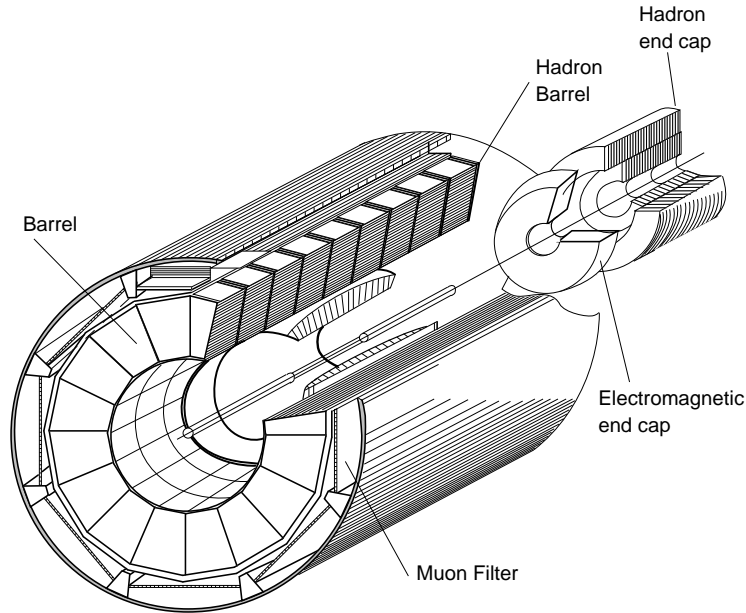
Figure 4.11: Schematic of the hadron calorimeter covered by muon filters.

Hadron Calorimeter

The energy of hadrons and hadron jets emerging from e^+e^- collisions is determined by the total absorption technique with the electromagnetic and the hadron calorimeter. The hadron calorimeter (HCAL) is mechanically divided into three parts, the barrel covering the central region of $35° \leq \theta \leq 145°$, and the endcaps covering the polar angle range of $5.5° \leq \theta \leq 35°$ and $145° \leq \theta \leq 174.5°$, respectively. The calorimeter is made of depleted uranium absorber plates interspersed with proportional wire chambers. The amount of material traversed by a particle depends on the polar angle and varies between 6 and 7 nuclear absorption lengths.

The barrel has a modular structure consisting of 9 rings of 16 modules each as shown in figure 4.11. For the readout the wires are grouped in so-called towers which include only wires from alternate and thus parallel planes. The principle of forming towers in the hadron calorimeter is depicted in figure 4.12. The energy resolution of the HCAL for single pions was determined to be $(55/\sqrt{E} + 8)\%$. The fine segmentation of the calorimeters allows a measurement of the jet axis with a precision of approximately 2.5°. In addition a muon filter is mounted on the inside wall of the support tube and adds one more absorption length to the HCAL. This combination ensures that almost only minimum ionising particles reach the muon spectrometer.
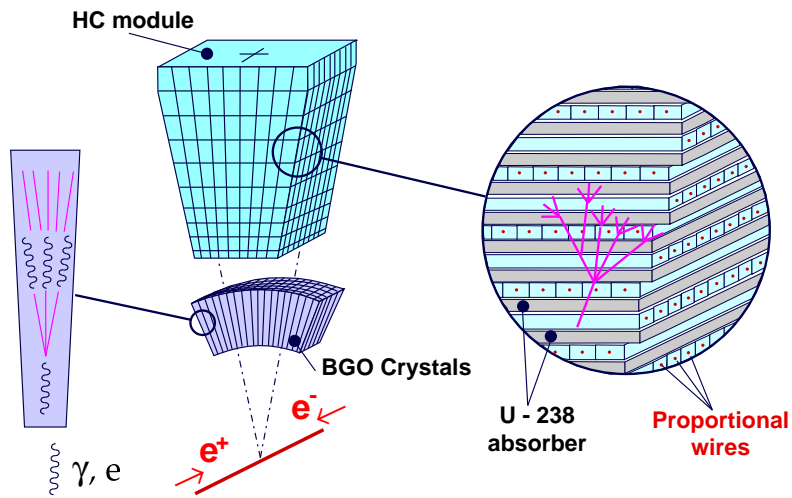
Figure 4.12: Principle of function of BGO and hadron calorimeter.

Luminosity Monitor

The luminosity delivered by the LEP collider to the L3 interaction region is measured by two dedicated BGO calorimeters. In the limit of small polar angles the cross section for Bhabha scattering $e^+e^- \to e^+e^-$ approaches the contribution from pure photon exchange. The cross section is very well known from QED so that the number of observed events can be converted into a direct determination of the luminosity. The calorimeters are situated symmetrically on either side

of the interaction region at z = ±2.7 m. They cover a polar angular range of 25 mrad < θ and $(\pi - \theta)$ < 70 mrad. The limiting factor on the luminosity measurement is the definition of the fiducial volume. In order to improve the angular resolution a Silicon Luminosity monitor (SLUM) was installed in front of each calorimeter [78]. The precision obtained with this luminosity monitor system is $\Delta \mathcal{L}/\mathcal{L} \approx 0.2\%$. The uncertainty of the theoretical prediction of the Bhabha-scattering cross section leads to a contribution of 0.16% to the luminosity error.

Muon Spectrometer

The muon spectrometer consists of eight ferric octants with three layers of drift chambers. It extends from an inner radius of 2.23 m up to an outer radius of 5.93 m from the beam line. One octant contains five precision drift chambers (P-chambers) arranged in the three layers. There are two chambers in the outer layer each with 16 signal wires, two chambers in the middle layer each with 24 signal wires, and one inner chamber containing 16 wires. A set of Z-chambers is mounted on the top and the bottom of the P-chambers of the inner and outer layer. The P and Z-chambers together yield a measurement of the momentum of the track with a precision of $\sigma(\mathrm{E_{beam}}/\mathrm{p_{\mu}}) = 2.5\%$ for 45 GeV muon tracks. Tracks measured in only two layers have a momentum precision of $\sim 20\%$. In 1996 the muon system has been completed by forward muon chambers. The polar angle acceptance of the whole muon system covers the range from 36º < θ < 158º.

L3 Trigger System

In general, the output of the detector is a large number of digital and analog signals for every beam crossing. Usually, not all information can be recorded by an experiment. In order to maximise the number of events written on tape and minimise the background an efficient trigger is needed to read out the L3 subdetectors only when a real e^+e^- annihilation take place in the detector. The readout sequence starts at each bunch crossing and, unless it is aborted, takes $500\mu s$ or 45 bunch crossings to complete. While the readout sequence is active no new input will be accepted. In order to minimise this 'dead time' a trigger system is designed in three stages such that beam crossings without e^+e^- annihilations can be recognised at time scales of $9\mu s$. This allows in case of a negative decision

to reset the readout in time for the next bunch crossing. Under normal running conditions the dead time is less than 8%.

Level-1 performs a logical OR of triggers from individual subdetectors. Level-2 coordinates information from more than one subdetector, while level-3 makes the final decision including the full detector information.

Level-1 trigger   The level-1 trigger is based on five separate triggers. Each trigger starts its operation at the beam crossing. If any of them has a positive decision the event is digitised and stored until the level-2 decision is available. The typical trigger rate of the level-1 trigger is 8 Hz. The five subdetector triggers are:

- **TEC trigger**: The TEC trigger decision is based on the total number of tracks, the number of co-planar pairs of tracks or on more complicated topologies [73].

- **energy trigger**: The energy trigger is designed to select events with a minimum energy deposition in the electromagnetic or hadronic calorimeter [79].

- **scintillator trigger**: The signals of scintillation counters are used to select high multiplicity events and to discriminate cosmics using the time-of-flight information [80, 81].

- **luminosity trigger**: The luminosity trigger requires energy in the luminosity monitor and selects low angle Bhabha events.

- **muon trigger**: The muon trigger detects events with at least one reconstructed track in the muon spectrometer. It is not used in this analysis.

Level-2 trigger   The level-2 trigger decision is based on the level-1 trigger information. The coarse signals of the different subdetectors are combined and analysed. The main task is the rejection of background events, such as calorimetric noise, beam-gas events, beam-wall interactions and synchrotron radiation. Each event with more than one positive level-1 trigger is automatically passed to the level-3 trigger. The level-2 trigger rate is typically 6 Hz.

Level-3 trigger   The level-3 trigger decision is based on the full detector information for the event. The digitised data are used to define thresholds more precisely to perform a simplified pattern recognition for tracks, to reconstruct energetic clusters, and to match energetic bumps in the calorimeters with tracks determined by the TEC. This leads to a further background suppression. Events with more than one positive level-1 trigger result are always accepted as well as all luminosity triggers. The level-3 trigger does not introduce any additional dead time and enables the reduction of the event writing rate to 2-3 Hz.

Chapter 5

Simulation and Reconstruction

Each physical measurement is based on the observation of a physical process with a measuring device. In order to extract valuable information from this observation the functionality of the measuring device has to be known exactly. The response of the L3 detector on a certain process is simulated by computer programs in such a way that the reconstruction of the event can be applied as well as for 'real' data. The comparison of the detector response from the simulation with that what the nature is 'producing' provides a good test of the knowledge of underlying physics. The analysis chain for high-energy physics experiments contains in general the following three components:

- data taking / Monte Carlo simulation

- event reconstruction

- physics analysis

These steps within the overall framework of any high energy physics experiment are illustrated in Figure 5.1.

5.1   Monte Carlo Simulation

Monte Carlo simulations in particle physics experiments are usually split into two subsequent steps:

- event generation

- detector simulation

Each generated event of a certain process contains the type of particles in the final state, the history of their respective parent particles and all four-vectors. Subsequent detector simulation modules simulate the response of specific measurement devices to all particles traversing it. The result is a number of digitised information as provided by the detector modules during real data taking.
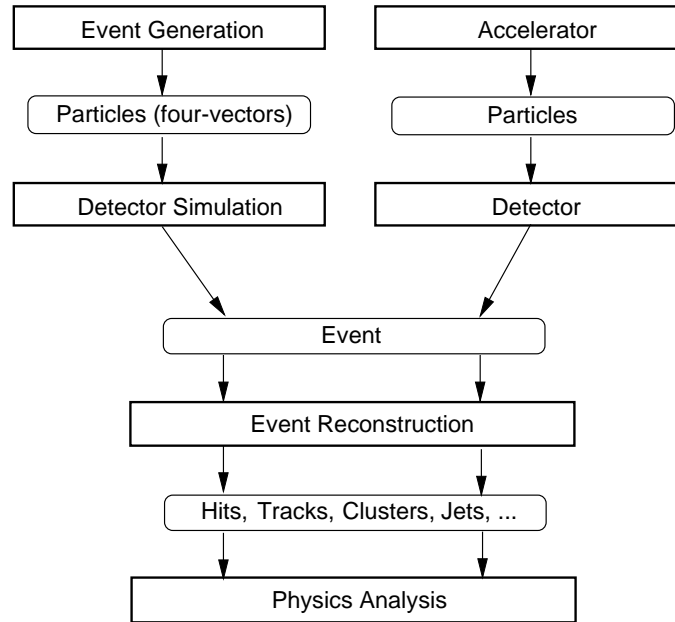
Figure 5.1: Schematic representation of the steps in the simulation, real data taking and subsequent reconstruction.

5.1.1 Event Generation

The L3 event-generator library contains generator modules for both Standard Model physics and new physics beyond the Standard Model. For the analysis presented here, event generation was performed by the programs JETSET [44, 82] and HERWIG [83, 84] that generate $e^+e^- \to f\bar{f}$ events according to Standard Model processes and perform subsequent decays using experimental data on lifetimes and

branching ratios as input.

As explained in section 3.1, the generation of events with hadronic final states can be subdivided into four different steps: beginning with the pair production of the quarks up to the formation of stable particles, which will be detected by the experimental apparatus.

5.1.2 Detector Simulation

The generated particles are propagated through a program package being a detailed representation of the detector including the response of each active detector element and the effects of showering in the detector materials. In L3, this is performed by a combined version of GEANT3 and GEISHA [85]. The output is a number of digitised information which can be reconstructed using exactly the same procedure as for the real data. The calorimeter responses are tuned with the help of test beam data. Detector imperfections (dead cells, noisy channels etc.) vary with the time and must be properly simulated. In order to provide such information they are stored in a central database. Each subdetector is represented in the database by following information:

- General setup such as the detector geometry.

- Data from online monitoring programs, *e.g.*, high voltage status of the TEC, BGO crystal temperature etc.

- Offline information of the different subdetectors, *e.g.*, calibration constants, dead crystal or dead wire maps and alignment data.

In order to keep the statistical uncertainty of the simulation small, the number of simulated events should be much larger than the number of events in the real data sample. However, event simulation is very time consuming: on average one minute CPU time (HP-UX9000/735 with PA7200 processor) for a hadronic events and up to a few minutes for events with a complicated shower structure in the BGO. Consequently, a limited number of events can be generated depending on the event type and the corresponding time need. For hadronic events, typically 4-5 times the number of real data is produced. For the analysis presented here, the Monte Carlo sample contains about 4.7 million fully simulated $e^+e^- \to q\bar{q}$ events.

This corresponds to 4.8 times of the statistics of the experimental data.

In order to be able to produce as many Monte Carlo events as possible and to handle large Monte Carlo requests in a proper time, L3 has implemented a system for distributed and asynchronous parallel processing of Monte Carlo events in a heterogeneous computing environment, FUL3 [86]. The concept of FUL3 is based on the idea to use a scalable amount of processors for the Monte Carlo simulation. The client-server architecture of FUL3 allows to involve computer instantaneously when the system load permits, and vice versa. The master is running on an SGI IRIX64 machine. Up to now about 100 slave machines of the L3 offline UNIX cluster are involved in the FUL3 Monte Carlo production. Most of the workstations are of type HP 9000 series 700, some machines are of type SGI Indy and since a few month an increasing number of Linux PC's are included.

5.2 Event Reconstruction within L3

The event reconstruction takes place first within each sub-detector. The individual raw data are formed into objects like tracks or clusters. In order to characterise the event as a whole the objects finally are combined. Since this analysis is based on the lifetime information of an event, especially the tracking within L3 will be explained in detail below.

Muon Spectrometer

Hits in the three layers of the muon chambers are combined to form tracks. These tracks are fitted with a helix curve to get information about the momentum and the sign of the charge. The mean energy loss of a minimum ionising particle (MIP) coming from the traversal of material in the inner part of the detector is taken into account in order to determine the muon momentum at the interaction point.

Hadron Calorimeter

Hadrons showering in the hadron calorimeter generate many charged particles, which ionise the gas in the multi-wire proportional chamber. The local sum of the charge measured in the wire chamber weighted with the average energy loss in the
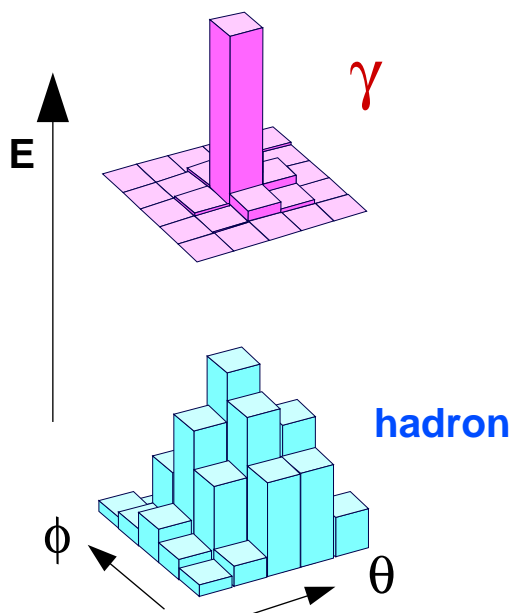
Figure 5.2: The different shower shapes in the BGO calorimeter caused by a photon (or electron) and a hadronic particle.

absorber plates is a measure of the deposited energy. A MIP deposits a certain amount of energy in the HCAL. A high energy muon looses about 2-3 GeV.

Electromagnetic Calorimeter

Signals of adjacent crystals are grouped into energy bumps. The position of a bump is determined by a centre of gravity method. By obtaining the shape of energy deposition it is possible to identify particles. This is mainly used to distinguish between electromagnetic showers and the signals produced by hadrons. Narrow, symmetric showers are caused by electrons and photons, whereas lateral expanded shower shapes may result from hadrons (see figure 5.2).

A parameter to distinguish between those kinds of particles is the ratio of the energy sums of crystals within a 3×3 crystal map and crystals within a group of 5×5 crystals around the centre of gravity of the tower. According to the number of crystals in each tower the parameter is called E_9/E_{25}. For electrons and photons this

value is typically $E_9/E_{25} \geq 0.94$. The average value for hadrons is much smaller. This enables a effective distinction between hadrons and electrons (photons).

The reconstructed bumps in the electromagnetic calorimeter are associated with information from the hadron calorimeter. A calorimetric cluster is built by using the energy deposition of associated bumps of BGO and HCAL. Due to noise in the BGO the energy of a cluster has to be greater than 40 MeV. The energy loss of a high energy muon in the BGO is about 0.25 GeV.

Track and Vertex Reconstruction

The reconstruction of tracks is performed in two steps: The information of the TEC alone is used to predefine a track in the $r\phi$ plane. TEC hits are given by $r\phi$ points, which are computed from the position of the anode wires and the drift time. Afterwards a new - 3 dimensional - fit is performed by assigning hits from the SMD and the Z chamber.
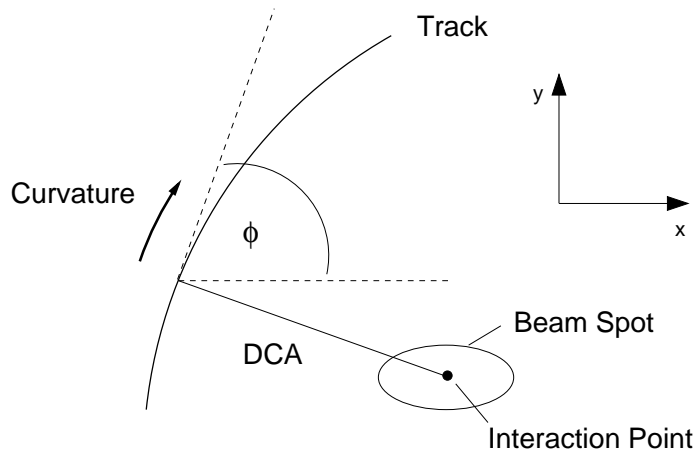
Figure 5.3: Tracking parameters in the $r\phi$ plane.

The hits associated with a track are fitted by a helix. The following parameters (figure 5.3) can be extracted ($r\phi$-plane):

- the curvature C^1 of the track, which is proportional to $1/p_\perp$, with $p_\perp$ the transverse momentum of the track,

---

[1]The curvature is equal to $1/R$, where R is the the radius of the circumference corresponding

- the distance of closest approach (DCA) of the track to the interaction point (reference point),

- the azimuthal angle ϕ within the bending plane.

The interaction point of the e^+e^- annihilation is different for each event but lies within a luminous region, called beam spot. The dimensions of the beam spot are:

$$\sigma_x \approx 120 \ \mu m, \qquad \sigma_y \approx 20 \ \mu m, \qquad \sigma_z \approx 10 \ mm \qquad (5.1)$$

The centre of the beam spot is used as reference point. The central beam spot position is determined by fitting a common vertex for a sample of events. Since the beam spot position is varying with the time it is useful to determine the beam spot positions in short time intervals. Samples of about 200 hadronic events are taken, corresponding to a time interval of about 16 minutes. The result of this procedure, called 200-event-vertex, is the starting point for the reconstruction of the primary vertex in each event. Its error, which corresponds to the r.m.s width, is taken as weight in the fit. For the reconstruction of primary vertices, tracks are selected passing loose cuts on the track quality:

- the track fit should be performed with at least 20 hits of the TEC and at least one hit from the inner layer of the SMD,

- the DCA to the 200-event-vertex should be less than 1 mm,

- the significance of the DCA, defined by the ratio of the DCA and its error, should be less than five,

- the transverse momentum of the track should be greater than 150 MeV.

For the determination of the event vertex an iterative procedure is applied. At each step of the iteration the vertex is calculated with all tracks following the hypothesis that they all have their origin at a single point. If the χ^2 probability of the vertex is less than 5%, the track with the largest contribution to χ^2 is removed and the vertex is recalculated with the remaining tracks. This procedure is repeated until

---

to the particle trajectory. It is positive (negative) defined for (anti-)clockwise 'rotation' in the rϕ plane.

the probability of the vertex is at least 5% or only three tracks are left. In every step the 200-event vertex is used as a constraint. After the primary vertex of an event is determined one is able to calculate the distance of closest approach (DCA) of each track related to this vertex. The DCA and its error, σ_{DCA}, are the most important parameters for the analysis presented here.

Detector dependent correction on the DCA

The uncertainty on the measurement of the DCA has the following contributions:

- intrinsic accuracy of the tracking system

- detector effects left after the basic calibration

- multiple scattering of charged particles in the Coulomb field of nuclei

Since accurate track parameters and errors and their proper description by the Monte Carlo are crucial to this analysis, detailed studies were carried out.

Intrinsic DCA Resolution

The DCA resolution was measured using the miss distance[2] distribution of the two tracks of Bhabha events with respect to the interaction point weighted by $1/\sqrt{2}$. In order to perform an independent check a sample was used which was not taken for the TEC calibration itself.
The measured values depend on the data taking period. For the longest of these periods the DCA resolution of the TEC was measured to be [74]:

$$\sigma_{DCA}^{TEC} = 105 \ \mu m \tag{5.2}$$

Including the information of the SMD in the track fit the DCA resolution can be improved to:

---

[2]The miss distance is defined as the distance between the two tracks with respect to the primary vertex.

$$\sigma_{DCA}^{SMD} = 32 \ \mu m \qquad\qquad (5.3)$$

Detector Calibration Correction

The DCA resolution has been studied as a function of the azimuth angle in local and global angle segment using hadronic events. The aim is to check the quality of the basic calibration at the DCA level. In order to investigate the effect of the tracking system in global the full range of the azimuth angle $\phi_{\mathrm{glo}} \in [0^o, 360^o)$ was divided into 48 segments. The DCA resolution of all tracks belonging to this angle segment was fitted by a Gaussian.
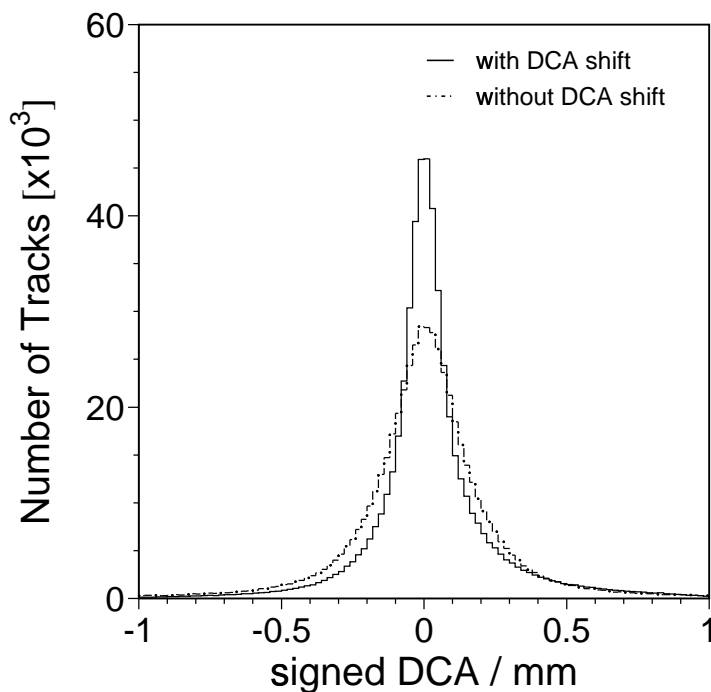
Figure 5.4: Distribution of the signed DCA before (dashed line) and after applying the detector dependent DCA correction (solid line).

The mean of the Gaussian should be compatible with zero. If the mean value differs from zero more than three times the r.m.s the shift is used to correct all tracks passing this segment. Once the global correction is applied the test of the local regions in ϕ can be done. The structure of the TEC as described in section 4.2 allows to define a certain number of sectors with an identical geometrical structure. A ϕ range of 30 degrees include one inner and two outer sectors each. Hence the local azimuth angle is defined as $\phi_{\mathrm{loc}} \in [0^{\circ}, 30^{\circ})$. The resulting ϕ segment is again subdivided into 48 subsegments and the same procedure as before is applied. Finally it will be checked that no significant shifts are left. Otherwise a second iteration is applied.

The corrections have been made for different data taking periods and different SMD two-dimensional[3] hit pattern categories:

Category 1:   no SMD hit

Category 2:   no inner and 1 outer SMD hit

Category 3:   1 inner and no outer SMD hit

Category 4:   1 inner and 1 outer SMD hit

Category 5:   2 inner and no outer SMD hit

Category 6:   2 inner and 1 outer SMD hit

Figure 5.4 shows the DCA distribution before and after applying these corrections.

Multiple Scattering

A charged particle traversing a medium is deflected by many small-angle scatterings caused by the Coulomb force in the field of the nuclei, and hence the effect is called multiple Coulomb scattering. However, in case of hadronic particles the strong interaction also contributes to the multiple scattering, but in comparison to the Coulomb scattering it is negligible [27].

---

[3]Since the SMD layer are double-sided, there are more combinations of of hits than given in these categories, which are choosed to be equivalent to the two-dimensional case (rϕ). Due to the SMD pattern recognition the outer layer also include z information.

The deflection of charged relativistic particle carrying unit charge traversing a homogeneous medium can be described by a Gaussian distribution with a width give by [27]:

$$\sigma_{\mathrm{MS}} = \frac{13.6 \text{ MeV}}{\mathrm{p}} \sqrt{\frac{\mathrm{x}}{\mathrm{X}_0}}. \qquad (5.4)$$

x/X_0 is the thickness of the medium in units of the radiation length and p the momentum of the particle.

Assuming a dependence on the layer thickness from the track angle with respect to the z axis ($\propto 1/\sqrt{\sin\theta}$) one can parameterise the uncertainty from multiple scattering by:

$$\sigma_{MS} = \frac{k}{p_\perp [GeV]\sqrt{\sin\theta}} \qquad (5.5)$$

The error from multiple scattering can be directly obtained by studying the transverse momentum dependence of the width of the DCA distribution. Studies of low momentum tracks were performed for different SMD hit pattern categories. The parameters for the longest data taking period in 1994 are tabled here:

SMD hit category	k
1	212 μm
2	140 μm
3	118 μm
4	110 μm

Reconstruction of the event hemispheres

In order to subdivide the event into two halves according to the back-to-back topology a common event axis has to be reconstructed. This event axis is estimated by the *thrust axis*, $\vec{n}$, which is defined by maximising the quantity T (thrust):

$$T = \max_{\vec{n}} \left(\frac{\sum_i |\vec{p}_i \cdot \vec{n}|}{\sum_i |\vec{p}_i|} \right) \qquad (5.6)$$
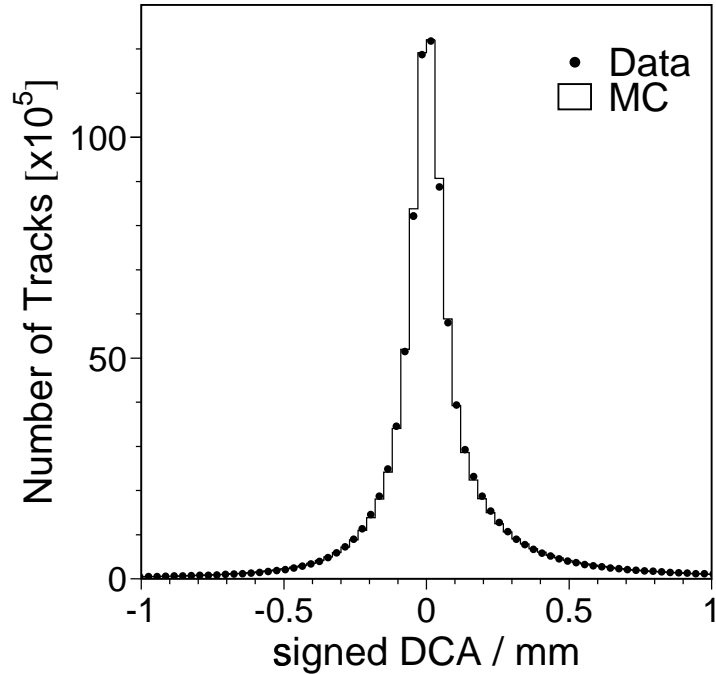
Figure 5.5: Distribution of the signed DCA. The procedure to define the sign is explained in the next section. A negative sign corresponds to an unphysical topology due to the resolution of the detector.

where p_i is the momentum of the track i. The value T itself is very useful to characterise the event. A fully isotropic event has a T equal 0.5, T is equal 1 for a fully collinear event. Figure 5.7 shows the distribution of the thrust value for $b\bar{b}$ events. Data and Monte Carlo are in good agreement, but a slight shift to higher thrust values in the model is visible.

A plane perpendicular to the thrust axis at the reference point subdivides the event into two halves, called *hemispheres*. So, each track of an event can be assigned to one of the two hemispheres.

Reconstruction of Hadronic Jets

Because of the big B hadron mass the decay products have a high transverse momentum with respect to the initial B hadron direction. In order to characterise tracks as belonging to the initial B hadron a cluster algorithm is applied. The most
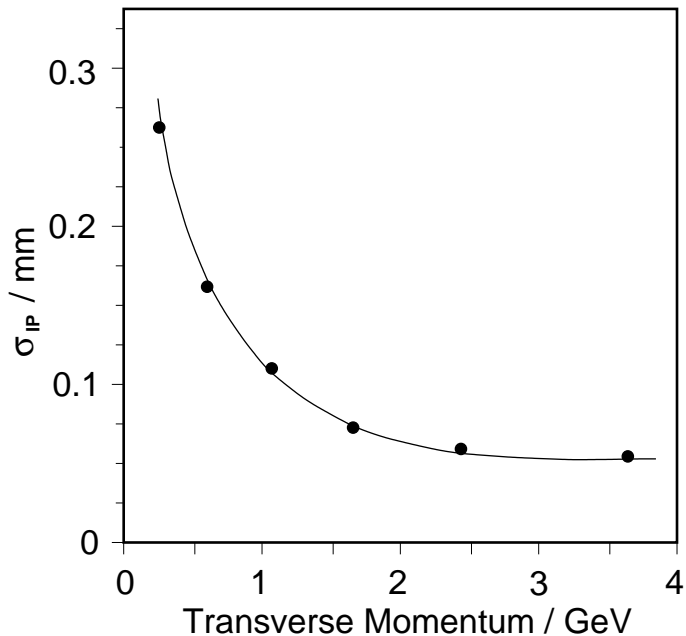
Figure 5.6: The transverse momentum dependence of the impact parameter resolution for the SMD hit category 4. The fitted line corresponds to a parameter k = 110 ± 2.

common cluster algorithm used by the LEP experiments is JADE [87].
JADE calculates for all particles the value:

$$y_{k,l} = \frac{2E_k E_l (1 - \cos\theta_{k,l})}{E_{vis}^2} \tag{5.7}$$

E_{vis}^2 is the total visible energy of the event. The two particles with the smallest value of $y_{k,l}$ are combined to a new particle by adding their momenta. This procedure will be repeated until the minimal $y_{k,l}$ is greater than a given value y_{cut}. The set of tracks which are combined by this algorithm is called *jet*.
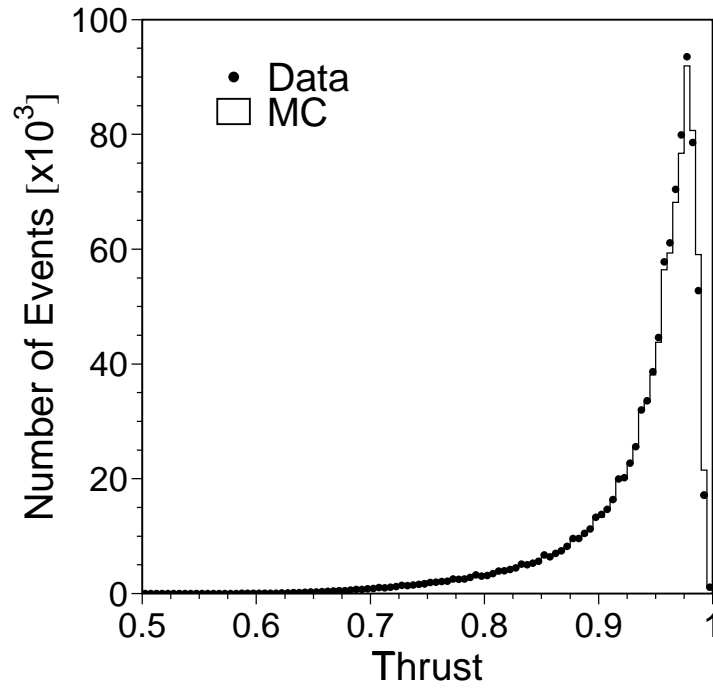
Figure 5.7: Distribution of the thrust value T (see formula 5.6).

Chapter 6

Measurement of R_b^0

The measurement of R_b^0 presented here is based on the precise tracking information provided by the Silicon Microvertex Detector. The analysis has been performed using about one million hadronic Z events collected in 1994 and 1995. In the next section the selection of hadronic events is presented followed by a detailed explanation of the tagging procedure using lifetime information. The method measuring R_b^0 presented here is based on a self-calibrating tagging method. After presenting the selection of hadronic events and giving an overview of methods to identify b quarks the self-calibrating double-tag method is discussed in detail.

6.1   Selection of Hadronic Z Events

The event selection for the process $e^+e^- \rightarrow$ hadrons is based on the evaluation of the energy depositions in the electromagnetic and hadronic calorimeters, and on a high particle multiplicity in the final state.

The selection strategy is based on the selection used for the L3 measurement of the hadronic cross section [88,89]. Hadronic events are selected using the following criteria:

1. $0.5 < E_{vis}/\sqrt{s} < 1.5$; where E_{vis} is the total energy observed in the detector.

2. $|E_{\parallel}|/E_{vis} < 0.6$; where $E_{\parallel}$ is the energy imbalance along the beam direction.

3. $E_{\perp}/E_{vis} < 0.5$; where $E_{\perp}$ is the transverse energy imbalance.
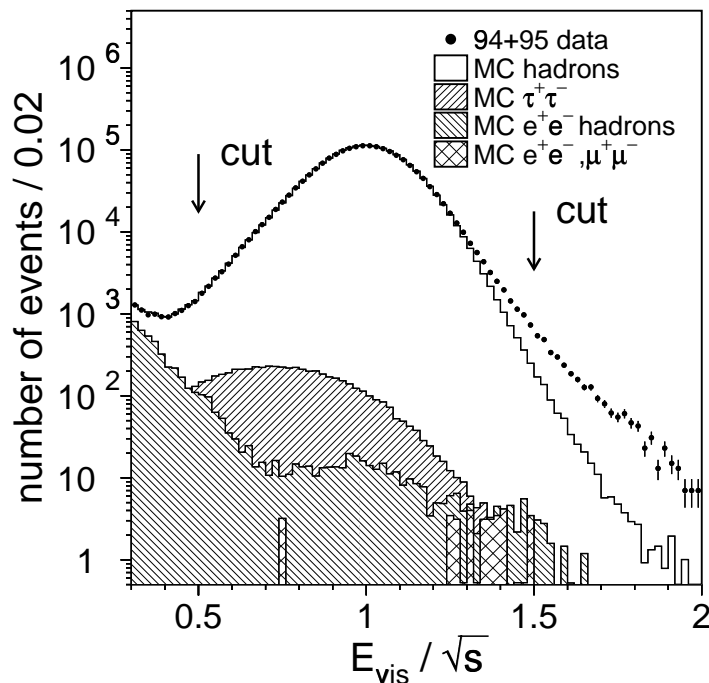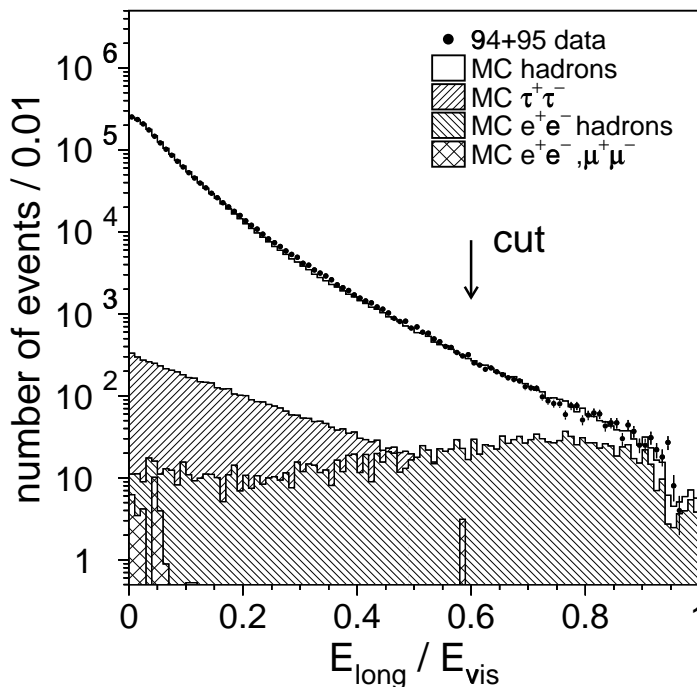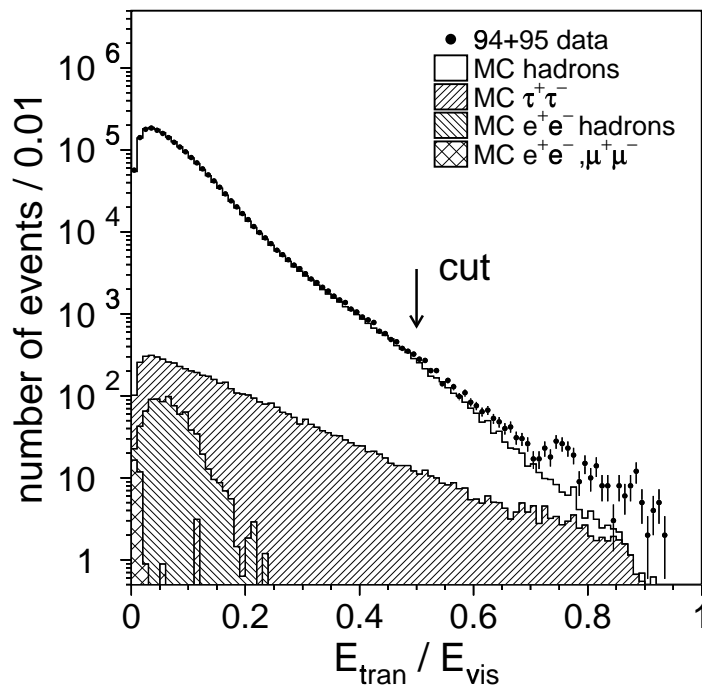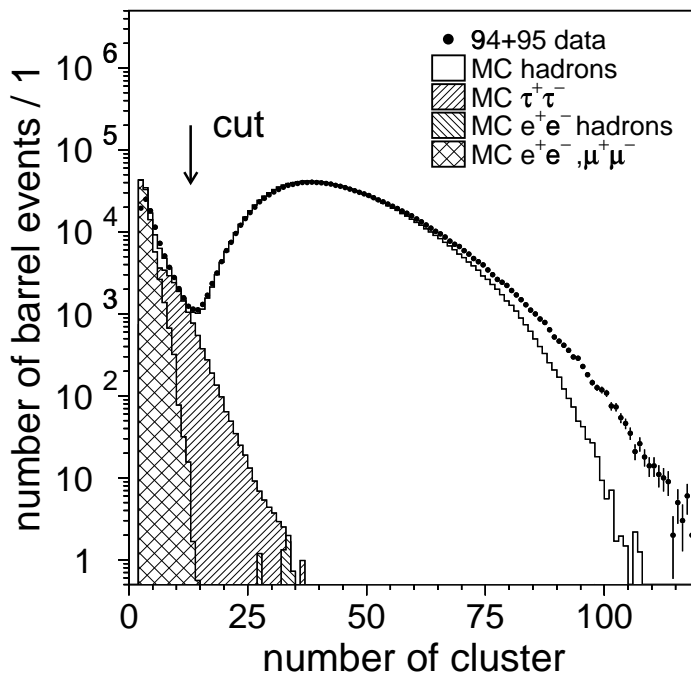
Figure 6.1: Distributions of the visible energy for hadronic events and the corresponding main background observed in the Monte Carlo . The data are represented by dots. The disagreement in the tail of the distributions is discussed in the text. The cut values for the hadron selection are depicted by the arrows.

4. The number of clusters reconstructed in the calorimeters is required to satisfy:
   $N_{Cluster} \geq 13$ for $|\cos\theta_T| < 0.74$ (barrel)

θ_T is the polar angle of the event thrust axis with respect to the beam pipe. The distributions are shown by figures 6.1, 6.2, 6.3, and 6.4. The main background components and the applied cuts are shown there. In two of these plots a disagreement between data and Monte Carlo in the tails of the distributions appear. The disagreement in the tail of the visible energy distribution is caused by the underestimation of the noise in the hadron calorimeter by the simulation. However, considering the logarithmic scale the effect begins two order of magnitude below the peak value. The disagreement in the tails of the number of cluster distribution results from a too small number of low energetic clusters from the simulation and has been investigated. One possible explanation could be, that the energy cut which leads to the stopping of the simulation of the particle propagation is too

Figure 6.2: Distributions of the longitudinal energy imbalance for hadronic events and the corresponding main background observed in the Monte Carlo . The data are represented by dots. The cut value for the hadron selection is shown by the arrow.

high. This cause the simulated particle to deposit the remaining energy in one cluster. However, a large amount of the affected events have been scanned and clearly identified as hadronic events.

The selection efficiency is determined using hadronic Monte Carlo events. These events have been generated with the JETSET and HERWIG Monte Carlo programs, passed through a simulation of the L3 detector [85] and were reconstructed by the L3 reconstruction program. The hadron calorimeter covers 99.5% of the full solid angle which results in a selection efficiency of $(99.19 \pm 0.10)\%$. The uncertainty on this number is estimated by comparing different fragmentation models as implemented in the generators mentioned above. The largest background with a fraction of $(0.20 \pm 0.02)\%$ comes from the process $e^+e^- \rightarrow \tau^+\tau^-$. The background from all other Z decays is negligible. The fraction of non-resonant background, e.g., two-photon processes, beam-gas interaction and cosmic rays, amounts

Figure 6.3: Distributions of the transversal energy imbalance for hadronic events and the corresponding main background observed in the Monte Carlo . The data are represented by dots. The cut value for the hadron selection is depicted by the arrow.

to $(0.10 \pm 0.04)\%$.

A few additional requirements ensure that the events are useful for an analysis based on lifetime information:

1. Event must pass the bad run selection: events from runs with known SMD or TEC problems, *e.g.*, power off, large noise etc.) are discarded.

2. $|\cos\theta_{\mathrm{T}}| < 0.7$; the event axis must point into a fiducial region delimited by the barrel part of the detector.

3. $N_{\mathrm{tracks}} > 4$; where N_{tracks} is the number of reconstructed tracks per event.

4. $N_{\mathrm{jets}} \geq 2$; where N_{jets} is the number of reconstructed jets per event.

5. A primary vertex must be found.

Figure 6.4: Distributions of the number of clusters for hadronic events and the corresponding main background taken from the Monte Carlo . The data are represented by dots. The disagreement in the tail of the distributions is discussed in the text. The cut value used for the hadron selection is shown by the arrow.

After applying all the selection criteria about 970.000 hadronic events are selected from the data taken in the years 1994 and 1995. This corresponds to an integrated luminosity of $\mathcal{L} \approx 71$ pb^{-1}. The following table gives the amount of events which are accepted after applying different selection cuts. The number are given relative to number of events passing the hadron selection.

Cut	Events Passing	Events Accepted
Hadron Selection	1.758.626	100.0%
Bad Run Rejection	1.674.034	95.2%
Thrust in Barrel	1.049.190	59.6%
Number of Jets	1.047.474	59.5%
Reconstructed PV	968.964	55.1%

6.2 Tagging of Heavy Quarks using Lifetime Information

In chapter 3 can be read about details of production and decay of heavy quarks. It was pointed out that due to a missing theory which can describe the process of the hadronisation in a consistent way different models are used. That leads to model uncertainties which has to be taken into account carefully.

The decay of B hadrons is characterised by a relatively long lifetime, a large charge multiplicity and a large fraction of energy retained from the initial b quark. The latter leads to large boost on one hand and a small amount of particles coming directly from the fragmentation on the other hand. These properties enables the topological separation of B and D hadrons. In case of light quarks a large fraction of tracks comes directly from the fragmentation and only a small part of the initial quark energy is carried by the hadron in the final state. By reconstructing the secondary vertex these properties are exploited to identify B mesons and hence the initial b quark. The identification is called 'tagging'.

6.2.1 Decay Length Tag

There are two variables that are mainly used for tagging using lifetime information. The most straightforward is the *decay length*, which is the distance from the interaction point to the decay point. The interaction point and the decay point are called primary and secondary vertex, respectively. The primary vertex is estimated on an event by event basis by taking all tracks that are consistent with originating from the same point. The secondary vertex is estimated by taking all tracks in a single jet that are consistent with originating from one point separated from the interaction point. The decay length depends on the lifetime, τ, of the decaying particle and on its energy:

$$L = \gamma \beta c \tau \,,$$

where γ and β are Lorentz boost factors of the B hadron:

$$\gamma = \frac{E}{m}, \qquad \beta = \frac{p}{E}.$$

Hence, to measure the lifetime an estimate of the momentum is required. With a lifetime of about 1.5 ps and a momentum of about 30 GeV, B hadrons decay after 2-3 mm, *i.e.*, still inside the LEP beam pipe.

6.2.2 The Impact Parameter Tag

In addition to the decay length, which is a joint property of a number of tracks, it is also useful to measure the *impact parameter*. The impact parameter is a property of each track and can be used even when a secondary vertex has not been reconstructed.
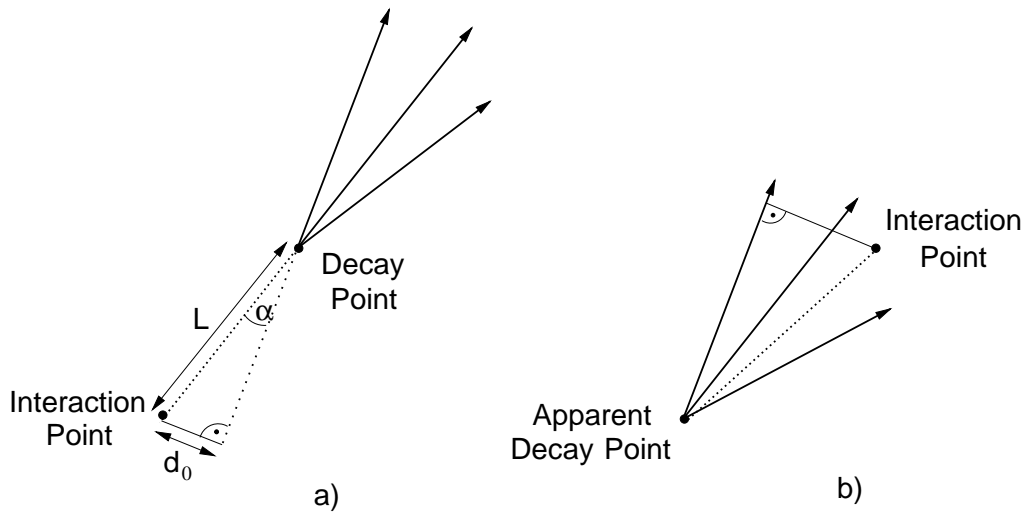
Figure 6.5: a) Schematic presentation of the definitions of decay length and impact parameter, as given in the text. b) Example of a topology where the apparent decay point is reconstructed on the wrong side of the interaction point leading to negative values of impact parameter and decay length.

The impact parameter is defined as the positive DCA of a track with respect to the nominal interaction point, provided with a sign as explained in figure 6.5. The DCA is given by $d_0 = L \sin \alpha$. The angle, α, of the track in the laboratory frame can be related to the decay angle, $\hat{\alpha}$, in the rest frame of the decaying particle by $\sin \alpha = \sin \hat{\alpha}/(\gamma(1 + \beta \cos \hat{\alpha}))$ such that

$$d_0 = \frac{\beta\tau\sin\hat{\alpha}}{1 + \beta\cos\hat{\alpha}}. \tag{6.1}$$

In the ultra-relativistic case, the impact parameter is independent of momentum or energy of the parent heavy quark. Hence, unlike the decay length, a precise knowledge of the parents energy is not required.

The sign is used to distinguish measured DCA's resulting from real secondary vertices from those which are associated wrongly due to resolution effects of the detector. The impact parameter is defined positive if the extrapolation of the linearised track intersects the direction of the associated jet in the direction of the momentum of the jet and negative if it intersects opposite to that direction with respect to the primary vertex.

6.2.3 Tagging Probabilities

In figure 6.6 two typical q$\bar{\text{q}}$ events as reconstructed by the L3 detector are shown. The q$\bar{\text{q}}$ event representing light quarks (u, d, s) is characterised by having only one joint vertex. For the b$\bar{\text{b}}$ event both the primary vertex and the secondary vertices, and the resulting large track DCA's can be clearly seen.

The main idea of the impact parameter tag, applied in this analysis, is to quantify whether tracks are consistent with the primary vertex or not. In order to define a probability that tracks are consistent with the primary vertex one considers the so-called *resolution function*. The resolution function reflects the precision of the vertex detector and hence the eligibility to conclude from the impact parameter of a track, that the track originates from the primary vertex or not.

The key quantity is the *impact parameter significance* which is given by the ratio of the impact parameter and its error:

$$x = \frac{IP}{\sigma_{IP}}. \tag{6.2}$$

The error of the impact parameter, σ_{IP}, is composed of the contribution from the intrinsic DCA resolution, the contribution from the multiple scattering and the contribution from the primary vertex error. Figure 6.7 shows the distribution of track significances of hadronic events. The negative part resulting from detector
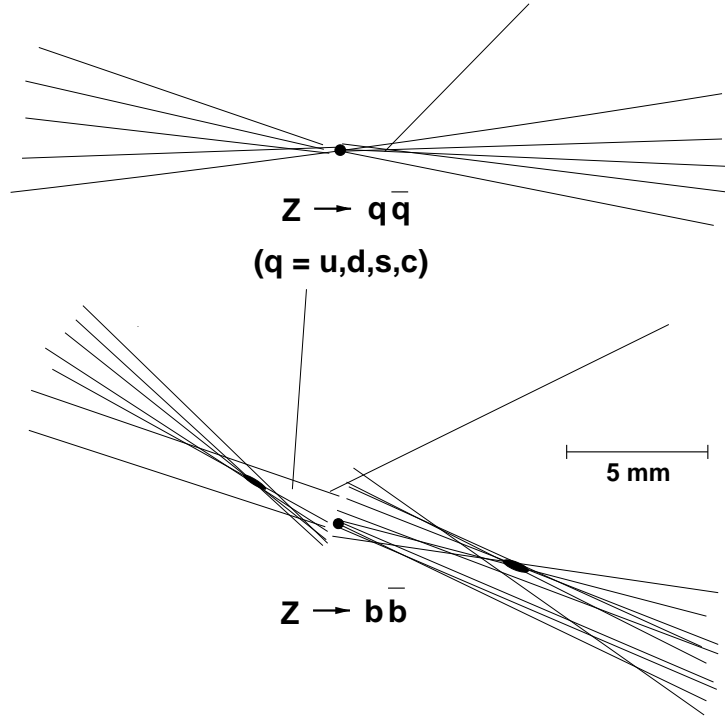
Figure 6.6: Graphical representations of q$\bar{\text{q}}$ events close to the e$^+$e$^-$ interaction point, projected onto a plane perpendicular to the beam axis. In the event Z → b$\bar{\text{b}}$ the lifetime can be clearly seen by tracks forming secondary vertices or having a large DCA ($\mathcal{O}$(1mm)). The black point indicates the centre of the beamspot. Note, that all track segments seen in the picture are reconstructed by combining hits of detector components which are out of this scale. The first detector layer is located in a distance of 60 mm from the centre of the detector (interaction region).

resolution has been mirrored (dotted line) in order to emphasise the asymmetric shape of this distribution. The excess of tracks on the positive side corresponds to their large probability coming from a secondary vertex.

In order to separate these two classes of tracks, a probability that a track with an impact parameter significance s is originating from the primary vertex is defined by:

$$P(s) = \frac{\int_s^\infty R(x)dx}{\int_0^\infty R(x)dx} \tag{6.3}$$

The resolution function, R(x), is the distribution of the absolute values of the
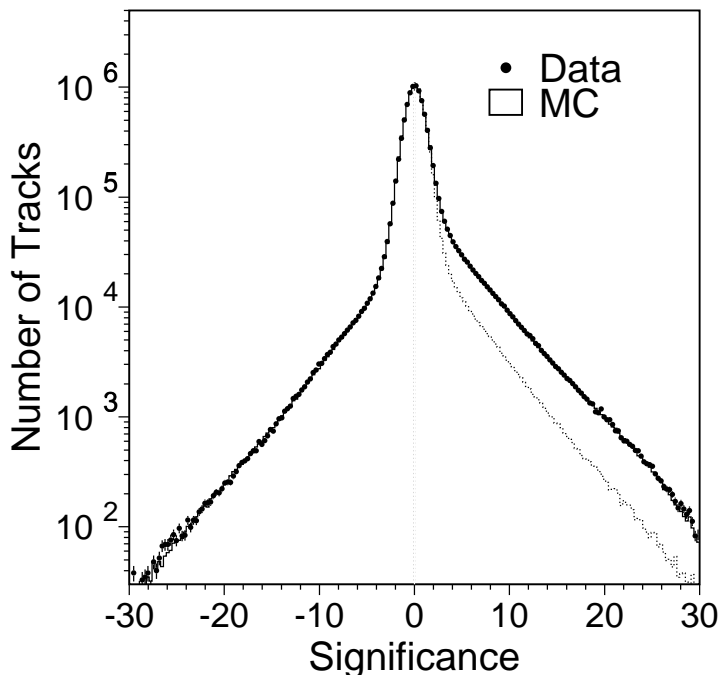
Figure 6.7: Significance distribution of q$\bar{\mathrm{q}}$ events of the 1994 and 1995 data and Monte Carlo sample. The negative part corresponds to the resolution of the detector. For clarity, the negative part has been mirrored (dotted line). The surplus on the positive side depict the capability to tag tracks as not originating from the event vertex. Data and MC are in very good agreement.

negative part of the impact parameter significance distribution and can be derived from data. P(s) varies between 0 and 1. Tracks with lifetime information have low P(s) values. For n tracks a combined probability can be defined by $\prod_{i=1}^{n} P_i$. It depends strongly on the number of tracks, n.

In order to avoid this problem a modified probability function firstly proposed by the ALEPH Collaboration [90] is used:

The individual track probability is considered as a point inside a n-dimensional hypercube of unit volume. The idea is to calculate the fractional hyper-area given by points having equal or less differential probability $\prod = \prod_{i=1}^{n} P_i$. Using the fact that the n-cube has unit hyper-volume the converse of this hyper-area is calculated by:
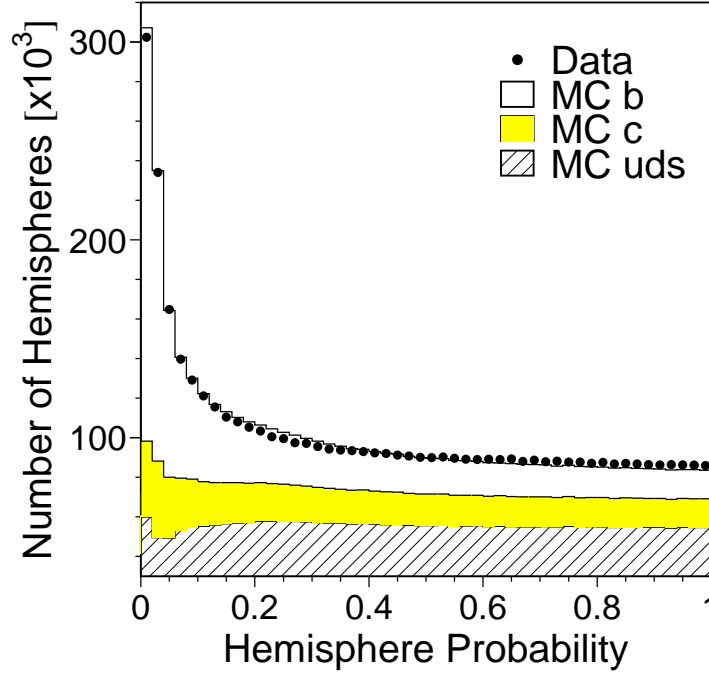
Figure 6.8: The probability distribution that tracks of a hemisphere originating from the primary vertex. The subdivision of the MC distribution into the different flavours shows clearly that tracks which are not belonging to the primary vertex come mainly from B decays.

$$P = 1 - \int_{\prod_{i=1}^{N} x_i}^{(1,1,...,1)} dx_1 dx_2 ... dx_n. \tag{6.4}$$

One can render the complicated boundary condition of this integral by unnesting them as:

$$P = 1 - \int_{\prod}^{1} \int_{\prod / x_n}^{1} \int_{\prod / x_n \cdot x_{n-1}}^{1} \cdots \int_{\prod / \prod_{i=2}^{n} x_i}^{1} dx_1 dx_2 ... dx_n. \tag{6.5}$$

In case of a single track (n=1), $\prod P_i = P_i$ can be recovered. In case of two tracks one finds $P = \prod_{i=1}^{2} x_i = \prod \cdot (1 - \ln \prod)$. It can be shown by induction that the probability that a set of n tracks is consistent with the primary vertex can be calculated by:
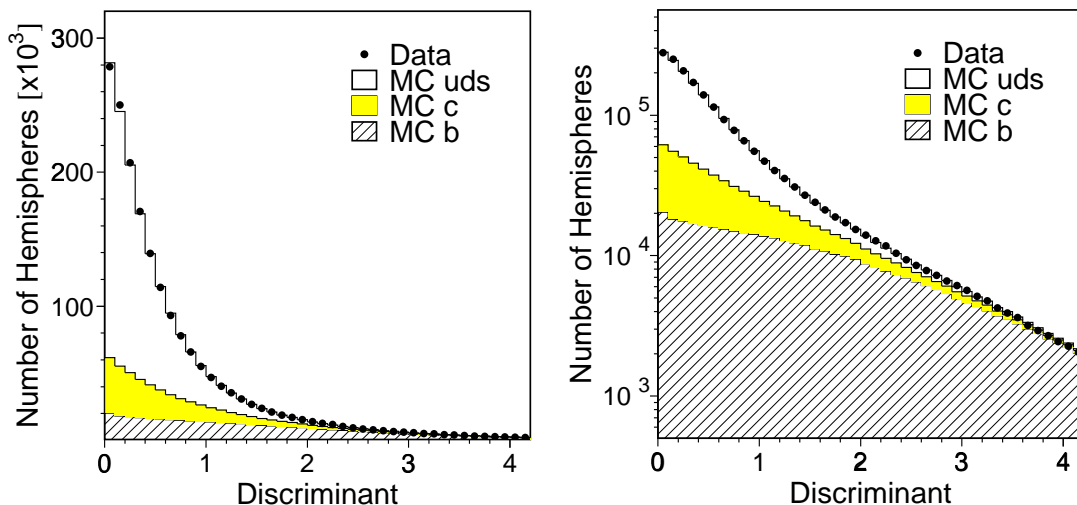
Figure 6.9: The distribution of the discriminant variable of a hemisphere in linear and logarithmic scale. It is evident, that larger discriminint variables lead to higher fraction of $b\bar{b}$ events in the sample.

$$P = \prod_{i=1}^{n} P_i \sum_{j=0}^{n-1} \frac{(-ln \prod_{i=1}^{n} P_i)^j}{j!} \tag{6.6}$$

This quantity is also distributed between 0 and 1. By construction, the probability of groups of tracks originating from the primary vertex is distributed flat. If the group includes tracks coming from the secondary vertex, the distribution peaks at low values of P. Figure 6.8 shows the hemisphere probability distribution for the different quark flavours using Monte Carlo information. It can be clearly seen, that for low probabilities hemispheres containing b quarks can be well separated from the hemispheres containing lighter quarks. The overall distribution is in good agreement with the hemisphere probability distribution from data.

The experimental variable finally used is defined by:

$$D = - \log_{10} P \tag{6.7}$$

and is further called the *discriminant variable*. Figure 6.9 depicts the distribution of the discriminant variable for tracks belonging to a hemisphere. Both representations show that larger values of the discriminant variable correspond to higher

fractions of b$\bar{\text{b}}$ events in the sample. Large values of D indicate lifetime information in the track sample whereas small values of D allow the assumption that all tracks of the sample originate from the primary vertex.
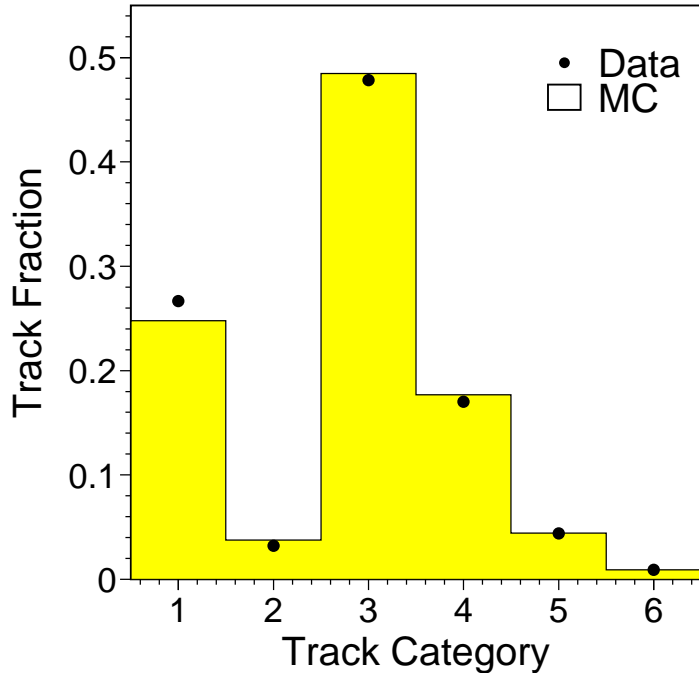
Figure 6.10: Fraction of the six track categories relative to all tracks in comparison between data and Monte Carlo.

The tracks retained for the calculation of D have to fulfil the following quality criteria which are optimised to give a high tagging efficiency:

- the track should have at least 30 associated hits spanned over a radial distance which corresponds to 40 TEC anode wires along the track;

- the rϕ projection of the DCA has to be less than 1.5 mm for tracks with SMD information and less than 3 mm for tracks without SMD information;

- the angular separation of the track from the anode and cathode planes of the TEC, where the resolution is degraded, should be more than 11 mrad;

- if a track has no SMD hits, at least 2 hits from an inner TEC segment should be used in the track fit.

Not all tracks have associated hits in both SMD layers. Since the resolution of the tracking and associated error assignment is different for tracks with different SMD hit pattern, tracks are classified into six track categories (see section 5.2, page 64). The fraction of tracks in the different category classes are shown in figure 6.10. For a perfect microvertex detector (and a perfect tracking system) all tracks are expected to be in category four, five, and six. Because of the finite SMD efficiency a large number of tracks are moved to lower categories and hence a degration of the best track quality is seen.
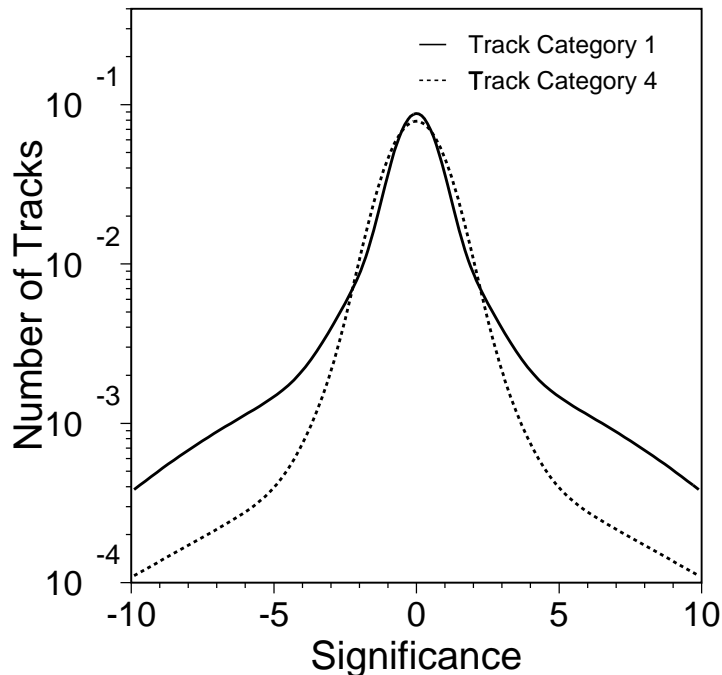
Figure 6.11: Normalised resolution functions of track categories 1 and 4 (see text). Because of the different shapes resolution functions are built for each track category separately.

The assignment of tracks to different hit pattern categories is exploited in calculating the track probability. Separate resolution functions are constructed for

each data taking period and each track category by fitting the negative side of the impact parameter significance distribution for corresponding tracks. Figure 6.11 shows the comparison of the fitted resolution function for tracks of the categories one and four[1]. For technical reasons the negative significance distributions are symmetrised. Considering figure 6.7 the motivation of using separate resolution functions becomes clear. The resolution functions and the corresponding data distributions of all track categories are depicted in figure 6.13. The r.m.s width of the significance in each class is compatible with one, but the distributions have substantial tails. Therefore, a model of the resolution function is constructed as the sum of two Gaussian functions and an exponential tail.
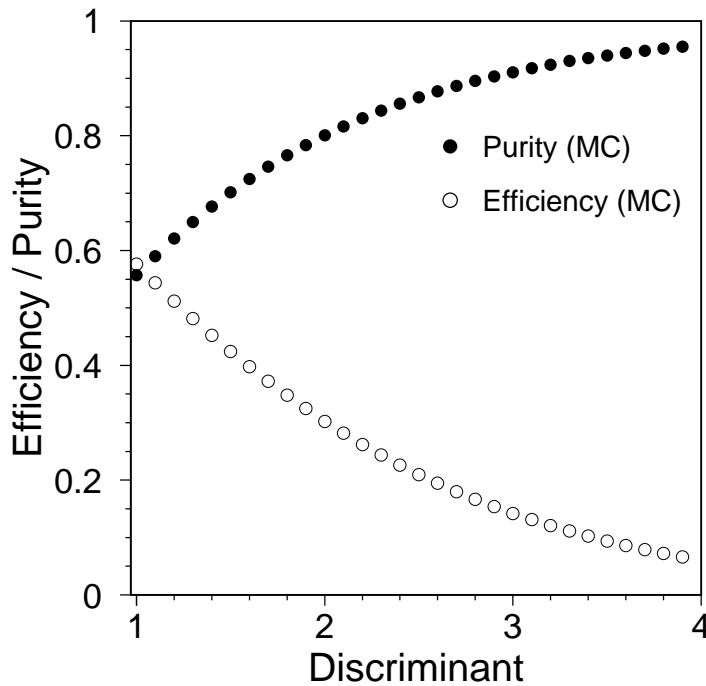
Figure 6.12: B tag efficiency and purity as a function of the discriminant cut determined from the Monte Carlo.

Using these functions one is able to compute the probability that the tracks of an event (or of a hemisphere) are originating from a joint vertex, *i.e.*, the primary

---

[1]Except the categories five and six, which corresponds to the 10% overlap of the inner layers, category four is the one with the most associated SMD hits.

vertex. An event (hemisphere) is tagged as originating from the process $Z \to b\bar{b}$ when its discriminant (formula 6.7) is greater or equal than D_{cut}.

6.2.4   Purity and Efficiency

A certain discriminant value corresponds to certain quantities of efficiency and purity. The b tagging efficiency is defined as:

$$\epsilon_b = \frac{\text{Number of b hemispheres tagged}}{\text{Total number of b hemisphere}} , \qquad (6.8)$$

and the b purity is:

$$\eta_b = \frac{\text{Number of b hemispheres tagged}}{\text{Total number of tagged hemisphere}}. \qquad (6.9)$$

The efficiency and purity of the b tag applied in this analysis are shown in figure 6.12. Both quantities has been taken using the Monte Carlo simulation. Later, the b tag efficiency are determined directly from data by the double-tag method. Both results are compared in chapter 7.

R_b^0 is initially measured as a function of the discriminant cut D_{cut}. The cut value used for the final result is then chosen to optimise the measurement precision.
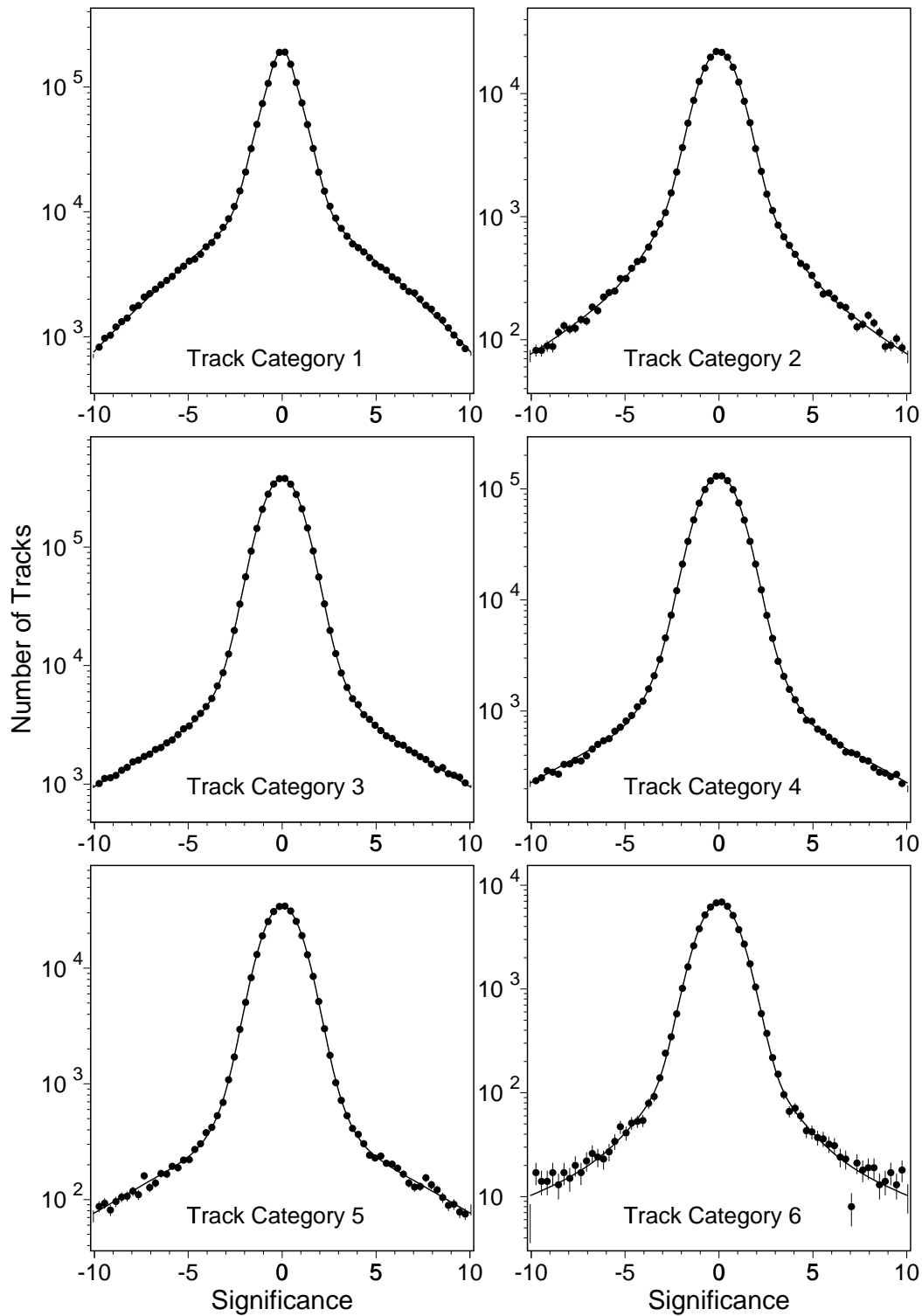
Figure 6.13: The fitted resolution functions for the longest data taking period. The six track categories are explained in the text. With increasing number of SMD hits the fraction of tracks in the tails becomes smaller.

6.3   The Double Tag Technique

The measurement of R_b in this analysis is based on the double-tag technique. This technique allows to deduce simultaneously both R_b and the efficiency for tagging b quarks from data and hence is self-calibrating. Typically, the quark and anti-quark pair originating from a Z decay is produced back-to-back in the Z restframe and hence the quarks enter into two hemispheres. Each event has the potential to be tagged twice. The number of tagged hemispheres, N_t, is related to the total number of hadronic events as follows:

$$\frac{N_t}{2N_{had}} = \epsilon_b R_b + \epsilon_c R_c + \epsilon_{uds} R_{uds} \tag{6.10}$$

$$= \epsilon_b R_b + \epsilon_c R_c + \epsilon_{uds}(1 - R_c - R_b) \tag{6.11}$$

where ϵ_b, ϵ_c and ϵ_{uds} are the efficiencies to obtain a tag from hemispheres containing jets which are originating from b, c or light quarks, respectively. The number of events with both hemisphere tagged, N_{tt}, is given by:

$$\frac{N_{tt}}{N_{had}} = \epsilon_b^d R_b + \epsilon_c^d R_c + \epsilon_{uds}^d(1 - R_c - R_b) \tag{6.12}$$

The parameter ϵ^d is the probability that both hemispheres of an event are tagged simultaneously, the *double-tag efficiency*. In first approximation the double-tag efficiency is equal to the single tag efficiency squared. For a precise measurement this assumption is not sufficient, the deviation has to be taken into account:

$$\epsilon^d = c \; \epsilon^2 \tag{6.13}$$

The parameter c is called *hemisphere correlation* factor and quantifies the efficiency correlation between the two hemispheres. Thus, equation 6.12 can be modified by:

$$\frac{N_{tt}}{N_{had}} = c_b \epsilon_b^2 R_b + c_c \epsilon_c^2 R_c + c_{uds} \epsilon_{uds}^2 (1 - R_c - R_b) \tag{6.14}$$

Using the system of two equations 6.11 and 6.14 and if the correlation parameters, ϵ_c, and ϵ_{uds} are calculated from the simulation and R_c is imposed from other measurements or from the Standard Model, R_b and ϵ_b can be measured simultaneously

from the data. Thus, a precise knowledge of the details of B hadron decays is not required.

With the simplification that ϵ_c and ϵ_{uds} are negligible in comparison to ϵ_b one can write:

$$R_b \simeq \frac{N_t^2}{4 N_{had} N_{tt}} c_b \,, \tag{6.15}$$

$$\epsilon_b \simeq \frac{N_t}{2 N_{had} R_b} \,. \tag{6.16}$$

The error on the efficiency correlation contributes directly to the error on R_b, so an accurate evaluation of c_b is essential for this measurement.

6.4 Hemisphere Efficiency Correlations

As mentioned above the method of measuring R_b is based on the subdivision of each event into two hemispheres. The tagging of a b quark in a hemisphere - the tagging of the hemisphere - is performed independently of the opposite side. Naïvely one would expect that the probability to tag b quarks in both hemispheres simultaneously is equal to the square of the probability to tag b quarks in one hemisphere of the event. But, in reality, it can be observed that the tagging efficiency of both hemispheres are correlated. The probability to tag both hemispheres simultaneously (ϵ^d) and the probability to tag one of each hemisphere independently (ϵ) are associated by the correlation parameter:

$$c = \frac{\epsilon^d}{\epsilon^2} = \frac{\langle \epsilon \, \bar{\epsilon} \rangle}{\langle \epsilon \rangle \langle \bar{\epsilon} \rangle} \tag{6.17}$$

In order to quantify the hemisphere efficiency correlation Monte Carlo information is used to identify the main contributions. If the sum of the contributions is in agreement with the total correlation the same correlation components are determined from data. The deviations between the correlation components from Monte Carlo and data are taken as component uncertainties.

Possible correlation sources are discussed below. Beforehand the procedure to calculate the individual contributions is deduced and explained in detail.

Method for the Determination of a Correlation Component

Taking the step function as probability, so that

$$
\Theta = \left\{ \begin{array}{ll} 1 & - \quad \text{hemisphere is selected} \\ 0 & - \quad \text{hemisphere is not selected,} \end{array} \right. \tag{6.18}
$$

the probability to tag both hemispheres in N events, can be expressed by:

$$
\epsilon^d = \frac{1}{N} \sum_{i=1}^{N} \Theta_1^i \Theta_2^i. \tag{6.19}
$$

By the subdivision of each hemisphere into bins of a specific experimental value, the step function Θ_1^i can be replaced by $\Theta_{j(k)}^i$, the probability to tag hemisphere 1(2) if the value was found in bin j(k). So equation 6.19 can be written as:

$$
\epsilon^d = \frac{1}{N} \sum_{i=1}^{N} \; \sum_{j=1}^{n} \sum_{k=1}^{n} \Theta_j^i \Theta_k^i \; . \tag{6.20}
$$
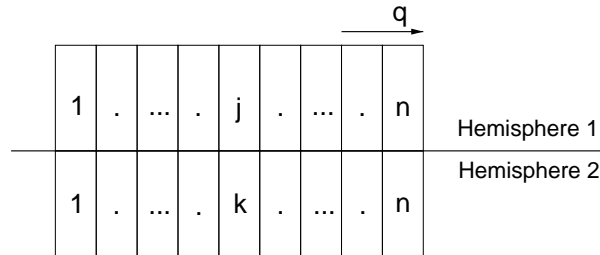
Figure 6.14: Schematic of the two event hemispheres and bins related to the distribution of an experimental observable q.

If N_{jk} is the number of events, in which the variable belongs to cell j of hemisphere 1 and to cell k of hemisphere 2, the event index i can be eliminated by:

$$
\epsilon^d = \sum_{j=1}^{n} \sum_{k=1}^{n} \frac{N_{jk}}{N} \epsilon_j \epsilon_k \; . \tag{6.21}
$$

The step functions Θ_j have been replaced by ϵ_j, the probability that a variable q was found in the bin j of the tagged event hemisphere.

In order to get an equation of the form $\epsilon^d = \epsilon\epsilon^{co}$, where ϵ^{co} is the *co-tag efficiency*, the efficiency of a hemisphere when the opposite one has been tagged - the following substitution is performed:

$$\epsilon^d = \epsilon \sum_{j=1}^{n} \epsilon_j \sum_{k=1}^{n} \frac{N_{jk}}{N} \frac{\epsilon_k}{\epsilon} . \tag{6.22}$$

Hence, one can separate a distribution which is experimentally accessible:

$$C_j = \frac{1}{\epsilon} \sum_{k=1}^{n} \frac{N_{jk}}{N} \epsilon_k. \tag{6.23}$$

Here, C_j is the normalised distribution of the variable q in a hemisphere, if the opposite one has been selected. After transition to continuous distributions of q, the co-tag efficiency can be written as follows:

$$\epsilon_q^{co} = \int dq \ \epsilon(q)C(q). \tag{6.24}$$

The hemisphere efficiency correlation parameter caused by a specific experimental observable can be estimated by:

$$c_q = \frac{\epsilon_q^d}{\epsilon^2} = \frac{\epsilon_q^{co}}{\langle\epsilon\rangle} = \frac{1}{\langle\epsilon\rangle} \int dq \ \epsilon(q)C(q). \tag{6.25}$$

A possible source of correlation can be quantified by considering variables q for each hemisphere which could be influenced by tagging the opposite hemisphere. For a particular cut on the hemisphere discriminant three distributions are defined:

- The average hemisphere tagging efficiency, $\langle\epsilon\rangle$.

- The single hemisphere tagging efficiency as a function of q, $\epsilon(q)$

- The normalised distribution of q in a co-tagged hemisphere, $C(q)$. A co-tagged hemisphere is the opposite to a tagged hemisphere, regardless of whether it is tagged itself.

Study of Relevant Correlation Components

The analysis is performed on several candidate variables q. For a $b\bar{b}$ Monte Carlo sample, the sum of the separate components is then compared to the total efficiency correlation factor c_q. A reasonable agreement between them means that the main sources of correlation have been identified. The following sources have been determined to be relevant:
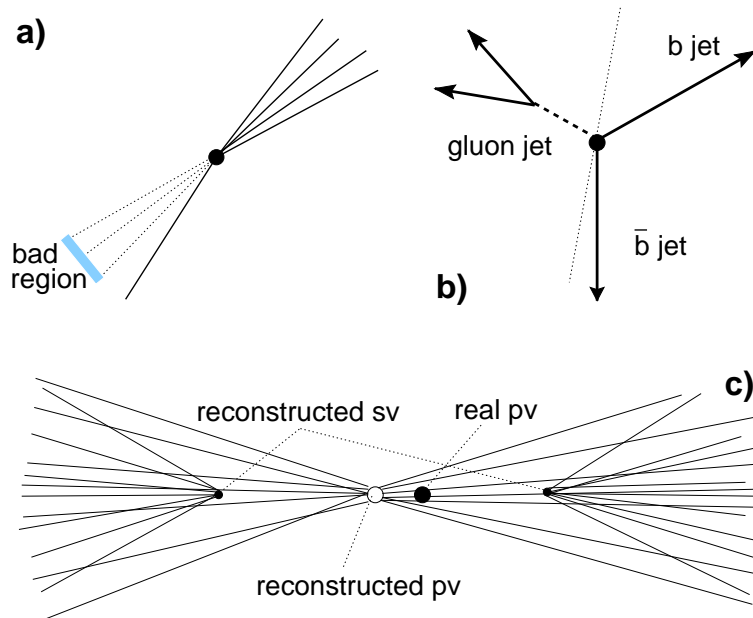
Figure 6.15: Illustration of possible hemisphere correlation sources. a) A bad region of the detector causes badly reconstructed tracks and hence a loss in the tagging efficiency in this hemisphere. b) The emission of a hard gluon. Energy is taken away from both b quarks and in an extreme case both b quark jets are forced to point into the same hemisphere. c) A displaced reconstructed primary vertex (white circle) with respect to the real event vertex (black circle) causes a systematic shift in the reconstructed decay length and hence also in the b tagging probability.

- **Geometric effects:** Bad regions of the detector can lead to efficiency correlations. The back-to-back nature of the event leads to a positive correlation in the polar angle. With increasing polar angles the contribution from multiple scattering to the track error decreases. At the end of the SMD some of the tracks are pointed outside the geometrical acceptance. This decreases

the tagging probability in both hemispheres. The angular correlation components are estimated using $q = \cos\theta$ and $q = \phi$ where θ and ϕ are the polar and azimuthal angles of the most energetic jet in each hemisphere.

- **Vertex effects:** Both hemispheres use the same primary vertex, which is determined as explained in section 5.2. The main effect arises because the primary vertex fit may also include some tracks coming from B-hadron decays (negative correlation). To quantify the effect, a primary vertex is constructed separately in each hemisphere using only the tracks assigned to it. The variable q is taken to be the distance in the xy plane between the vertex in each hemisphere and the overall event vertex. Its sign is given according to how far each hemisphere vertex moves when the 200-event vertex constraint is removed: the positive sign is assigned to the hemisphere with the larger movement.

- **Kinematics effects:** The presence of hard gluons in the event can influence the tagging efficiency of both hemispheres in two ways: a) by taking energy away from the primary quarks. This lowers the b tagging efficiency, which leads to a positive correlation or, b) in an extreme case, by pushing both quarks into the same hemisphere, leading to a negative correlation. The signed event thrust, $q = \pm T$, is used as a probe. The positive sign is assigned to the hemisphere containing the jet with the largest energy.

By means of the polar angle θ, the method of estimating the correlation component is now explained in detail. The momentum vectors of both B hadrons are pointed predominantly into opposite directions - they are highly correlated: In the rest frame of the Z, which is identical with the laboratory system, the quark and anti-quark are travelling in opposite directions and fragment into jets with opposite momentum directions. In order to investigate polar angle effects causing hemisphere correlations the polar angle of the jet has been taken to be relevant. Figure 6.16a shows the polar angle distribution of b jets from Monte Carlo (selected and unselected). The dotted line in this figure represents the distribution of a hemisphere, if the opposite one is selected. Both distributions are normalised to one. It can be clearly seen, that by tagging one hemisphere the distribution of the opposite hemisphere is modified (relative to the overall distribution). Figure 6.16b

shows the distribution of the selection efficiency of one b hemisphere as a function of the polar angle $\cos\theta_{\text{jet}}$ applying a discriminant cut of $D_{\text{cut}} = 2.3$. The average selection efficiency is indicated by the dotted line. Using formula 6.25 the correlation factor caused by the correlation due to polar angle effects can be calculated. Figure 6.17a shows the correlation parameters of different sources as a function of the discriminant cut. The dominant components are those due to gluon radiation and vertex bias. There is a remaining discrepancy between the linear sum of the correlation components resulting from the three sources considered and the total correlation factor. That can be explained by an interference between the different sources and by additional sources of smaller relevance. For instance, ϕ and vertex effects are intrinsically correlated, since the primary vertex uncertainty is affected by the ϕ dependent beam spot size.

In order to estimate the uncertainty of the efficiency correlation parameter taken from Monte Carlo, a data sample with a b-purity of 70% is selected by requiring the event discriminant to be greater than 1.5 (see figure 7.2). The same cut is applied to the Monte Carlo sample. The correlation coefficients are calculated for each of the four sources in data and Monte Carlo. Figure 6.17b shows the deviations between data and Monte Carlo of each component and the linear sum. The correlation used as input parameter for calculating R_b is the total correlation from the simulation corrected by half the difference of data and Monte Carlo component sum. The uncertainty is estimated by adding the corrections of the different components in quadrature.
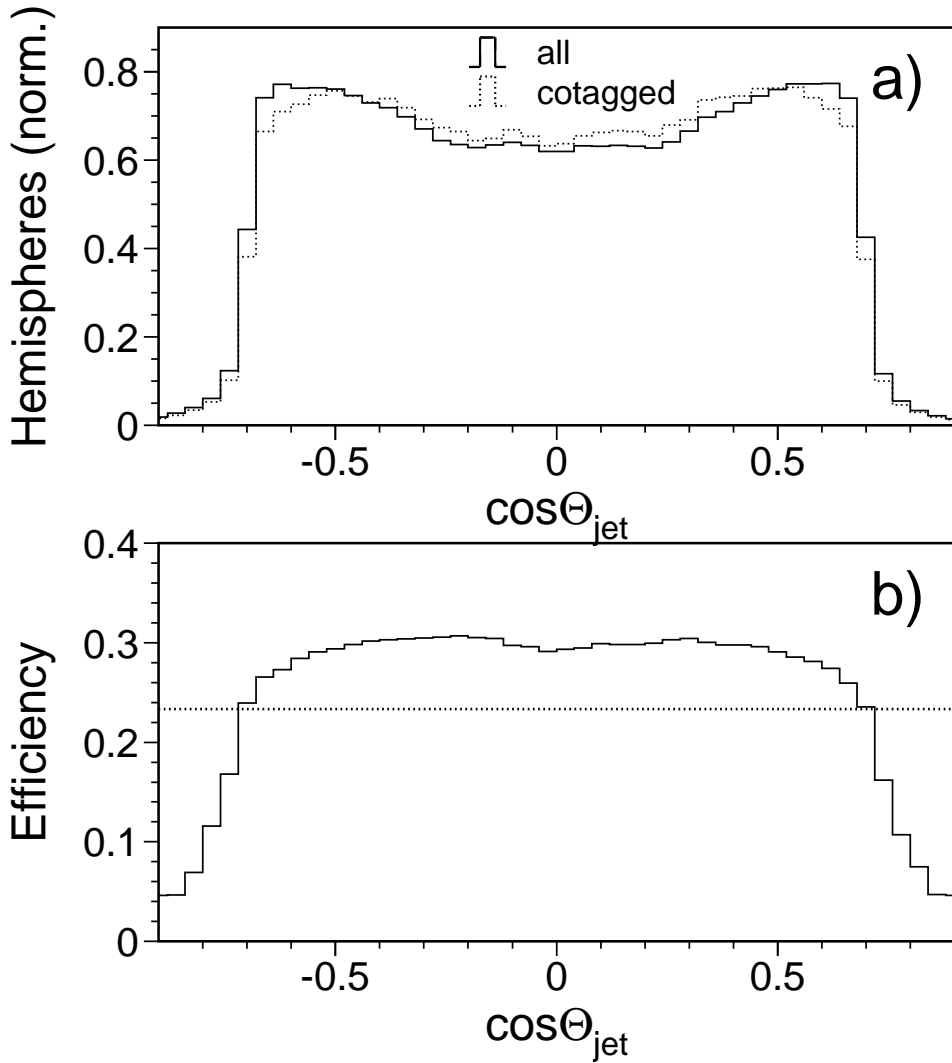
Figure 6.16: a) Monte Carlo distribution of $\cos\theta$ of the jet in all hemispheres (solid line) and of the opposite of a tagged hemisphere (dashed line) using a discriminant cut of $D_{cut} = 2.3$. It is clearly visible that if one hemisphere is tagged, the opposite one tends to point more predominant into the barrel region of the detector ($\cos\theta \leq 0.7$). b) The hemisphere selection efficiency as a function of $\cos\theta_{jet}$. The average efficiency is depicted by the dashed line.
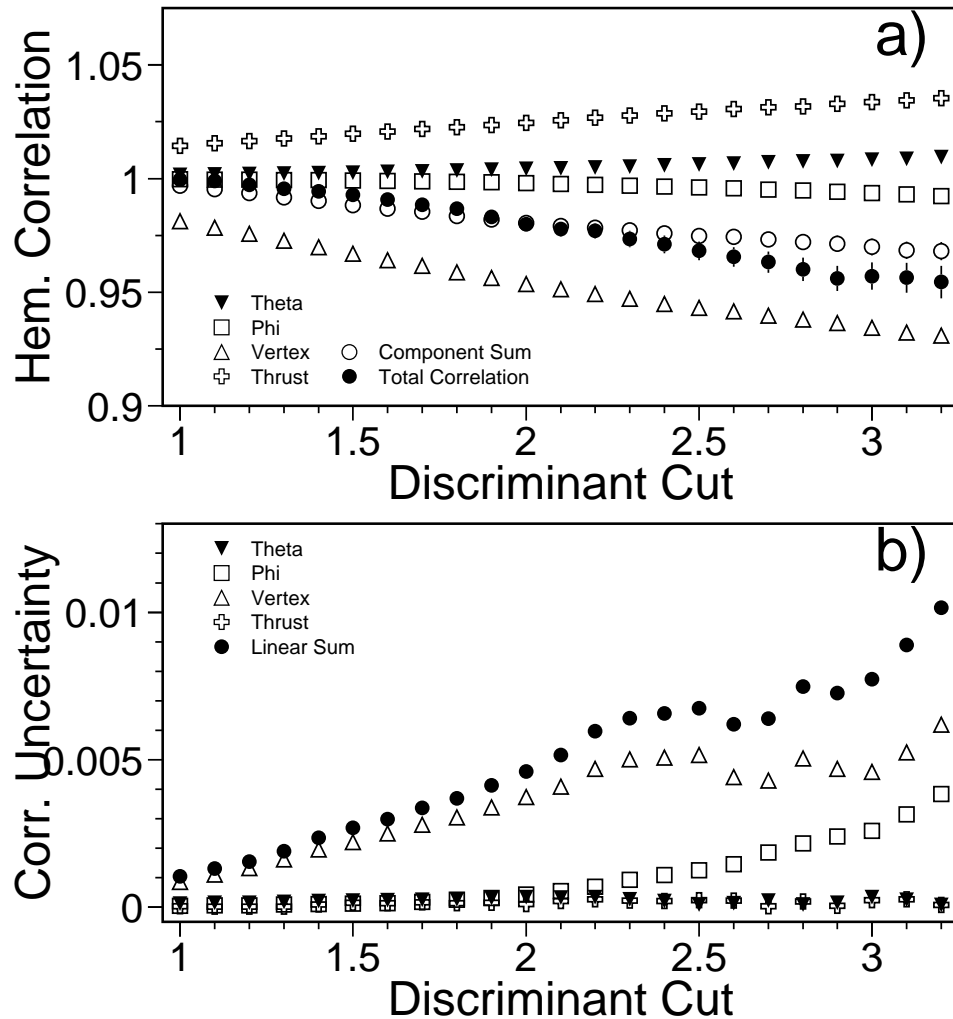
Figure 6.17: a) Correlation components, sum and the total correlation as function of the discriminant cut in the Monte Carlo. In the region of the final cut the agreement of the component sum and the total correlation is reasonable. b) The uncertainties of the correlation components estimated as explained in the text. The dominant contribution comes from the vertex bias. The filled dots show the linear sum of the different uncertainties.

Chapter 7

Results and Error Discussion

The double-tag method is based on the system of the two equations 6.11 and 6.14 (section 6.3). N_t, N_{tt}, and N_{had} are measured from data, whereas the background efficiencies ϵ_c, ϵ_{uds}, and the hemisphere efficiency correlation factor c_b are determined from Monte Carlo. For the relative rate of c quark production, $R_c = \frac{\Gamma_{c\bar{c}}}{\Gamma_{had}}$, the Standard Model prediction of 0.172 [27] is used. All input values given here are obtained with a hemisphere discriminant cut of $D_{cut} = 2.3^1$ .The determination of the hemisphere efficiency correlation is described in detail in section 6.4. The correlation factors are constructed in such a way that c = 1 represents no correlation, c > 1 a positive and c < 1 an anti-correlation between the tagging in the two hemispheres. The values obtained from Monte Carlo calculations are listed here:

Quantity	Value
ϵ_{uds}	0.7%
ϵ_c	3.0%
c_b	0.97

Any efficiency correlation between the two hemispheres of quarks lighter than the b quark can be safely neglected ($c_c = c_{uds} = 1$) because the corresponding efficiencies

---

[1]In practice all quantities have been calculated for different discriminant cut values in the relevant interval $D_{cut} \in [1, 4]$. For clarity reasons, the following numbers are given for $D_{cut} = 2.3$. The motivation for this value will be given later.

are very small ($\epsilon_c = 3.0\%$, $\epsilon_{uds} = 0.7\%$). The background efficiencies ϵ_{uds} and ϵ_c are shown in figure 7.1 as a function of the hemisphere discriminant cut value. The input numbers measured from data are:

Quantity	Value
N_{had}	968964
N_t	118817
N_{tt}	11705

With all input values the equation system can be solved resulting in the following numbers for ϵ_b and R_b:

$$R_b = 0.2178$$
$$\epsilon_b = 23.70\%$$

In figure 7.2 the b tagging efficiency for data and Monte Carlo and the purity of the Monte Carlo sample as a function of the discriminant cut is shown. The agreement of the b tagging efficiency between Monte Carlo and data is very good. The residual relative difference between the efficiency observed in data with respect to the Monte Carlo over the whole interval never exceeds 2.3%.

7.1   Error Discussion

The total error on R_b is calculated from all errors of the coefficients in the equations 6.11 and 6.14. In order to get the contributions to R_b of these input parameters, they are propagated through the equation. The total error is built by adding these values in quadrature. Error contributions are considered separately for systematic and statistical error sources.

The statistical error of the input values are given by the standard deviation of the binomial distribution. This can be done because the efficiencies, correlations and numbers of (co-)tagged hemispheres are based on 'true' or 'false' decisions on a sample of known number of events (N). For the number of selected events, N_{sel}, out of a sample of known number N the statistical deviation is consequently given by:
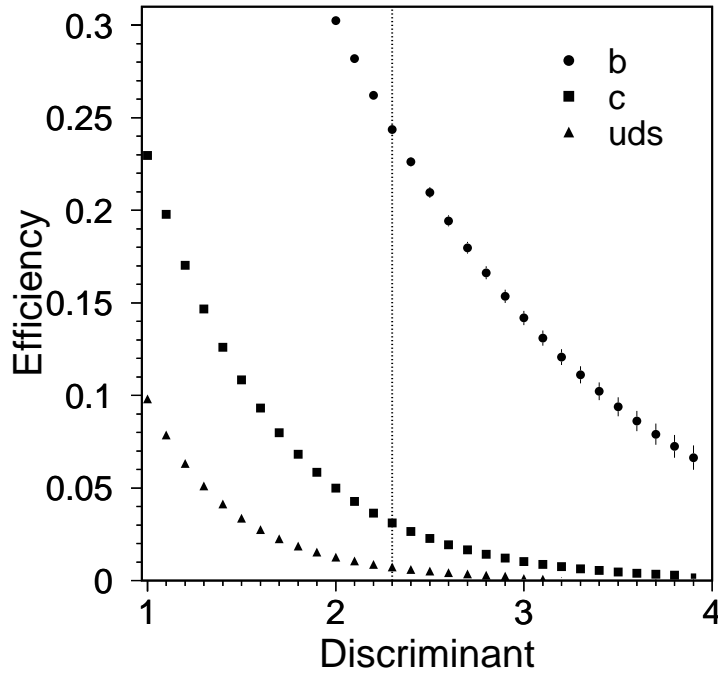
Figure 7.1: The background efficiencies of c and uds quarks passing the b tag estimated from Monte Carlo. In comparison, the selection efficiency of b quarks is also presented. The dashed line indicates the hemisphere discriminant cut value finally used.

$$\Delta N_{sel} = \sqrt{N\epsilon(1-\epsilon)}\,, \qquad (7.1)$$

whereas ϵ is the probability that an event can be selected. This probability is called selection efficiency. Thus the statistical error of a selection efficiency taken from Monte Carlo can be calculated by:

$$\Delta\epsilon = \sqrt{\epsilon(1-\epsilon)/N^{MC}}\,. \qquad (7.2)$$

The investigation of the systematic errors is more complex. They result from imperfections of the Monte Carlo simulation, either from underlying physics input to the event generation or from aspects of the detector simulation. In the following sections the procedure of estimating the contributions to the final systematic error will be described. The following sources of systematic errors are considered:
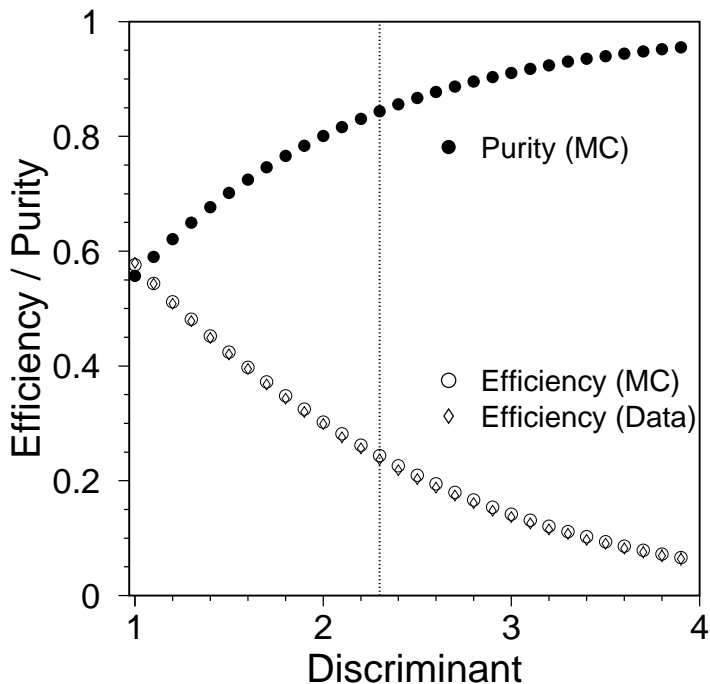
Figure 7.2: The efficiency and the purity of the b tag taken from the Monte Carlo sample and the b tag efficiency obtained from data.

- tracking resolution,

- systematics from background modelling,

- systematics from hemisphere correlations,

- finite Monte Carlo statistics.

7.2 Tracking Resolution

The tracking resolution function - deduced from the distribution of negative impact parameter significance - is obtained from data. The uncertainty caused by statistics is negligible. But a wrong description of the resolution function in the Monte Carlo sample may influence the values taken from the Monte Carlo and hence the measurement. In order to estimate the systematic error from tracking resolution, two Monte Carlo samples are used; one with final adjustment and the other one

corresponding to an 1σ uncertainty in the resolution function. The Monte Carlo with final adjustment is found to produce a stable value of R_b as a function of the discriminant within statistical fluctuations and systematic errors. The magnitude of the residual discrepancy in the reference Monte Carlo sample is defined by the resulting inconsistency with a constant value by one standard deviation. The differences in ϵ_c, ϵ_{uds}, and c_b predicted by these two Monte Carlo samples are propagated as an estimate of the tracking resolution uncertainty.

7.3 Systematic Error from Background Modelling

By selecting a hemisphere to be originated from a primary b quark using lifetime information, there is a certain possibility to tag those event hemispheres in which a long-lived particle other than a B hadron is produced. Since the background efficiencies ϵ_{uds}, ϵ_c, and the hemisphere efficiency correlation factor c_b are determined externally from Monte Carlo, uncertainties in the modelling of production and decay of quarks have to be taken into account.

The propagation of the uncertainties is done by calculation reweighting functions which parameterise the standard deviation of the different error sources and can be used to modify the existing Monte Carlo sample. The variation of the auxiliary parameter is taken as error.

The largest background fraction of particles passing the b tag results from the decay $Z \to c\bar{c}$. Lifetimes from charm hadrons like D^0, D^+, D_s, and Λ_c vary between 0.2 and 1.1 ps. Other hadronic events could contain strange mesons or baryons (K^0, Λ) with relatively long lifetime, which contribute to uncertainties in ϵ_{uds}. All these particles decay after travelling some distance from their production point and hence will produce tracks with significant lifetime information. Typical average decay length at LEP are one millimeter for charm hadrons and a few centimeters in case of K^0 and hyperons. The fragmentation function was tuned according to the measured rate of strange longlived baryons. As an estimate of the error a variation of 10% around their central value is used.

A further possibility identifying b quarks not originating from the process $Z \to b\bar{b}$ is the *gluon splitting*, where radiated gluons, *e.g.* from $Z \to u\bar{u}$, produce $c\bar{c}$ or $b\bar{b}$ pairs. Uncertainties in the b and c fragmentation are estimated by varying

Error source	Variation
Beauty fragmentation parameter: $\langle \mathrm{x_E}(\mathrm{b}) \rangle$	0.702 ± 0.008 [46]
Beauty decay parameters: B lifetimes	1.576 ± 0.016 ps [52]
B decay multiplicity	4.955 ± 0.062 [52]
Fractions in $c\bar{c}$ events: D^+	0.233 ± 0.027 [52]
D_s	0.103 ± 0.029 [52]
Λ_c	0.063 ± 0.028 [52]
$g \rightarrow c\bar{c}$ in $c\bar{c}$ events	$(2.38 \pm 0.48)\%$ [46]
$g \rightarrow b\bar{b}$ in $c\bar{c}$ events	$(0.13 \pm 0.04) \times g \rightarrow c\bar{c}$ [46]
Charm decay parameters: D^0 lifetime	0.415 ± 0.004 ps [27]
D^+ lifetime	1.057 ± 0.015 ps [27]
D_s lifetime	0.467 ± 0.017 ps [27]
Λ_c lifetime	0.206 ± 0.012 ps [27]
D decay multiplicity	2.53 ± 0.06 [46]
$BR(D \rightarrow K_s^0 \text{anything})$	0.46 ± 0.06 [48]
Charm fragmentation parameter: $\langle \mathrm{x_E}(\mathrm{c}) \rangle$	0.484 ± 0.008 [46]
Fractions in uds events: K^0 and Λ	JETSET $\pm 10\%$ (see text)
$g \rightarrow c\bar{c}$ in uds events	$(2.38 \pm 0.48)\%$ [46]
$g \rightarrow b\bar{b}$ in uds events	$(0.13 \pm 0.04) \times g \rightarrow c\bar{c}$ [46]

Table 7.1: Variation of modelling parameters used for the determination of the systematic error in the impact parameter double-tag measurement.

the Peterson fragmentation function [91]. This is done using the fraction of beam energy carried by the b or c hadron, $\langle x_E(b) \rangle$ and $\langle x_E(c) \rangle$.

Modelling uncertainties in the B hadron production only influence the correlation parameter c_b. Beside the B energy fraction, the charged decay multiplicity and the average lifetime of B hadrons were varied.

All parameters relevant to the R_b analysis are summarised in table 7.1 . The parameters and their variation follows a recommendation of the LEP Electroweak Working Group [46] and updated measurements.

By propagating the large b physics uncertainties to ϵ_b estimated from Monte Carlo, it results in $\epsilon_b^{MC} = (24.18 \pm 0.03(\text{stat}) \pm 1.53(\text{syst}))\%$. Here, the advantage of the double-tag method becomes clear. The large systematic error has no effect on R_b because ϵ_b from Monte Carlo is not used.

uds Efficiency

Model uncertainties in ϵ_{uds} arise from:

- the residual contamination by light hadrons with long lifetimes (K^0 and hyperons) and

- the probability for gluon splitting into $b\bar{b}$ and $c\bar{c}$ pairs.

The error sources and the resulting total error of the uds efficiency are listed in table 7.2. All values are calculated for a hemisphere discriminant cut of $D_{cut} = 2.3$.

c Efficiency

Model uncertainties contributing to the error of ϵ_c arise from:

- the lifetimes of charm hadrons,

- its relative branching ratios,

- the decay multiplicity of D mesons,

- the K_s^0 multiplicity in c decays,

Error source	$\Delta\epsilon_{uds}$
Monte Carlo Statistics	0.004%
Track Resolution	0.009%
K^0 and Λ	0.033%
$g \to c\bar{c}$	0.003%
$\frac{g \to b\bar{b}}{g \to c\bar{c}}$	0.003%
Total	0.035%

Error source	$\Delta\epsilon_{c}$
Monte Carlo Statistics	0.02%
Track Resolution	0.02%
D^0 lifetime	0.02%
D^+ lifetime	0.01%
D_s lifetime	0.01%
Λ_c lifetime	0.01%
D^+ fraction	0.10%
D_s fraction	0.02%
Λ_c fraction	0.04%
D decay multiplicity	0.06%
$BR(D \to K_s^0 anything)$	0.02%
$\langle x_E(c) \rangle$	0.06%
$g \to c\bar{c}$	0.00%
$\frac{g \to b\bar{b}}{g \to c\bar{c}}$	0.00%
Total	0.14%

Table 7.2: Error contributions to ϵ_{uds} and ϵ_c for a cut of $D_{cut} = 2.3$.

- the fragmentation function,

- gluon splitting.

All contributions to the error of ϵ_c are listed in table 7.2 for a hemisphere discriminant cut of $D_{cut} = 2.3$.

Hemisphere Correlation c_b

The accuracy of the R_b measurement depends largely on the understanding of the hemisphere efficiency correlation. Due to the high b purity the correlation factors c_c and c_{uds} can be safely neglected. The effect on R_b varying the background correlation factors, c_c=c_{uds}= 1, within reasonable limits ($\pm 1\%$) is negligible.

Error source	Δc_b
Monte Carlo Statistics	0.0036
Track Resolution	0.0002
Vertex bias	0.0050
θ correlations	0.0002
ϕ correlations	0.0009
Hard gluon emission	0.0004
B decay multiplicity	0.0009
B lifetimes	0.0004
B fragmentation	0.0016
Total	0.0065

Table 7.3: Error contributions to c_b for a cut at $D_{cut} = 2.3$.

No corresponding error estimate involving them is carried out. The remaining model uncertainties in calculating c_b from the Monte Carlo are:

- the B meson decay multiplicity,

- the B meson lifetime,

- the b fragmentation.

All contributions to the total error of c_b are listed in table 7.3.

7.4   Results

Figure 7.3 shows the statistical and systematic errors on R_b as a function of the hemisphere discriminant cut. Minimising the overall error (systematic and statistical added in quadrature), $D_{cut} = 2.3$ is chosen to be the central cut value of the measurement. The corresponding purity of b events is 84%. The value of ϵ_c is estimated by the Monte Carlo to be $\epsilon_c = (3.05 \pm 0.02(\text{stat}) \pm 0.15(\text{syst}))\%$. A breakdown of the errors is shown in table 7.2. Since the individual charm lifetimes are measured very accurately, the fractions of the different species become one of the major error contributions. Among all charm hadrons D^+ dominates the errors due to its long lifetime. The value of ϵ_{uds} is estimated to be $\epsilon_{uds} = (0.738 \pm 0.004(\text{stat}) \pm 0.035(\text{syst}))\%$. The different error sources are shown in table 7.2. The systematic error is dominated by the uncertainty in the rate of light flavoured hadrons with long lifetime. The correlation coefficient is $c_b = 0.9729 \pm 0.0048(\text{stat}) \pm 0.0067(\text{syst})$. The different error sources are listed in table 7.3. Primary vertex effects are the dominant source of uncertainty.

Using all these information the measured value of R_b^0 is:

$$R_b^0 = 0.2178 \pm 0.0018(\text{stat}) \pm 0.0031(\text{syst}) - 0.196(R_c - 0.172)$$

The corresponding b quark tagging efficiency is:

$$\epsilon_b = (23.70 \pm 0.19(\text{stat}) \pm 0.22(\text{syst}))\%$$

The dependence of R_b on the discriminant cut value is shown in figure 7.4. No significant dependence from the cut value can be seen. The deviation of R_c from the Standard Model prediction of 0.172 has been left explicitly in the calculations,

since there is some uncertainty in the accuracy of its experimental determination. The full breakdown of the final systematic errors is given in table 7.4.

Error source	ΔR_b
Monte Carlo statistics	0.00092
Resolution	0.00055
Reconstruction effects on c_b	0.00120
D^+ fraction	0.00133
D_s fraction	0.00021
Λ_c fraction	0.00047
D^+ lifetime	0.00020
D^0 lifetime	0.00013
D_s lifetime	0.00012
Λ_c lifetime	0.00008
D decay multiplicity	0.00074
$BR(D \rightarrow K_s^0 anything)$	0.00025
$\langle x_E(c) \rangle$	0.00084
$g \rightarrow c\bar{c}$ in $c\bar{c}$ events	0.00001
$\frac{g \rightarrow b\bar{b}}{g \rightarrow c\bar{c}}$ in $c\bar{c}$ events	0.00003
K_s^0 and Λ	0.00176
$g \rightarrow c\bar{c}$ in uds events	0.00017
$\frac{g \rightarrow b\bar{b}}{g \rightarrow c\bar{c}}$ in uds events	0.00014
B fragmentation $\langle x_E(b) \rangle$	0.00040
B lifetimes	0.00011
B decay multiplicity	0.00024
Hard gluon fragmentation	0.00010
Total	0.00307

Table 7.4: Internal and external error contributions to R_b for a cut at $D_{cut} = 2.3$. The errors from the D fractions are propagated according to the correlation matrix defined in [92].
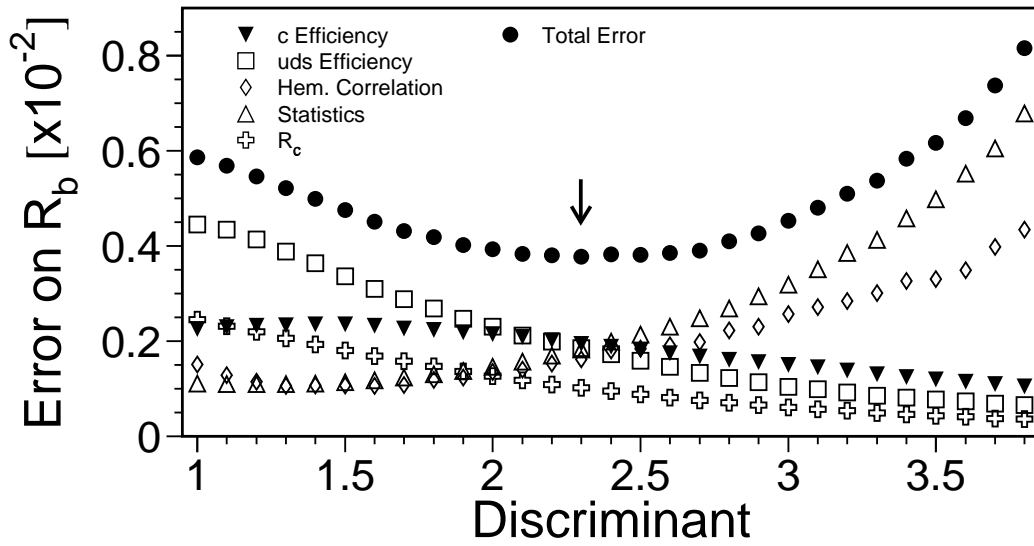
Figure 7.3: Distribution of the error contributions as a function of the discriminant cut. In order to determine the discriminant cut value which gives the smallest error, the distribution of the total error is also shown. The arrow indicates the discriminant cut chosen for this analysis.
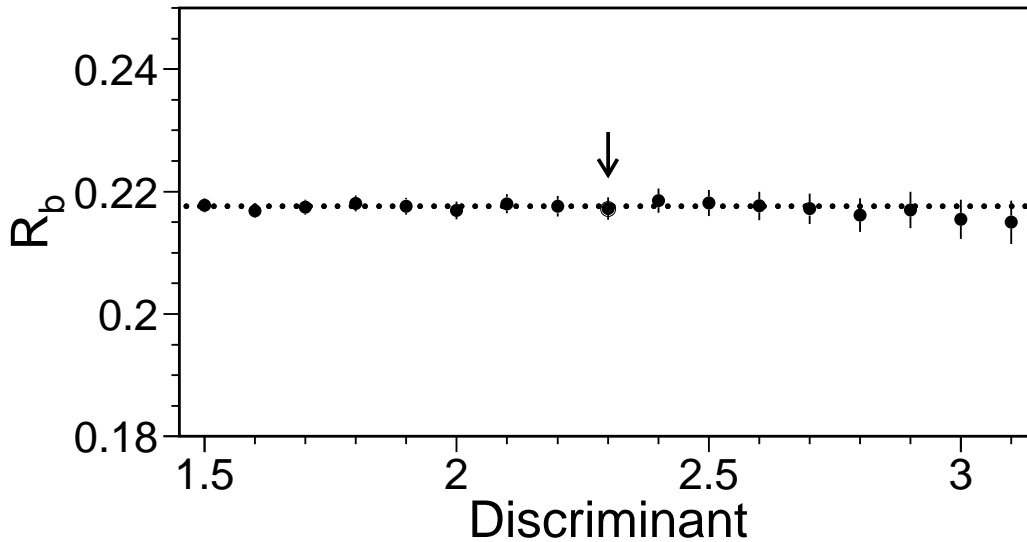
Figure 7.4: Distribution of R_b as a function of the hemisphere discriminant cut. The deviation of R_b from a constant is within the statistical fluctuation. The arrow shows the discriminant cut chosen for this analysis.

The precision of the measurement of R_b relies on an excellent vertex detector. The precise reconstruction of the primary vertex provides the quality of the measurement. Additional information such as the precisely measured secondary vertex or the capability to determine the invariant jet mass can greatly improve the b tagging efficiency by reducing the background simultaneously. The experiments have made great efforts to improve the details of their vertex tracking system. For example, DELPHI and ALEPH have upgraded their silicon detectors.
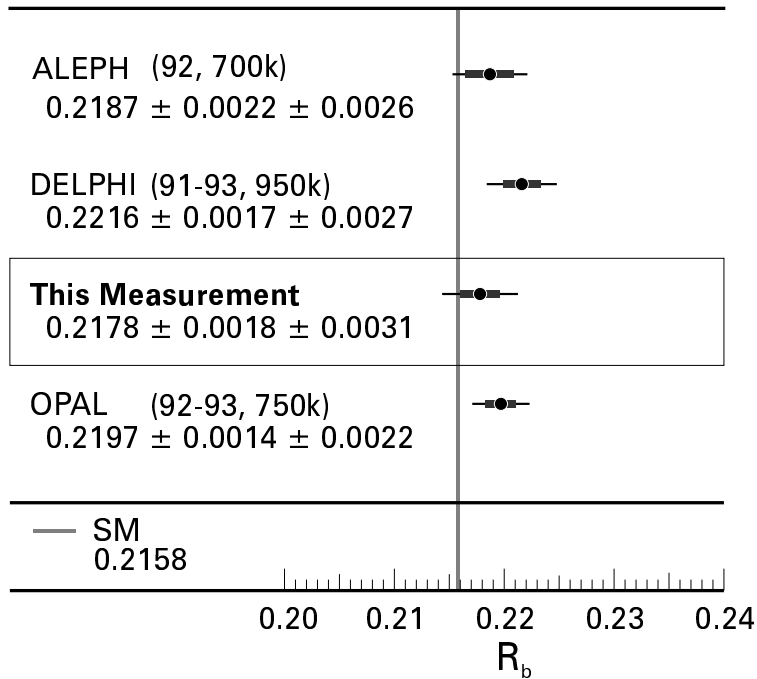
Figure 7.5: Comparison of the R_b measurement presented in this thesis with the results of the other LEP experiments which are based on the same tagging technique. The amount of data used by each experiment is given in brackets. The results are compatible[3] with each other and the uncertainties are similar. In addition the Standard Model expectation is given.

In order to compare this measurement directly with those from other LEP experiments results were taken which are based on the same tagging method. Figure 7.5 shows the results of the four LEP experiments using a lifetime tag. Since the silicon vertex detector of L3 was fully operational from 1994 onwards, the analy-

sis presented here is limited to the data of 1994-1995. Therefore, the results are comparable in terms of the operation time and hence in terms of statistics. The measurements are compatible with each other and have similar uncertainties.

Figure 7.6 shows the latest results of all experiments as of end of 1998 [93] and the result of an electroweak fit including these measurements. The value for L3 is the result of a combination of the measurement described here with an analysis using a high-$p_\perp$ lepton tag. The procedure of combining both measurements is described in [9].
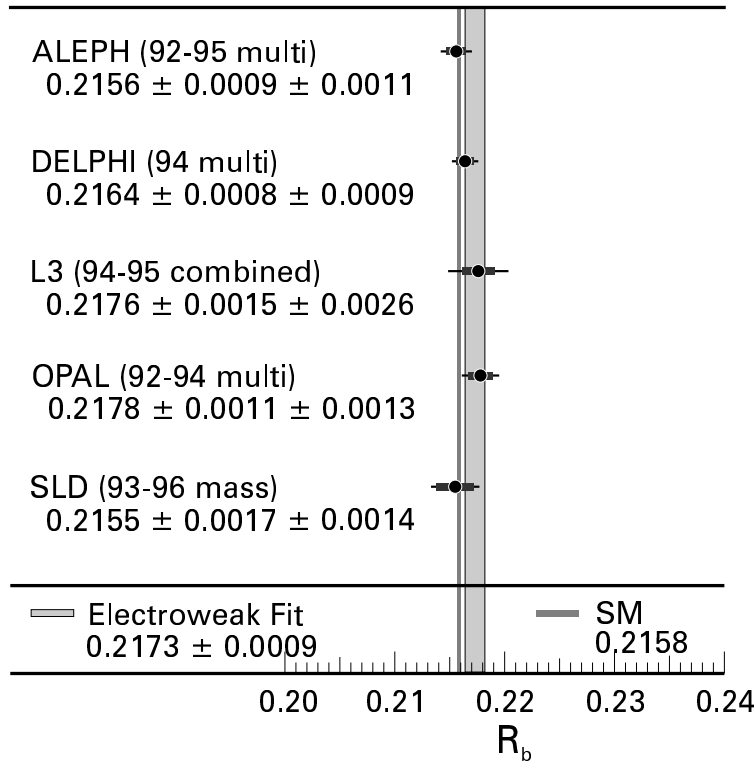
Figure 7.6: Latest results of R_b measurements from LEP and SLD. The right band depicts the result of a global electroweak fit including these measurements. The Standard Model expectation is given by the left band.

The precision of the world average $R_b = 0.2173 \pm 0.0009$ is 0.4% (414 ppm) and denotes an improvement in the world average in summer 1995 (720 ppm) of almost a factor of two. In comparison, the mass of the Z boson has been measured at LEP with a precision of 77 ppm, $\alpha_s(m_Z)$ is known with a precision of 17000 ppm [27].

Chapter 8

Interpretation and Conclusion

The couplings of fermions to the Z boson are of great importance in establishing the validity of the Standard Model and investigating physics effects beyond it.

The vector and axial-vector couplings enter in the equation for R_b as quadratic sum $(g_V^b)^2 + (g_A^b)^2$. Using a second observable, $A_{FB}^{0,b}$, here the couplings enter as ratio g_V^b/g_A^b, it is possible to calculate the effective couplings separately. Figure 8.1 illustrates the mathematical relation of R_b and $A_{FB}^{0,b}$ in the g_V^b-g_A^b plane. The solution in the g_V^b-g_A^b plane can be described by a crossing point of a circle[1] with a radius which is proportional to $(R_b^0)^2$ and a straight line with a slope given by $A_{FB}^{0,b}$. Since the couplings enter symmetrically into the equations of $A_{FB}^{0,b}$ and R_b^0, the values of vector and axial-vector couplings cannot be distinguished. Furthermore, the absolute sign of the couplings in not defined. This leads to a fourfold ambiguity, depicted by figure 8.2. It can be resolved, e.g., by including data far below the Z resonance. The asymmetry there is dominated by the γ-Z interference term, proportional to $Q_e g_A^e Q_b g_A^b$. Thus, the sign of the axial-vector coupling of the b quark is determined with respect to reference definition of the electron. Taking the result from an analysis which includes data from PETRA, PEP and KEK [94] as constraint, the ambiguity can be resolved (see figure 8.2). In order to extract the couplings an electroweak fit to seven parameters as shown in table 8.1 have been applied. This fit was done using the MINUIT program [95] which is based on the

---

[1]There are small corrections which slightly modify the circle. These corrections were taken into account but are not seen within the precision of the figures.

minimisation of the chi-square:

$$\chi^2 = \begin{pmatrix} \chi_1 & \cdots & \chi_n \end{pmatrix} \begin{pmatrix} C_{11} & \cdots & C_{1n} \\ \vdots & \ddots & \vdots \\ C_{n1} & \cdots & C_{nn} \end{pmatrix}^{-1} \begin{pmatrix} \chi_1 \\ \vdots \\ \chi_n \end{pmatrix} \qquad (8.1)$$

$$\text{with:} \quad \chi_i = \frac{(x_i - e_i)}{\delta_i}$$

where x_i are the free parameters being fitted, and δ_i are the uncertainties in the individual measurements e_i.
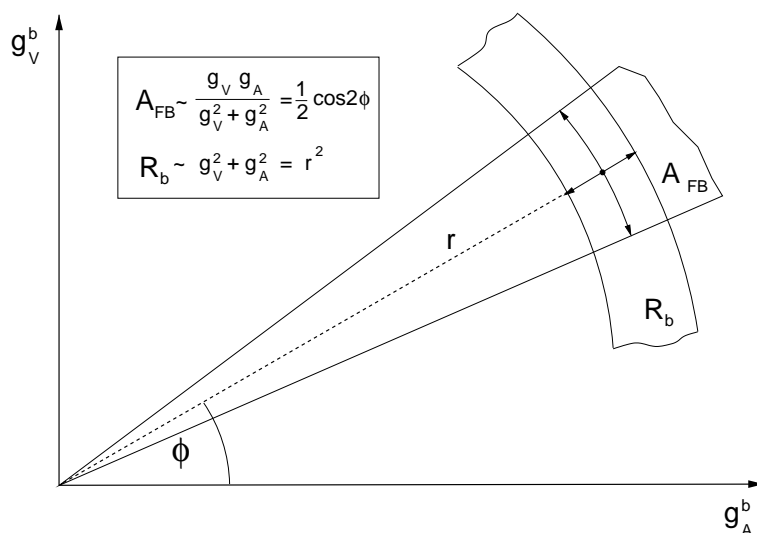
Figure 8.1: Mathematical representation of $A_{FB}^{0,b}$ and R_b in the g_V^b-g_A^b plane.

The matrix elements C_{ij} describe the correlation between the different input parameters. The experimental observables used as input values are the hadronic and leptonic cross-sections and the leptonic forward-backward asymmetries expressed by the five parameters:

$$m_Z, \quad \Gamma_Z, \quad \sigma_{had}^0, \quad R_l, \quad A_{FB}^{0,l}. \qquad (8.2)$$

These parameters are chosen since they are largely uncorrelated experimentally. They are taken from a global fit assuming lepton universality. In addition,

$$R_b^0 \quad \text{and} \quad A_{FB}^{0,b} \qquad (8.3)$$

are taken from measurements. The free parameters of the fit are chosen to be:

$$g_V^b, \quad g_A^b, \quad g_V^l, \quad g_A^l, \quad \Gamma_{\text{had}}, \quad \Gamma_Z, \quad m_Z. \tag{8.4}$$

The relations between the input values and the free parameters of the fit are given explicitly in section 3. R_l is defined by $R_l = \frac{\Gamma_{\text{had}}}{\Gamma_l}$. The L3 input values are listed in table 8.1.

Parameter	Value
m_Z (GeV)	91.1883 ± 0.0029 [96]
Γ_Z (GeV)	2.4996 ± 0.0043 [96]
σ_{had}^0 (nb)	41.411 ± 0.074 [96]
R_l	20.788 ± 0.066 [96]
$A_{FB}^{0,l}$	0.0187 ± 0.0026 [96]
$A_{FB}^{0,b}$	0.1015 ± 0.0073 [97]
R_b	0.2178 ± 0.0030

Table 8.1: Input values for the fit to L3 data.

The result of the fit to L3 data in the g_V^b-g_A^b plane is shown in figure 8.2 as contours. The two contours in the lower left quarter correspond to a confidence level of the fit of 68%. In the upper right zone the equivalent contour of 95% is given. The window marked by the rectangle defines the region of interest shown in the next figures. The Standard Model prediction corresponds to a top mass of $m_{\text{top}} = 175$ GeV and a fixed Higgs mass of $m_H = 300$ GeV. Figure 8.3 shows the g_V^b-g_A^b contour of a 68% confidence level and the constraints from the individual measurements for L3 data and combined results from LEP and SLD. The input values taken for the fit to LEP and SLD results are given in table 8.3.

The fit to L3 data results in the following solution for g_V^b and g_A^b:

$$g_V^b = -0.2984^{+0.0381}_{-0.0562} \tag{8.5}$$
$$g_A^b = -0.5275^{+0.0356}_{-0.0200}$$

The final correlations of the fitted parameters are listed in table 8.2. It can be seen that the vector and axial-vector couplings of the b quark are strongly anti-
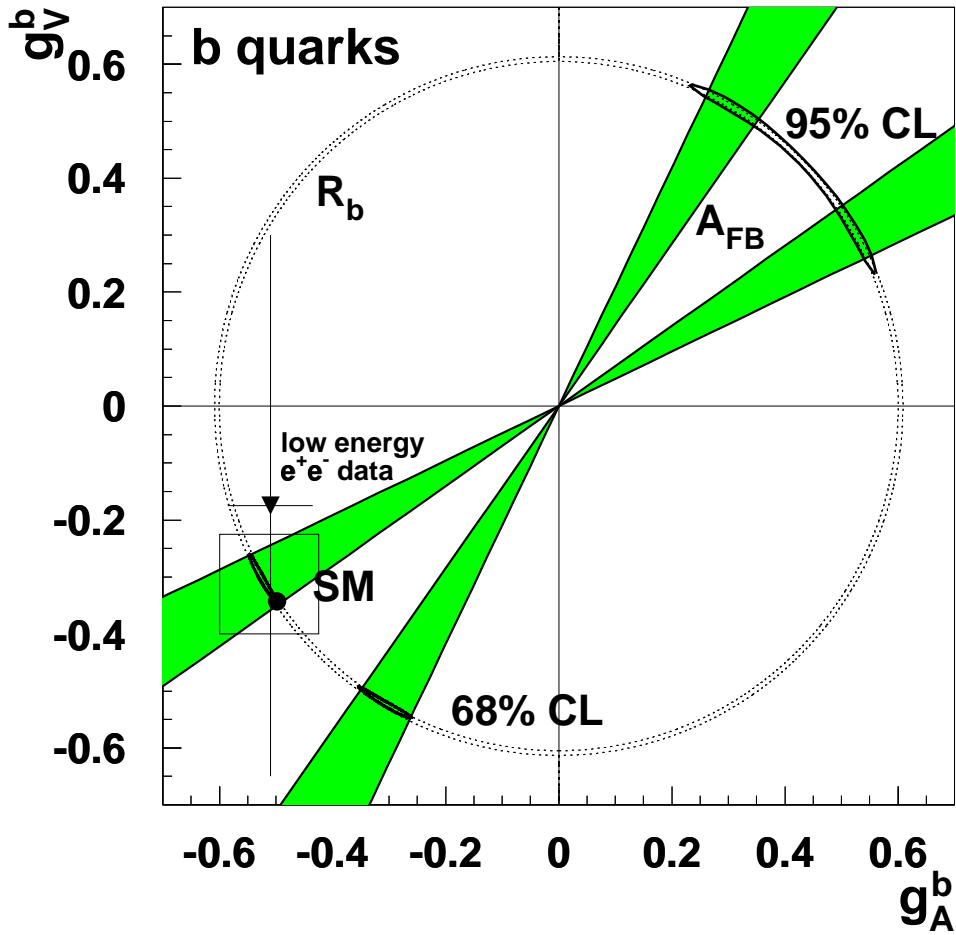
Figure 8.2: The figure shows the four possible solutions for the vector and axial-vector couplings taking the values of R_b^0 and $A_{FB}^{0,b}$ measured by the L3 experiment. The value of $A_{FB}^{0,b}$ is represented by two straight lines in the g_V^b-g_A^b plane. The shadowed areas correspond to the 1σ error regions. The circle is given by the value of R_b. The two lines include the 1σ error contribution. The contours in the crossing areas are results from a global fit to L3 data using the ZFITTER program. The 95% confidence level contour is shown in the upper right quarter and the results with 68% confidence level in the lower left one. The point inside the rectangle represents the Standard Model prediction. The value given by a combination of low energy e^+e^- data far below the Z resonance allows to solve the ambiguity. The rectangle is the region of interest shown in the next figures.

correlated.

	g_V^b	g_A^b	g_V^l	g_A^l	m_Z	Γ_Z	Γ_{had}
g_V^b	1	-0.992	0.219	-0.802	0.048	-0.008	-0.007
g_A^b		1	-0.196	0.799	-0.047	-0.022	-0.038
g_V^l			1	-0.246	0.009	-0.675	-0.489
g_A^l				1	-0.060	-0.015	-0.017
m_Z					1	0.050	0.039
Γ_Z						1	0.65
Γ_{had}							1

Table 8.2: Correlations between the free parameters given by the fit to L3 data.

Parameter	Value
m_Z (GeV)	91.1867 ± 0.0021 [96]
Γ_Z (GeV)	2.4939 ± 0.0024 [96]
σ_{had}^0 (nb)	41.491 ± 0.058 [96]
R_l	20.765 ± 0.026 [96]
$A_{FB}^{0,l}$	0.01683 ± 0.00096 [96]
$A_{FB}^{0,b}$	0.0990 ± 0.0021 [96]
R_b	0.21656 ± 0.00074 [96]

Table 8.3: Input values for the fit to combined data from LEP and SLD.

From a fit to combined results of LEP and SLD (the input values are listed in table 8.3) the vector and axial-vector couplings has been extracted to be:

$$
\begin{aligned}
g_V^b &= -0.3100^{+0.0159}_{-0.0189} \\
g_A^b &= -0.5182^{+0.0116}_{-0.0092}
\end{aligned}
\tag{8.6}
$$
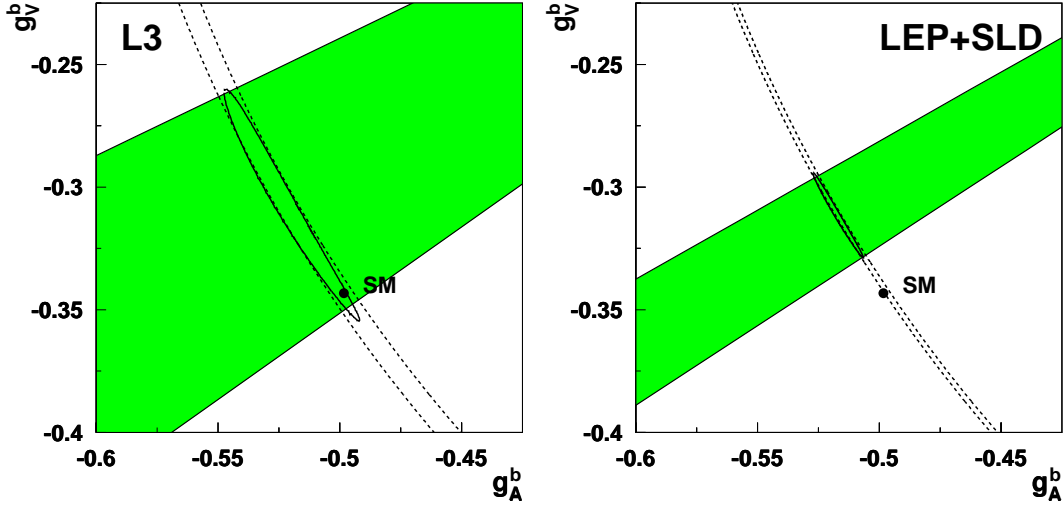
Figure 8.3: The 68% CL contour in the g_V^b-g_A^b plane for a 7-parameter fit to L3 data and on combined results from LEP and SLD. The 1σ regions given by R_b^0 and $A_{FB}^{0,b}$ are also shown.

The weak neutral couplings can also be expressed in terms of the left-handed $((g_V^b + g_A^b)/2)$ and right-handed $((g_V^b - g_A^b)/2)$ couplings. The Standard Model predicts the parity violation of the electroweak interaction and hence different contribution to g_L^b and g_R^b. In case of 100% parity violating couplings $(g_V^b = g_A^b)$ the right-handed coupling would be equal zero, whereas the left-handed coupling would reach its maximum value. From a fit to L3 data the left-handed and right-handed couplings can be extracted to be::

$$g_L^b = -0.4140^{+0.0094}_{-0.0102} \tag{8.7}$$
$$g_R^b = +0.1149^{+0.0290}_{-0.0461}$$

The corresponding results of the fit to LEP and SLD data are:

$$g_L^b = -0.4152^{+0.0034}_{-0.0035} \tag{8.8}$$
$$g_R^b = +0.1044^{+0.0126}_{-0.0153}$$

The fit results from LEP and SLD combined data and the one from L3 are in agreement. The experimental results of L3 on the neutral current couplings of the b

quark do not provide compelling evidence for physics beyond the Standard Model. In that sense the b quark data are mutually consistent with the Standard Model - the b quark is a representative of the third-generation weak iso-spin doublet. However, the extracted couplings from the fit to LEP and SLD combined data yield a disagreement with the theory. It corresponds to a value of R_b^0 greater than the Standard Model prediction, and a value of $A_{FB}^{0,b}$ less than the in the Standard Model. Figure 8.4 shows the fit results as contours in the g_L^b-g_R^b plane with a confidence level of 68%. Since the result of $A_{FB}^{0,b}$ measure the product of $\mathcal{A}_e$ and $\mathcal{A}_b$, the value of $\mathcal{A}_e$ is used as a reference.
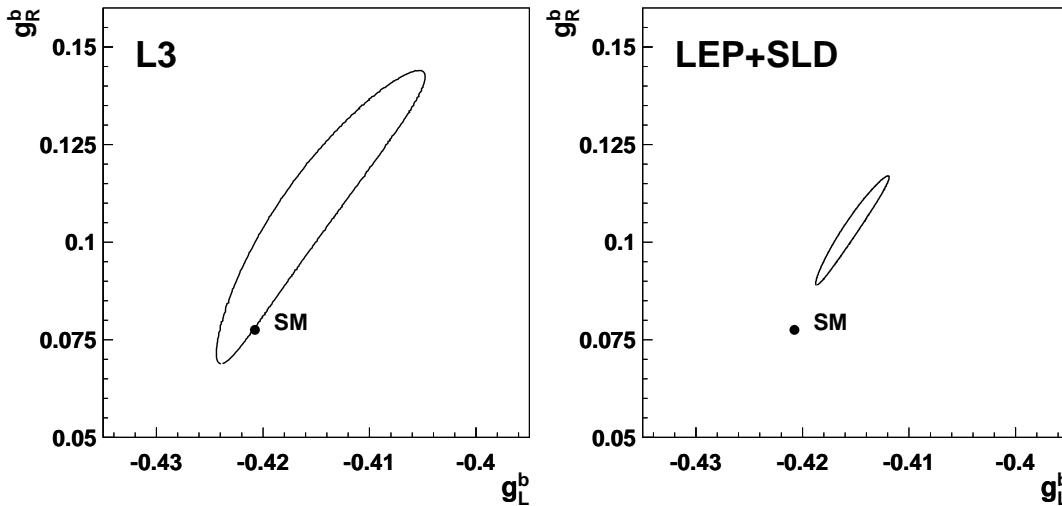
Figure 8.4: The 68% CL contour in the g_L^b-g_R^b plane for a 7-parameter fit to L3 data and to combined results from LEP and SLD.

Since 1995, when the first measurements of R_b resulted in a large disagreement with the Standard Model prediction, great theoretical interest was triggered in the possibility that some aspects of physics beyond the Standard Model might be playing a role. In particular, the MSSM (the minimal supersymmetric extension of the Standard Model) was favoured. Considerable interest centred in the existence of light supersymmetric particles like charginos $\chi^{\pm}$ and scalar top quarks $\tilde{t}_1$. This offered the possibility of removing some apparent discrepancy if the $\chi^{\pm}$

and $\tilde{t}_1$ are light enough to be discovered at LEP-II or at Tevatron. But with today's lower limits of both masses the possible contribution to R_b is of about $\Delta R_b^{SUSY} < 0.0010$ [98]. This is comparable with the actual experimental error of the LEP and SLD combined measurement. None of the popular extensions to the Standard Model could account for these effects. So, it is unlikely that the deviation from the Standard Model arise from new physics contribution to the radiative correction since a correction to κ_Z^b (see equation 3.29 in section 3.4) of about 30% would be necessary to account for the central value of the results.

Alternatively to the equations 3.9 and 3.14 in section 3.2 and 3.3, R_b^0 and $\mathcal{A}_b$ can be expressed in terms of the right-handed and left-handed couplings:

$$R_b^0 \propto (g_L^b)^2 + (g_R^b)^2 , \tag{8.9}$$

$$\mathcal{A}_b = \frac{(g_L^b)^2 - (g_R^b)^2}{(g_L^b)^2 + (g_R^b)^2} . \tag{8.10}$$

This equation is equivalent to:

$$\frac{|g_L^b|}{|g_R^b|} = \sqrt{\frac{1 + \mathcal{A}_b}{1 - \mathcal{A}_b}} . \tag{8.11}$$

Using the LEP and SLD combined fit results, the ratio of the left-handed and right-handed couplings can be calculated to be $|g_L^b|/|g_R^b| = 3.98 \pm 0.53$. This is compatible with the ratio, calculated directly with $\mathcal{A}_b = 0.877 \pm 0.023$ [27], which is 2.5σ below the Standard Model. For the ratio of the couplings the Standard Model predicts $|g_L^b|/|g_R^b| = 5.46$. Together with the measurement of R_b^0 which yield a value about 1σ high compared to the Standard Model, this suggest that the right-handed coupling is higher than expected.

The only possible explanation would be an extension, which couples on the tree level and influences mainly the right-handed coupling of the third generation of quarks. In supersymmetric models with R-parity[2] violation, scalar neutrinos ($\tilde{\nu}$)

---

[2]R-parity is defined as $R_P = (-1)^{2J+3B+L}$, where J, B, and L are spin, baryon number and lepton number, respectively. R_P conservation strongly restricts the phenomology. It implies that superpartners must be produced in pairs and that the lightest supersymmetric particle (LSP) is stable. In the MSSM the R-parity is assumed to be conserved.

may be produced as s-channel resonances in e^+e^- annihilations. Taking data from the high precision scans of the Z lineshape, a sneutrino near the Z mass is not excluded [99]. It would increase R_b^0 and decrease $A_{FB}^{0,b}$. In addition, gauge invariance prohibits to affect the $c\bar{c}$ production, and hence R_c^0 and $A_{FB}^{0,c}$ (which are now in perfect agreement with the Standard Model). It has also been shown in [99] that the t-channel contribution to $\mathcal{A}_e$ is negligible. By allowing such sneutrino resonance, the chi-square in a combined fit to lineshape data of the Z and heavy flavour electroweak observables could be improved from $\chi^2/\text{d.o.f} = 60.6/54$ to around $\chi^2/\text{d.o.f} = 54/51$ [99]. Except the hadronic cross-section, which is reduced by 2/3 of the standard deviation, the extracted fit parameters are in agreement with the Standard Model predictions. The improvement in the fit probability is mainly due to R_b ($\chi^2/\text{d.o.f}$ reduced from 4.5 to 0.1) and $\mathcal{A}_b$, yielding a $\chi^2/\text{d.o.f}$ of 1.4 instead of 2.6 without assuming a sneutrino resonance. Thus, an improvement in the sector of weak neutral b quark couplings can be obtained without changing the other electroweak parameter.

It has to be pointed out that there are complications in the definition of electroweak effective couplings for quarks. These effective couplings absorb not only the electroweak effects but also underlying QCD corrections and running mass effects. Top mass dependent effects are contained in both electroweak and QCD corrections. Thus a clean separation of electroweak and QCD corrections in the effective couplings depending on m_{top} and m_H and QCD correction factors depending on α_s is not possible beyond one-loop order. For the results presented here, the factorisation as implemented in the ZFITTER framework is used as an example.

Appendix A

Overview about HEP
Experiments and Laboratories

In this thesis many names of high energy physics laboratories and corresponding high energy physics experiments are used. An overview of actual and past experiments and the laboratories where they are located is given.

BNL - Brookhaven National Laboratory

Location: Long Island, New York, USA.

Accelerators and Experiments:

- **AGS** - Alternating Gradient Synchrotron. Here the J particle was discovered in 1974 and led to a Nobel price together with the collaboration which found the Ψ at the SPEAR storage ring. The particle is today known as J/Ψ.

CERN - European Laboratory for Particle Physics

Location: near Geneva along the border of France and Switzerland.

Accelerators and Experiments:

- **PS** - The Proton Synchrotron is the oldest and most versatile of CERN's accelerators. The PS was commissioned in 1959 and has been running continuously ever since. With a diameter of 200 meters and reaching a final

energy of 28 GeV, it was for a while the most powerful accelerator in the world. Today the PS is working as preaccelerator, *e.g.*, for LEP.

- **SPS** - The Super Proton Synchrotron is a circular accelerator, 6 km in circumference, buried underground. It was built originally to accelerate protons - and still does so - but it has since operated as a proton-antiproton collider, a heavy-ion accelerator, and an electron/positron injector for LEP. As a proton-antiproton collider in the 1980s, it provided CERN with one of its greatest moments - the first observations of the W and Z particles, the carriers of the weak force.

- **LEP** - Large Electron Positron Collider was built to study electroweak interaction at centre of mass energies of up to about 200 GeV. The four experiments ALEPH, DELPHI, L3, and OPAL are investigating electron-positron annihilations. Extremely accurate measurements of the Z particle properties show that the fundamental building blocks of matter consist of only three families of particles. Today LEP is running at an energy region which allows the production of W pairs. The investigation of the properties of the charged gauge boson and the search for the Higgs boson and new phenomena are the physics goals of today.

- **LHC** - with the Large Hadron Collider it is planned to bring protons into head-on collisions up to an energy of about 14 TeV using the LEP tunnel. With this collider one is probably able to answer fundamental questions left unanswered by LEP, the most important being the mechanism which gives matter its mass.

DESY - Deutsches Elektron-Synchrotron

Location: Hamburg, Germany.

Accelerators and Experiments:

- **DORIS** - electron-positron storage ring with a maximum centre of mass energy of 11.2 GeV. DORIS stops operation in 1992. The experiments ARGUS (1982 - 1992) and Crystal Ball (1982-1986) have taken data at the $\Upsilon(4S)$

Machine	Dates	Energy(GeV)	Major experiments
SPEAR (SLAC)	1972-1990	8	Crystal Ball, DELCO MARK I,II,III
DORIS (DESY)	1973-1992	11.2	ARGUS, Crystal Ball, DASP, PLUTO
CESR (Cornell)	1979-	12	CLEO, CUSB
PETRA (DESY)	1978-1986	46.8	CELLO, JADE, MARK J, PLUTO, TASSO
PEP (SLAC)	1980-1990	30	DELCO, HRS, MAC, MARK II, TPC
TRISTAN (KEK)	1987-1995	64	AMY, TOPAZ, VENUS
SLC (SLAC)	1989-	100	MARK II, SLD
LEP (CERN)	1989-	192	ALEPH, DELPHI, L3, OPAL
PEPII (SLAC)	1999-	9/3.1	BaBar
KEKB (KEK)	1999-	8/3.5	BELLE

Table A.1: The major high-energy e^+e^- colliders. The energy refers to the maximum centre of mass energy except for the asymmetric b-factories where the two beam energies are given.

resonance. 1987 the mixing of the $B\bar{B}$-system was discovered by ARGUS. Today the DORIS ring is used as synchrotron radiation source with an electron/positron beam energy of 4.5 GeV (DORISIII).

- **PETRA** - electron-positron storage ring with a maximum centre of mass energy of about 46.8 GeV. PETRA was operating from 1978 - 1986 for high energy physics experiments like CELLO, JADE, MARK J, PLUTO and TASSO. 1979 the gluon was discovered here. Today PETRA is used as synchrotron radiation source with an electron/positron beam energy of 4.5 GeV and as preaccelerator with a beam energy of 40 GeV (protons) or 4.5 GeV (electrons/positrons).

- **HERA** - electron-proton collider with an electron beam energy of 27.5 GeV and a proton beam energy of 920 GeV. There are 3 experiments actually running: H1 and ZEUS, collider experiments measuring the proton structure function and HERMES a gas target experiment using the longitudinally polarised electron beam to measure the spin structure function of nucleons. The experiment HERA-B is proposed to investigate the CP-violation in a B meson system using an internal wire target and is under construction.

FNAL - Fermi National Accelerator Laboratory (Fermilab)

Location: Batavia, Illinois, USA

Accelerators and Experiments:

- **Tevatron** - proton-antiproton collider with a centre-of-mass energy of up to 2 TeV. Both experiments D0 and CDF are hosted here. The first direct evidence for the top quark (the up-type quark of the third generation) was given in 1994/1995 by both experiments.

KEK - High Energy Accelerator Research Organisation
Location: Tsukuba, Japan.

Accelerators and Experiments:

- **TRISTAN** - electron-positron collider with a centre-of-mass energy of about 64 GeV which ends operation in 1995. Three experiments (AMY, TOPAZ, and VENUS) were analysing data from this collider.

- **KEKB** - asymmetric B factory for the BELLE experiment which is built to investigate the CP-violation in the B meson system and will start operation in 1999.

LNS - Laboratory of Nuclear Studies

Location: Cornell University Department of Physics, Ithaca, NY, USA.

Accelerators and Experiments:

- **CESR** - the Cornell Electron-positron Storage Ring with centre-of-mass energies between 9 and 12 GeV. CESR provides electron-positron collision to the CLEOII experiment. CLEOII is an extension of the CLEO experiment which is optimised to study the behaviour of B hadrons on the $\Upsilon(4S)$ resonance. Until 1991 the CUSB experiment takes data at a centre-of-mass energy of 4 to about 8 GeV.

SLAC - Stanford Linear Accelerator Center

Location: Stanford, USA.

Accelerators and Experiments:

- **SPEAR** - electron-positron storage ring with a beam energy of about 4 GeV. Here the Ψ particle (bounding $c\bar{c}$ state) was found in 1974. 1976 the lepton of the third family was discovered. Both measurements won a Nobel price. Today SPEAR is used for synchrotron radiation research.

- **SLC** - the Stanford Linear Collider produces polarised electron and unpolarised positron beams of about 45 GeV each. The SLD Detector makes use of the capabilities of the SLC to perform studies of polarised Z particles produced in collisions between electrons and positrons at the centre of mass energy at the Z resonance.

- **PEPII** - an asymmetric e^+e^- B factory for the BaBar experiment which is optimised to investigate CP-violation.

List of Figures

List of Tables

129

Bibliography

[1] S. L. Glashow, Nucl. Phys. **22** (1961) 579.

[2] A. Salam and J. C. Ward, Phys. Lett. **13** (1964) 168.

[3] S. Weinberg, Phys. Rev. Lett. **19** (1967) 1264.

[4] S. L. Glashow and J. Iliopoulos and L. Maiani, Phys. Rev. **D2** (1970) 1285.

[5] F. Abe and others, Phys. Rev. Lett. **73** (1994) 225–231.

[6] F. Abe and others, Phys. Rev. Lett. **74** (1995) 2626–2631.

[7] S. Abachi and others, Phys. Rev. Lett. **74** (1995) 2632–2637.

[8] The LEP Electroweak Heavy Flavours Working Group and the SLD Heavy Flavour Group, Internal Note LEPHF/95-02 (1995).

[9] J. Alcaraz, B. Bertucci, M. Chamizo, S. Easo, J. Goldstein, D. Kamrad, M. Maity, J. Rodin, Measurement of the Z Branching Fraction into Bottom Quarks Using Double Tag Methods, Internal Report, L3 Note 2114, CERN, 1997.

[10] N. Cabibbo, Phys. Rev. Lett. **10** (1963) 531.

[11] M. Gell-Mann, Phys. Lett. **8** (1964) 214.

[12] G. Zweig, (1664), CERN-TH-412.

[13] M. Kobayashi and T. Maskawa, Prog. Theor. Phys. **49** (1973) 652.

[14] Mary K. Gaillard and Benjamin W. Lee and Jonathan L. Rosner, Rev. Mod. Phys. **47** (1975) 277.

[15] J. J. Aubert and others, Phys. Rev. Lett. **33** (1974) 1404.

[16] J. E. Augustin and others, Phys. Rev. Lett. **33** (1974) 1406–1408.

[17] W. R. Innes and others, Phys. Rev. Lett. **39** (1977) 1240.

[18] W. R. Innes and others, Phys. Rev. Lett. **39** (1977) 1240.

[19] C. Berger and others, Phys. Lett. **76B** (1978) 243.

[20] C. W. Darden and others, Phys. Lett. **76B** (1978) 246.

[21] D. Andrews and others, Phys. Rev. Lett. **44** (1980) 1108.

[22] D. Andrews and others, Phys. Rev. Lett. **45** (1980) 219.

[23] H. Albrecht and others, Phys. Lett. **B192** (1987) 245.

[24] D. Besson and others, Phys. Rev. Lett. **54** (1985) 381.

[25] D. S. Akerib and others, Phys. Rev. Lett. **67** (1991) 1692–1695.

[26] Henning Schröder, Rept. Prog. Phys. **52** (1989) 765.

[27] Review of Particle Physics, Europ. Phys. Journal, C3 (1998) 1.

[28] ed. F. Halzen and A.D. Martin, Quarks & Leptons: An Introductionary Course in Modern Particle Physics, (John Wiley & Sons, Inc., 1984).

[29] The LEP Collabotations, the LEP Electroweak Working Group and the SLD Heavy Flavour Group, A Combination of Preliminary Electroweak Measurements and Constraints on the Standard Model, CERN-PPE/97-154 (1997).

[30] P. W. Higgs, Phys. Lett. **12** (1964) 132.

[31] P. W. Higgs, Phys. Rev. Lett. **13** (1964) 508.

[32] P. W. Higgs, Phys. Rev. **145** (1966) 1156.

[33] M. Kobayashi and T. Maskawa, Prog. Theor. Phys. **49** (1973) 652.

[34] Takaaki Kajita, (1998).

[35] S. Sjöstrand, in Z Physics at LEP 1, Vol.3, ed. G. Altarelli, R. Kleiss and C. Verzegnassi, CERN Report: CERN 89-08 (1989) 143.

[36] T. Hebbeker, Phys. Rept. **217** (1992) 69.

[37] R. D. Field and R. P. Feynman, Nucl. Phys. **B136** (1978) 1, and references therein.

[38] X. Artru and G. Mennessier, Nucl. Phys. **B70** (1974) 93–115.

[39] Xavier Artru, Phys. Rept. **97** (1983) 147.

[40] R. Odorico, Nucl. Phys. **B172** (1980) 157.

[41] Geoffrey C. Fox and Stephen Wolfram, Nucl. Phys. **B168** (1980) 285.

[42] Richard D. Field and Stephen Wolfram, Nucl. Phys. **B213** (1983) 65.

[43] Thomas D. Gottschalk, Nucl. Phys. **B214** (1983) 201.

[44] T. Sjöstrand, Comput. Phys. Commun. **82** (1994) 74–90.

[45] C. Peterson and D. Schlatter and I. Schmitt and Peter Zerwas, Phys. Rev. **D27** (1983) 105.

[46] The LEP experiments, Combining Heavy Flavour Electroweak Measurements at LEP, CERN-PPE/96-017 (1996).

[47] W. Braunschweig and others, Z. Phys. **C45** (1989) 193.

[48] D. Coffman and others, Phys. Lett. **B263** (1991) 135–140.

[49] P. Abreu and others, Phys. Lett. **B425** (1998) 399.

[50] M. Acciarri and others, Phys. Lett. **B416** (1998) 220.

[51] R. Akers and others, Z. Phys. **C61** (1994) 209–222.

[52] The LEP Heavy Flavour Working Group, Input Parameters for the LEP/SLD Electroweak Heavy Flavour Results for Summer 1998 Conferences, LEPHF/98-01 (1998).

[53] W. Hollik, Predictions for e^+e^- process, in P. Langacker, editor. Precision tests of the standard electroweak model, World Scientific (1995).

[54] W. J. Marciano and A. Sirlin, Phys. Rev. Lett. **61** (1988) 1815.

[55] D. Bardin and others, Nucl. Phys. **B351** (1991) 1–48.

[56] D. Yu. Bardin and M. S. Bilenkii and G. Mitselmakher and T. Riemann and M. Sachwitz, Z. Phys. **C44** (1989) 493, (see also http://www.ifh.de/theory/publist.html#software).

[57] The LEP Collabotations, the LEP Electroweak Working Group and the SLD Heavy Flavour Group, A Combination of Preliminary Electroweak Measurements and Constraints on the Standard Model, CERN-PPE/96-183 (1996).

[58] S. Jadach, Z. Was et al., in Z Physics at LEP1, CERN report CERN 89-08, eds. G. Altarelli, R. Kleiss and C. Verzegnassi (CERN, Geneva, 1989) Vol. 1, p. 235 and references therein..

[59] Z Physics at LEP I, edited by G. Altarelli, R. Kleiss, C. Verzegnassi, CERN 89-08 (1989).

[60] A. A. Akhundov and D. Yu. Bardin and T. Riemann, Nucl. Phys. **B276** (1986) 1.

[61] Wim Beenakker and Wolfgang Hollik, THE WIDTH OF THE Z BOSON, 1988.

[62] J. Fleischer and O. V. Tarasov and F. Jegerlehner and P. Raczka, Phys. Lett. **B293** (1992) 437–444.

[63] M. Acciarri and others, Z. Phys. **C62** (1994) 551–576.

[64] The LEP Collaborations, ALEPH, DELPHI, L3, OPAL, the LEP Electroweak Working Group and the SLD Heavy Flavour Group and Electroweak Groups, A Combination of Preliminary Electroweak Measurements and Constraints on the Standard Model, L3 preprint 170, to be submitted to the CERN Preprint Service, CERN-EP/99-XXX.

[65] LEP Design Report
Part I: The LEP injector chain, LEP/TH 29 Vol. I, CERN, 1983,
Part II: The LEP main ring, LEP/TH 02 vol. II, CERN, 1984.

[66] Nucl. Instrum. Meth. **A289** (1990) 35.

[67] O. Adriani and others, Phys. Rept. **236** (1993) 1–146.

[68] M. Acciarri and others, Nucl. Instrum. Meth. **A351** (1994) 300–312.

[69] A. Adam and others, Nucl. Instrum. Meth. **A344** (1994) 521–528.

[70] A. Adam and others, Nucl. Instrum. Meth. **A348** (1994) 436.

[71] Andreas S. Schwarz, Phys. Rept. **238** (1994) 1–133.

[72] S. Petrak, SMD Efficiency in 1994, Internal Report, L3 Note 1998, CERN, 1996.

[73] F. Beissel and others, Nucl. Instrum. Meth. **A332** (1993) 33.

[74] D. Bourilkov, TEC Calibration with the SMD, Internal Report, L3 Note 1870, CERN, 1995.

[75] D. Bourilkov D. Wagenaar, TEC single wire resolution, Internal Report, L3 Note 1871, CERN, 1995.

[76] K. Deiters and others, Nucl. Instrum. Meth. **A323** (1992) 162.

[77] E. Lieb and R. Völkert, Performance of the Z-Chamber during LEP Data Taking from 1992 to 1995, L3 Note 2028 (1996).

[78] I. C. Brock and others, Nucl. Instrum. Meth. **A381** (1996) 236–266.

[79] R. Bizzarri and others, Nucl. Instrum. Meth. **A317** (1992) 463.

[80] U. Uwer, Aufbau und Eichung der Szintillationszähler des L3-Experiments, Diploma thesis, RWTH-Aachen, 1990.

[81] U. Uwer, The L3 Scintillation Counter System, Internal Report, L3 Note 1400, CERN, 1993.

[82] T. Sjöstrand, PYTHIA 5.7 and JETSET 7.4 Physics and Manual, Preprint CERN-TH 7112/93, CERN, 1993; revised August 1995.

[83] G. Marchesini and B. R. Webber, Nucl. Phys. **B310** (1988) 461.

[84] G. Marchesini and others, Comput. Phys. Commun. **67** (1992) 465.

[85] The L3 detector simulation is based on GEANT Version 3.14; see R. Brun *et al*, GEANT 3, CERN DD/EE/84-1 (Revised), September 1987 and the GHEISHA program (H. Fesefeld, RWTH Aachen Report PITHA85/02, 1985) for the simulation of hadronic interactions.

[86] D. Kamrad, FUL3 - A System for Distributed and Asynchronous Parallel Processing of Monte Carlo Events in a Heterogeneous Computing Environment, L3 Note 2358 (1999).

[87] W. Bartel and others, Z. Phys. **C33** (1986) 23.

[88] B. Adeva and others, Z. Phys. **C51** (1991) 179–204.

[89] M. Acciarri and others, Z. Phys. **C62** (1994) 551–576.

[90] D. Brown and M. Frank, Tagging b hadrons using track impact parameters, ALEPH 92-135 PHYSIC 92-124, CERN, 1992.

[91] C. Peterson and D. Schlatter and I. Schmitt and Peter Zerwas, Phys. Rev. **D27** (1983) 105.

[92] LEPEWWG and SLD HF Group, A Combination of Preliminary LEP and SLD Electroweak Measurements and Constraints on the Standard Model, Internal Note, LEPEWWG/96-01 (1996).

[93] The LEP Coll. and the SLD Heavy Flavour and Electroweak Groups, A Combination of Preliminary Electroweak Measurements and Contraints on the Standard Model, LEPEWWG/98-01 (1998).

[94] R. Marshall, Z. Phys. **C43** (1989) 607.

[95] F. James and M. Roos, Comput. Phys. Commun. **10** (1975) 343.

[96] M. Grünewald, Combined Analysis of Precision Electroweak Results, HUB-EP-98/67
D. Karlen, Proceedings of ICHEP98, Vancouver, 1998.

[97] S. Blyth, Measurement of $A_{FB}^{0,b}$, Internal Report, L3 Note 2324, CERN, 1998.

[98] John Ellis and Jorge L. Lopez and D. V. Nanopoulos, Phys. Lett. **B397** (1997) 88–93.

[99] Jens Erler and Jonathan L. Feng and Nir Polonsky, Phys. Rev. Lett. **78** (1997) 3063–3066.

Acknowledgements

Dirk Kamrad   Hans-Fallada-Straße 12
                                               12683 Berlin

Tabellarischer Lebenslauf

07. Januar 1966   geboren in Torgelow
                       Familienstand: verheiratet

1972 – 1982   10-klassige Oberschule in Berlin,
                       Prädikat: "Auszeichnung"

1982 – 1985   Berufsausbildung zum Elektromechaniker mit Abitur,
                       Prädikat: "Auszeichnung"

1985 – 1988   Ableistung des Wehrdienstes als Soldat auf Zeit

Okt.88 – Mai 95   Physikstudium an der Humboldt-Universität zu Berlin mit
                       dem Nebenfach Informatik, abgeschlossen mit der Diplomar-
                       beit "Untersuchungen zur Ortsmeßgenauigkeit des Silizium
                       Mikrovertex Detektors von L3" am DESY-IfH Zeuthen
                       Gesamturteil: "Gut"
                       Urteil über das Diplomverfahren: "Sehr Gut"

Juli 95 – Juni 98   Wissenschaftlicher Mitarbeiter am Deutschen Elektronen-
                       Synchrotron DESY Zeuthen

Mai 99   Abschluß der Doktorarbeit zum Thema: "Measurement of the
                       Partial Z Decay Width into b Quarks with the L3 Detector at
                       LEP"

Selbständigkeitserklärung

Hiermit versichere ich, die vorliegende Arbeit selbständig angefertigt und keine weiteren als die angegebenen Hilfsmittel verwendet zu haben.

Dirk Kamrad